RI | 9578

REPORT OF INVESTIGATIONS/1995

Studies of Stope-Scale Seismicity in a Hard-Rock Mine

Part 2: Characterization of Blast and Rock Burst Aftershock Sequences

UNITED STATES DEPARTMENT OF THE INTERIOR

UNITED STATES BUREAU OF MINES

U.S. Department of the Interior
Mission Statement

As the Nation's principal conservation agency, the Department of the Interior has responsibility for most of our nationally–owned public lands and natural resources. This includes fostering sound use of our land and water resources; protecting our fish, wildlife, and biological diversity; preserving the environmental and cultural values of our national parks and historical places; and providing for the enjoyment of life through outdoor recreation. The Department assesses our energy and mineral resources and works to ensure that their development is in the best interests of all our people by encouraging stewardship and citizen participation in their care. The Department also has a major responsibility for American Indian reservation communities and for people who live in island territories under U.S. administration.

Report of Investigations 9578

Studies of Stope-Scale Seismicity in a Hard-Rock Mine

Part 2: Characterization of Blast and Rock Burst Aftershock Sequences

By Robert L. Kranz, John P. Coughlin, and Selena Billington

UNITED STATES DEPARTMENT OF THE INTERIOR
Bruce Babbitt, Secretary

BUREAU OF MINES
Rhea Lydia Graham, Director

International Standard Serial Number
ISSN 1066-5552

CONTENTS

ILLUSTRATIONS

Page

TABLES

UNIT OF MEASURE ABBREVIATIONS USED IN THIS REPORT

deg	degree	m	meter
h	hour	s	second

Reference to specific products does not imply endorsement by the U.S. Bureau of Mines.

STUDIES OF STOPE-SCALE SEISMICITY IN A HARD-ROCK MINE

PART 2: CHARACTERIZATION OF BLAST AND ROCK BURST AFTERSHOCK SEQUENCES

By Robert L. Kranz,[1] John P. Coughlin,[2] and Selena Billington[1]

ABSTRACT

Mining-induced microseismicity data collected by the U.S. Bureau of Mines in a hard-rock mine were analyzed for spatial and temporal patterns that might prove useful for prediction of rock bursts or assessment of rock mass damage changes. Pattern attributes described and illustrated in the previous report (part 1) were applied to the study of aftershock sequences associated with two different stopes. The aftershock sequences were spatially and temporally fractal, and the fractality was maintained for up to 16 h following a sequence progenitor. This suggests mechanical interdependency among the aftershocks. No statistical difference was found in the distributions of fractal dimensions when comparing two different stopes or when comparing aftershock sequences initiated by blasts or bumps. This suggests a lack of sensitivity to both stress perturbation mechanism and local damage states. However, differences between the two stopes were found in other sequence attributes that support inferred differences in the magnitude of stress concentrations and damage near each stope, and over time as a stope is developed.

[1]Geophysicist.
[2]Electronics engineer.
Denver Research Center, U.S. Bureau of Mines, Denver, CO.

INTRODUCTION

This is the second report on studies of stope-scale seismicity that the U.S. Bureau of Mines (USBM) has conducted using data gathered at a hard-rock mine in northern Idaho as part of its mine safety program. The first part described several new methods employed and factors affecting their results (*1*).[3] It was shown that the spatial and temporal patterns of groups of microseismic events had a fractal, or self-similar, and scale-invariant character over a limited scale range. Further, it was shown that the manner of selecting the ensemble of events to be analyzed could definitely affect the results of the analyses, especially in regard to identifying real changes in event group attributes. Finally, it was suggested that the geometrical arrangement of groups of microseismic event locations might be relatable to certain physical structures such as ore veins or faults in the stope region. This second report describes and discusses characteristics of a particularly prominent group of microseismic events: the aftershocks that immediately follow the larger events and production or destress blasts.

Microseismicity in a mine can result from a variety of mechanically different sources: the fracture of previously unbroken rock, slippage on preexisting faults or fractures, pillar collapse, rock and gas outbursts, roof falls, etc. The superposition of gravity and mine-wide tectonic stresses may favor certain mechanisms. Production or destress blasting can activate any of these mechanisms. One goal of the research reported here is to obtain information about the mechanics of deformation and rock mass structural changes near active stopes from analysis of the microseismicity generated as a direct or indirect result of mining. We believe such information may prove to be as vital as knowledge of the state of stress for any deterministic method proposed for predicting damaging rock bursts in a mine. Furthermore, in the absence of detailed geologic structural mapping as mining proceeds, interpretation of the spatial aspects of the induced microseismicity may be the only evidence available for determining inaccessible rock mass damage. In that sense, throughout this report the phrase *"rock mass damage"* refers to either newly created fractures or actively slipping, preexisting fractures.

In this report, the word *"progenitor"* refers either to a manmade blast or to any bump or rock burst that is isolated in space and time from other progenitors and that produces, or is associated with, subsequent microseismicity. The words *"bump"* and *"rock burst"* are used here synonymously to refer to the larger sized seismic events in the mine, although the latter term usually connotes a potentially hazardous state of damage, in that rock is ejected into the mine openings. The word *"aftershock"* is meant to apply to any microseismic event that follows, and is presumably related to, a nearby progenitor. In this report we do not focus on individual aftershock events in the set collected following a progenitor. Instead, we study the entire set or *aftershock sequence* as an *individual entity*, although it may be contaminated or incomplete. Each aftershock sequence will have its own characteristics or attributes.

The problems of defining precisely what events should be classified as aftershocks of large progenitors, and the time and space windows within which one should search for these, have occupied seismologists for some time (*2-8*). Unfortunately, many of the methods in these references require knowledge of background seismicity characteristics. In a working mine, "background seismicity" is an ever-changing concept. Rather than apply some scheme for separating aftershocks from concurrent background seismicity, in this report we simply restrict the term to events that are "well located" (as defined in part 1(*1*)) within the individual stope geophone network and that occur within 16 h following a blast or bump. This space-time window probably overestimates the number of larger microseismic events (which tend to be well located) and underestimates the number of smaller events (which tend not to be well located) that are truly aftershocks of the progenitors. The estimate of numbers and the measures of many characteristics of the collection of aftershocks probably degrade with increasing time following the progenitor. By consistently using the same space-time windows, however, this method imposes no prior assumptions about statistical distributions or independence of the microseismic events in any particular sequence following a progenitor. This approach implicitly assumes that any contamination of the aftershock patterns is either relatively small or easily identifiable.

Large progenitors may affect the seismicity at stopes other than the primary stope (*9*). Although all mining microseismicity may ultimately be interrelated through stress readjustments at different scales, temporally or spatially "near" event sources are more likely related than more separated event sources. Potential aftershocks located at stopes other than those nearest the progenitor are, therefore, not considered. Interstope-related seismicity will be the subject of a subsequent report.

Attributes of selected aftershock sequences are defined and measured according to the methods put forth in part 1 (*1*). Although there are many possible attributes of individual aftershock sequences, some attributes may be more characteristic of a stope or progenitor type than

[3]Italic numbers in parentheses refer to items in the list of references preceding the appendixes.

others. In addition to the goal of gathering information about rock mass damage, another goal has been to evaluate the usefulness of such sequence attribute information for understanding bump or rock burst mechanics. For example, one might ask whether rock bursts or bumps seemingly unprovoked by blasting, and originating within the rock mass, cause subsequent stope responses that are different from those immediately following nearby production blasts. One might hypothesize that sequences following a production blast can best be distinguished from sequences following a damaging rock burst by comparison of the spatial extent of the aftershock event locations, or perhaps by the cumulative energy released during the sequence, or by some other attribute. By measuring and analyzing many aftershock sequences, one may be able to group the sequences by their more important attributes and test such hypotheses. From this higher level of association, information may be obtained about different stope relaxation responses, differences between blasts and bumps, effectiveness of destress blasting, etc.

The stope-scale microseismicity data sets that were analyzed are first described below. Then a brief recapitulation of the different measures of microseismic event sequence attributes, previously described and discussed in part 1 (*1*), is presented. Results of the analyses for specific sequence attributes are then presented. In particular, the changing nature of certain sequence attributes and the unchanging nature of others are demonstrated. Subsequently, the various attribute measures are used to study differences, similarities, and associations among the aftershock sequences. To do that, common statistical measures and classification analysis are employed. Finally, results are presented and discussed in terms of the temporal evolution and characteristic behaviors of a stope.

An outline of the general methods used to classify objects based on measured attributes is presented in appendix A. In appendix B, an example of grouping individual seismic events in a sequence by their attributes is presented. The same methods are applied to entire aftershock sequences in the body of this report.

DESCRIPTION OF MICROSEISMICITY DATA SETS

All data discussed in this report were collected in the Galena Mine by the USBM in cooperation with ASARCO, Inc., the mine operator. The mine and two of its stopes (49-189 and 49-307, hereafter called stopes 189 and 307, respectively) were previously described by the authors in part 1 (*1*) and by other USBM work referenced in that report. Maps of stopes 189 and 307, showing the local networked geophone locations, were also included in part 1 (*1*). A third stope studied (stope 46-99, hereafter called stope 99) was similarly described by Boler and Swanson (*10*), and a map of that stope's area and local geophone placements is presented in figure 6 of their report. Characteristics of the typical network with 16 geophones were also previously described (*1*).

The stopes are mined using the overhand cut-and-fill method. This results in ever-diminishing, horizontal pillars punctured by vertical raises. The temporal and spatial stope development upward is illustrated schematically in figures 1 and 2 for stopes 189 and 99, respectively. These figures will be important for discussions in conjunction with the data analyses later in this report. Activity logs and network parameters for each working stope were recorded by mine personnel. Geophone network characteristics at each stope were essentially constant during the 1989 and 1990 time periods in which the blasts and bumps occurred. However, following the first quarter of 1991, the renewed northeastern development of stope 99 (figure 2*B*) was monitored with a slightly altered network that provided wider, but perhaps less sensitive, coverage. The effect of this alteration can be seen in some of the measured aftershock sequence attributes, as described below. For that stope and period, it is difficult to separate certain network-related attribute changes from those changes resulting from the move over to a physically different portion of the stope. Accordingly, analyses of stope 99 sequences that occurred after the network alteration in 1991 are presented but not used in the classification work.

We selected 40 aftershock sequences occurring in stope 189 and 37 aftershock sequences occurring in stope 99 during the period 1989 to 1991. During these periods, event detection threshold levels were relatively stable. The number of analyzed aftershock sequences in stope 307 were too few to provide meaningful statistical comparisons; therefore, stope 307 will not be discussed in this report. Table 1 lists the sequences analyzed in stopes 189 and 99, along with a "type" assignment that indicates whether the sequence followed a blast (BL), a blast with one or more bumps within a few minutes of the blast (BB or BBB), or an isolated bump (BU).[4] Also reported in table 1 is the accumulated number of "well-located" events. The number of events that triggered five or more network geophones within the 16 h following the sequence progenitor may be considerably larger. Only well-located events were used in the spatial attribute analyses. Temporal attribute analyses

[4]The symbol designations used in many of the figures of this report to distinguish these three types of aftershock sequences are as follows: ellipses represent BL aftershock sequences, rectangles represent BB or BBB aftershock sequences, and triangles represent BU aftershock sequences.

Table 1.—Selected aftershock sequences

Progenitor type[1]	Initialization time[2]	Number of well-located events[3]
	STOPE 189	
BB	890313.142401	1,098
BB	890316.142321	548
BL	890321.222035	337
BL	890322.221945	782
BU	890325.022201	696
BL	890331.221931	517
BL	890403.142329	635
BL	890406.142131	597
BL	890629.142009	425
BL	890714.221831	627
BU	890715.053501	453
BL	890720.141759	761
BU	890804.030122	1,024
BU	890805.034458	1,187
BL	890907.222006	307
BBB	890912.221953	1,435
BL	890919.141927	269
BB	890921.141959	255
BL	891004.221936	227
BL	891005.221959	335
BL	891009.221902	178
BL	891010.221933	316
BL	891011.221951	210
BU	891120.075026	277
BB	891205.222055	318
BL	891211.141941	372
BB	891215.141947	522
BBB	891219.141948	566
BB	900102.221912	875
BB	900104.222045	644
BB	900110.141844	1,229
BB	900112.142659	171
BB	900116.142003	642
BBB	900117.143121	1,032
BL	900118.142011	790
BL	900119.142921	979
BBB	900123.221653	555
BB	900124.221809	409
BB	900306.141655	624
BBB	900307.141821	1,353
	STOPE 99	
BB	891011.221711	370
BBB	891018.141812	284
BB	891020.141954	370
BBB	891119.142112	289
BBB	891227.142641	485
BB	891228.221845	1,181
BU	891229.094121	712
BB	900104.142048	358
BB	900105.141944	548
BBB	900109.141918	276
BBB	900110.141945	247
BBB	900202.144911	588
BU	900207.122021	507
BB	900219.144602	495
BL	900406.141949	336
BB	900504.141852	456

See footnotes at end of table.

Table 1.—Selected aftershock sequences—Continued

Progenitor type[1]	Initialization time[2]	Number of well-located events[3]
	STOPE 99—Continued	
BB	900504.141852	456
BL	900511.141943	474
BB	900615.145016	1,128
BL	900830.221624	381
BL	900907.141754	231
BB	900913.141712	597
BBB	901009.141806	285
BBB	901011.141806	435
BB	901019.222021	478
BU	901118.131106	231
BL	901220.143448	213
BB	910103.141924	267
BBB	910108.141854	336
BB	910111.141905	233
BL	910117.141921	306
BB	910205.142999	457
BBB	911003.221636	202
BB	911025.141912	174
BU	911029.052748	303
BBB	911030.221701	212
BB	911108.221801	166
BBB	911223.221712	231
BU	930318.150027	350

[1]Progenitor type. BL = production or destress blast not quickly followed by a rock burst or a bump; BB = blast followed by a single rock burst or bump; BBB = production blast followed by two or more bumps; BU = relatively large rock burst or bump not preceded (within 8 h) by any blasting or significant work in the stope.

[2]Initialization time of sequence: year, month, day, hour, minute, second. This is typically within a few seconds of progenitor occurrence time.

[3]Cumulative number of well-located events in the stope area 16 h after progenitor occurrence.

used the trigger occurrence times for events that were located, with various degrees of accuracy, in the network region. One other aftershock sequence that occurred near stope 99 in March 1993 is also listed. This sequence will be discussed separately from the others since it occurred long after all production operations at the Galena Mine were halted in June 1992.

Aftershock sequence selection was partly subjective. Selection was based primarily on the availability of adequate numbers of well-located aftershock events and lack of any obvious contemporaneous sources of contamination by other mining activity for 16 h after sequence initiation. Also eliminated from consideration were those sequences following a blast that included several small bump occurrences spaced out over several hours. Although there were potentially many more sequences that might have been studied had we relaxed our selection restrictions, we believe that we have selected relatively uncontaminated,

representative samples of the postblast or postbump microseismic activity of each stope.

Progenitors for some of the aftershock sequences caused considerable damage to the stope. For example, damage from a magnitude 2.7 event and its aftershock sequence (the last entry, labeled 900307.141821, for stope 189 in table 1) was severe enough to essentially end further production work in the 189 stope area. We did not specifically select or eliminate sequences on the basis of reported damage or lack thereof. However, the most damaging progenitors during the study period are included in the sequences analyzed.

AFTERSHOCK SEQUENCE ATTRIBUTES

As indicated in part 1 (*1*), the primary raw data consisted of two pieces of information: first-phase arrival times at up to 16 geophone stations per stope and the relative amplitude of the signal within a small time window that starts with that phase at selected geophone stations. From those data, event origination time, event source location, and a normalized measure of event size were derived. Secondary statistical information about groups of events was subsequently derived. These spatial, temporal, and size event group attributes are listed in table 2, along with the typical amount of uncertainty. Most of these attributes were discussed and the method of determination was described in part 1 (*1*). The determination of the others is fairly straightforward. However, a brief restatement of the attributes is in order here.

Table 2.—Aftershock sequence attributes[1]

Type	Label	Average uncertainty
Spatial:		
Correlation fractal dimension	SF	0.1
Average interevent location distance, m	AD	5
Interevent distribution skewness ratio, %	SR	20
Strike and dip of major seismic plane, deg	S, D	5
Temporal:		
Correlation fractal dimension	TF	0.05
Event rate decay power law exponent	DR	0.1
Coefficient of variation of interevent times	CV	[2]
Size:		
Number of triggers	N	[2]
Total normalized energy, %	ET	25
Average normalized energy, %	EA	25
B-value	BV	0.2
Others related to sequence progenitor:		
Total length of blasted holes, m	LT	[2]
Progenitor magnitude	M	0.2

[1]All attributes except S, D, LT, and M were separately determined for periods of 2, 4, 8, and 16 h following the progenitor. S and D were determined 16 h after sequence initiation. Some sequences do not have values for all attributes in each period.

[2]Untabulated values indicate either an exact measurement or no estimate possible.

For each aftershock sequence, quantified *spatial* attributes included the correlation fractal dimension (SF), the average of the sequence interevent location distances (AD), the skewness of the interevent distance distribution normalized to an averaged random distribution in the same volume (skewness ratio SR), and the strike and dip (S and D) of the major plane found in the event locations pattern using planarity-finding algorithms (*11-12*). The spatial fractal dimension SF is inversely related to the degree of clustering of the event locations. Event locations randomly placed in the same rock mass volume as the real event locations have SF values close to 3. Virtually all aftershock sequence event locations were spatially fractal (with SF values less than 3) over some scale range. The spatial fractal dimensions reported here are for the range 4 to 32 m. Spatial fractality extended to a greater upper limit in some sequences studied.

The distribution of aftershock interevent distances is highly skewed, as would be expected for clustered aftershock patterns. However, even events placed randomly within the asymmetrical geophone network region may show a skewed interevent distance distribution. The skewness ratio SR will be equal to 1 if the interevent distance distribution results from essentially random locations in the same volume occupied by the real data. The SR value will be greater than 1 if the interevent distances are more skewed than for random locations; larger SR values indicate more clustered aftershock locations.

Quantified *temporal* attributes included the correlation fractal dimension (TF), the negative exponent of a power law fit to the event rate as a function of time following the progenitor (DR), and the coefficient of variation (CV) of interevent trigger times calculated as the ratio of the standard deviation to the mean of those interevent times. The temporal fractal dimension TF is inversely related to the clustering of event occurrence times. Random occurrences, which can have some clustering, typically give TF values of 1. During any truncated period following the progenitor, virtually all aftershock occurrences were fractally distributed over a range of several seconds to about one-third of the period examined. With one exception, the

longest period examined for a single aftershock sequence was 16 h. CV and DR values are measures of the times to next event occurrence and changes in the rate of recurrence, respectively. The coefficient of variation CV is similar to the Poisson index of dispersion and measures the departure from random occurrences that would give a CV value of 1.

Size attributes for the aftershock sequences included the number of threshold-exceeding triggers (N), a cumulative energy count attribute (ET) related to the cumulative seismically released energy normalized to account for geometrical spreading (as described in part 1 (*1*)), the average energy count per event in the sequence (EA = ET/N), and the slope (BV) of the log number, log- normalized energy distribution. This B-value (BV) is related, but not equal, to the customary seismological b-value that relates event magnitude to numbers of events. We used the B-value because our aftershock events were too small to obtain a magnitude for each of them. Using a calibrated surface seismograph, local magnitude (M_L) was determined for the progenitor events. Assuming that the aftershock energies scale in the same manner as the sequence progenitor energies, the B-value reported here should be divided by 1.3 to obtain the more commonly reported b-value.

Potentially significant size attributes of the sequence progenitors were also examined for many sequences. These included the total length (LT) of blasted holes (for blast-induced sequences) and the progenitor magnitude (M), derived from the waveform coda length on the surface seismograph.

Aftershock sequence attributes were separately measured for four cumulative periods after the sequence progenitor occurrence (i.e., for 2, 4, 8, and 16 h following the progenitor). Each longer period of observation contains the data in the preceding periods. This was done since we did not know a priori when an aftershock sequence might disappear into the background seismicity or when the sequence might be contaminated by outside events. We thereby effectively quadrupled the number of aftershock sequences available to us, although not all attributes could be reliably measured to the end of each time period. This also enabled us to examine the dependency (if any) of the attribute values on the period of observation. In the next sections it is shown that, within the estimated uncertainties associated with the attribute measurements, most of the 2-h attribute values were not statistically different from the corresponding 16-h values. That is, these attributes were essentially constant after 2 h and independent of the window of observation used during the aftershock period. However, several attributes (e.g., DR, N, ET) were clearly not stationary, requiring comparisons of values determined during similar periods only. Attribute changes or rate of change at a specific stope could have been compiled as separate attributes, but this was not done in any regular fashion. It is important to realize that *every aftershock sequence is essentially a multidimensional vector in attribute space, and some, but not all, of the vector components are time dependent.*

ATTRIBUTE ANALYSES

SPATIAL ATTRIBUTES

Aftershock locations are highly clustered near the stope boundaries, but extend to areas outside the immediate stope as well. Figure 3 shows some typical patterns. The degree of location clustering is quantified by the SF attribute. The average spacing between locations and the deviation from a random distribution of interevent distances are quantified by the AD and SR attributes, respectively.

Values for the spatial fractal dimension (SF) measured 2 and 16 h after progenitor occurrence are shown in figures 4*A* and 4*B* for all sequences studied in stopes 189 and 99, respectively. The diagonal line across the graph is the locus of points that indicates equality of attribute values measured for the two cumulative periods. In these figures, points plotted above or below the line indicate that the value measured 2 h after progenitor occurrence was larger or smaller, respectively, than the value measured 16 h after progenitor occurrence. In virtually all cases, values measured for the 4- and 8-h observation periods are bounded by those measured at 2 and 16 h.

To evaluate whether the spatial fractality is different at the 2-h mark than at the 16-h mark, one must consider the uncertainty in each point plotted. Each point is the slope of a fitted line with a quantified uncertainty. Both the mean and standard deviation of these fit uncertainties are about 0.1 for the SF attribute. About half of the points in figures 4*A* and 4*B* fall within a ±0.1 region around the equality locus, indicating no statistical difference in the values measured for the two periods of observation. Almost all points are within 0.2 of the equality locus. Recall that the smaller the SF value, the more clustered is the event location point pattern. Those sequences with 16-h SF values more than 0.1 greater than the 2-h values are somewhat less clustered. In only a few cases is the location point pattern marginally more clustered for 16 h of data than for only 2 h of data. We believe that, in those few cases, the additional clustering is a result of secondary

aftershock sequences or effects of subsequent mining activity not related to the sequence progenitor. In general, the degree of aftershock location clustering after 2 h is the same or marginally greater than the degree of clustering at subsequent times. Observations of aftershock locations sequentially plotted on a video screen confirm that after 2 h, events continue to occur in generally the same volume and same pattern as those that occurred in the first 2 h.

The average distance between well-located events (AD) is shown in figures 5*A* and 5*B* for stopes 189 and 99, respectively. The average interevent distance is almost always a little greater when calculated with 16 h worth of locations than with only 2 h worth. With a few notable exceptions, the increase in average interevent distance is typically 6 m or less. Although the location uncertainty is about 5 m for these events, the individual location errors are just as likely to move events closer as farther apart. Therefore, any increase of average interevent distances greater than 5 m is probably real. The sequences in stope 99 that show large differences between the 2- and 16-h windows are all sequences that occurred after network alteration in April 1991. The alteration resulted in a tendency to locate more events outside of the immediate stope area, and the chances of doing so apparently increase as time progresses. For those cases, it is impossible to separate real differences from the network effects.

Values for the skewness ratio attribute (SR) are presented in figures 6*A* and 6*B* for stopes 189 and 99, respectively. In both stopes, some sequences are extremely skewed. This is another indication of clustering, with a preponderance of small interevent distances. Many interevent distance distributions appear to be more skewed after 16 h than only 2 h after progenitor occurrence. It is hard to assess the accuracy of any particular SR value. The calculation itself is exact, but different normalizing random data sets and different numbers of interevent distances used can both affect the calculated value. We created random event locations with the same number and within the same volume as the real data sets. Based on comparing the skewness of 50 different random data sets for 1 particular sequence, an estimate of the SR error is 20%. Thus, most of the apparent differences in 2- and 16-h values are unlikely to be significant.

Only a few sequences in either stope were tested for location migration (as described in part 1 (1)) during the 16 h period following the progenitor. Given the estimated error in event locations (5 m), no apparent migration of event location clusters was found during those aftershock sequences. Together with the above results, this implies that the nature of aftershock location patterns is well established within 2 h after progenitor occurrence and, except for increasing the number of event locations, changes little thereafter. However, there may be differences between blast, blast-bump, and bump sequences or between stopes. These are assessed in a later section of this report.

TEMPORAL ATTRIBUTES

Two examples of the temporal decay in event occurrence rate are shown in figure 7. The lower curve shows a relatively smooth, uninterrupted decay for 7 h. The upper curve is an example of what was more usually observed. A sudden rise in event rate followed by a relatively rapid decay is seen after some hours. Such a rise may result from a significant large aftershock creating its own secondary aftershock sequence, from renewed mining activity in the stope, or from a large blast at another nearby stope. When the rate jump occurs later in the aftershock sequence, DR and CV attribute values determined for the preceding time periods are more accurate measures. Rate jumps do not appear to have much effect on the temporal fractal dimension TF, probably because they contribute interoccurrence times that are distributed in the same way as the earlier part of the overall aftershock sequence. Most of the DR and CV values determined for the 16-h window were contaminated by rate jumps and are not presented below. Instead, the 8-h data are presented for these attributes.

The temporal fractal dimension (TF) is presented in figures 8*A* and 8*B* for stopes 189 and 99, respectively. Just as for the SF attribute, each point represents the slope of a fitted line. The typical uncertainty in each of these values is about 0.05. Accordingly, only a few sequence interoccurrence time patterns are statistically indistinguishable from random interoccurrence times, which would result in a TF value of 1. The great majority are clearly nonrandom. The degree or strength of the temporal clustering is not strong in most cases, however. With few exceptions, differences between TF values measured for the 2- and 16-h windows are not statistically significant. The temporal fractality, like the spatial fractality, is established within the first 2 h and generally persists at least up to 8 h after progenitor occurrence.

The exponent in the simple power law fit to the event rate as a function of time (DR) is presented in figures 9*A* and 9*B* for stopes 189 and 99, respectively. Points plotted below the diagonal equality line indicate faster event rate decay for the 2-h period than for the 8-h period. Since the uncertainty in the fitted exponent value is typically about 0.1, some of the DR values are statistically the same when evaluated for either period. However, a substantial number are clearly different. The few points more than 0.1 above the equality line suggest some early contamination in those sequences. In figure 9*B*, the five sequences having very rapid rate decays (greater negative exponents) all occurred after network alteration in 1991, so may be discounted. Slower event rate decay, when viewed in the 8-h window compared with the 2-h window (the majority of cases here), suggests inadequacy of the simple power law with constant parameters to describe the rate

decay over the entire period of observation. Alternatively, many sequences may have effectively ended in less than 8 h, and the local background rate may have been inadvertently combined with the aftershock rate, giving a spurious low value for DR. If the second explanation is valid, comparisons between sequence attributes should be limited to only those measured at shorter observation periods.

Most earthquake aftershock studies have used a modified version of the simple power law: the so-called modified Omori law (*2, 13-14*). The relative effect of the modification is to make the absolute value of the exponent larger (more negative), compared with the simple power law. Unless our data are refit to the modified Omori relation, our rate decay exponents cannot strictly be compared with values in other aftershock studies that used the modified relation. However, during a working visit to the USBM, T. Satoh[5] fitted the modified Omori relation to many aftershock sequences originating near stope 99. The period of observation in his study varied, but was usually for 10 h or less after progenitor occurrence. The exponent values he obtained were about 0.2 to 0.3 more negative than ours for the same sequences, but overall were similarly distributed. His results indicated a weak dependence of the exponent on period of observation after 8 h. We conclude that, for comparative purposes, the unmodified power law exponent is probably a valid attribute for these sequences for up to 8 h following progenitor occurrence.

The coefficient of temporal variation (CV) is presented in figures 10*A* and 10*B* for stopes 189 and 99, respectively. All values for any period of time are greater than unity, indicating some clustering in the distribution of interevent occurrence times. The larger the value, the greater the clustering. The sequences occurring after network alteration around stope 99 had high CV values significantly discordant with the other sequences. It is difficult to evaluate the uncertainty in individual CV attribute values. Like the SR attribute, the calculation is exact. Small errors in trigger times could potentially bias the mean or standard deviation of interoccurrence times. However, such errors and their effects on CV values are expected to be relatively small. More important is the fact that, as time progresses after progenitor occurrence, an increasing number of unrelated, random background event triggers are added to the population analyzed. The number and rate of such random event triggers may vary from stope to stope and from day to day at any particular stope. The background rate before each sequence was not measured. Since the overall trigger rate for aftershocks is decreasing after progenitor occurrence, one should expect aftershocks to occur further apart in time, on average. Accordingly, CV values should decrease, moving toward unity more quickly, and points should plot above the equality line in figures 10*A* and 10*B*. Points plotting far below the equality line may indicate the effects of high or changing background rates.

[5]Letter report by T. Satoh, Geological Survey of Japan, 1991.

SIZE ATTRIBUTES

Both the numbers of events and the cumulative event energies continue to increase, at a decreasing rate, for some time following the progenitor. The energy count (ET), corrected only for geometric spreading and integrated over all events up to 2 h and up to 16 h after the progenitor, is presented in figures 11*A* and 11*B* for stopes 189 and 99, respectively. This cumulative energy count is presented on an arbitrary, but consistent, scale for both stopes. Note that all sequence points lie below the equality line, indicating an increase in accumulated energy release over time. The increase between the 2- and 16-h data is less variable for stope 189 than for stope 99. Although values for the ET attribute span about one order of magnitude in both stopes, the mean ET values are different for the two stopes. Both east and west sides of stope 189 were often blasted at the same time, whereas only one area was blasted in stope 99. However, we found no correlation between ET and whether or not blasting occurred on either side of the raise in stope 189. Additionally, in both stopes, ET was found to be essentially independent of the total length of blasted holes. Some other explanation is needed since differences in ET between the bump sequences of the two stopes also exist.

It is difficult to distinguish the relative effects of different stope network sensitivities from real physical differences in the stope regions and evaluate them to account for these observations. There was not a large difference in the overall numbers of events detected or well located at the two stopes, so trigger threshold differences should not be an issue. Two possibilities remain. First, energy count calibrations may have been different for the two stopes. We have no confirmable information to assess this possibility. Second, real differences in the damage states around each stope may have existed, creating attenuation differences that could account for the apparent energy release differences between the stopes. This possibility is discussed further in a subsequent section.

The average energy count (EA) for each sequence is the ratio of ET and N. EA for these sequences appears to decline only a little, if at all, between 2 and 16 h after they start. Figures 12*A* and 12*B* show this for stopes 189 and 99, respectively. Once again, EA values are somewhat larger in stope 189 than in stope 99. Both EA and ET are affected by signal clipping, which causes an underestimate of the contributions of larger events. It is possible that more clipped events occur in the first 2 h after progenitor occurrence than in subsequent times. If true, then the

difference between EA at 2 h and at 16 h would be greater than indicated by figures 12*A* and 12*B*. Uncertainty in EA (and ET), however, is due primarily to error in the geometric spreading correction, which in turn, depends upon the distance between the presumed event location and the geophones used to assess maximum waveform amplitudes. With 5 m in location uncertainty, the error in either ET or EA would be less than 25% for most sequences. The geophone stations were not moved in stope 189, and this may account for the very small range of EA values there. Sequences occurring after network changes in stope 99 produced apparently higher EA, with fewer smaller events detected. In general, no significant difference is measured for EA at 2 and 16 h following progenitors in either stope. Any points falling below the equality line in these figures may be due to late contamination.

The apparent constancy in EA after 2 h into a particular aftershock sequence is explained if both N and ET increase at about the same rate during that period. Since dN/dt is characterized by a power law time dependency with negative exponent value between -1 and 0, ET should also be characterized by a similar power law with positive exponent value between 0 and 1. Figure 13 shows two examples of this for stope 189 sequences, starting from about 1.5 h after the progenitor. Not every sequence could be so well fit by a temporal power law because a large aftershock might induce a subsidiary sequence within a few hours of the original progenitor. Nevertheless, in the majority of sequences studied, the relation between the normalized energy counts and time was determined to be well fit by a power law.

Figure 14 shows the relationship between the accumulated aftershock sequence event energies (ET) at 16 h (corrected for geometric spreading) and the local magnitude of the sequence progenitor, as determined independently by surface seismograph records. None of the blast sequences and only some of the blast-bump and bump sequences had assigned magnitudes. We emphasize that here the total energy count ET is not associated with the seismic energy released immediately by the progenitor itself, but rather is related to the sum of all individual aftershock energies. A weak dependence of sequence energy on progenitor size is seen for stope 189 only. The aftershock sequence following the large event (local magnitude M_L = 3.0) near stope 99 in March 1993 is more consistent with this trend between progenitor and aftershock sequence size for stope 189 (figure 14*A*) than for stope 99 (figure 14*B*). The March 1993 event and the majority of its aftershocks were located 50 m to the southwest of stope 99, whereas most other sequences near stope 99 were concentrated around or to the northeast of the stope.

Figure 15 shows the distribution of B-value (BV) for both stopes. Uncertainty in BV arises from both the error of the fit and the error inherent in the energy normalization procedure. Larger BV values indicate a relatively greater proportion of smaller events. There is a clear difference between the mean values of all B-values in the two stopes. This and other differences are assessed in a later section of this report.

PLANARITY

Many aftershock locations in a sequence can be grouped on one or more planes. Poles to the planes containing the most event locations 16 h after progenitor occurrence are shown in lower hemisphere projection in figures 16*A* and 16*B* for stopes 189 and 99, respectively. Table 3 gives the detailed characteristics for all such planes, one per sequence, in both stopes. Other, similar results for two sequences in stope 307 were discussed in the part 1 report (*1*). The error in both strike (S) and dip (D) of these fitted planes is typically ±5°. In table 3, each fitted plane is really a thin ellipsoid approximating a plane. This occurs primarily because the method of finding the plane places potential poles in small, but finite-size, equal-area bins, allowing some orientational flexibility. Additionally, given the uncertainty in event locations, it is unwarranted to require that events be precisely coplanar to be included. The thicknesses of the "planes" appear to be somewhat less, on average, in stope 99 than in stope 189.

Most of the fitted planes are subvertical, dipping less than 10° to either the northwest or southeast (figure 16). However, a substantial number dip at shallower angles. The vast majority of planes in both stopes strike to the northeast, but the dominant directions are more eastward in stope 189 than in stope 99 (figure 17). These dominant plane strikes and dips roughly correspond to the orientation of each stope, following the orientation of the silver vein in the area. Both stopes are subvertical, with stopes 189 and 99 striking approximately N. 70° E. and N. 45° E., respectively. From the mine maps, strikes and dips were tabulated for over two dozen fractures noted within each of the regions encompassed by the geophone networks in the two stopes. Most of these fractures had dips within 20° of vertical, with strikes dominantly between 25° and 35° *west* of north, subparallel to the northwest trend of known major local faults. Thus, the planarity found in the event locations for these aftershock sequences appears to be more associated with the stope or mineral vein than with the joint or fracture sets. Further study, including determination of potential secondary and tertiary planarity, is needed to properly evaluate the physical significance of the inferred planar structures.

Table 3.—Results of planarity searches

Progenitor type and sequence	Percent in-plane[1]	Number in-plane	Strike	Dip	Extent,[2] m
STOPE 189					
BL:					
890321	42	141	N. 14° E.	46° NW.	26,16,4
890322	47	365	N. 4° W.	48° SW.	24,18,4
890331	46	237	N. 71° W.	55° SW.	34,18,8
890403	32	201	N. 76° W.	63° SW.	36,18,6
890406	30	180	N. 51° E.	74° NW.	30,10,3
890629	60	256	N. 45° E.	73° NW.	18,10,3
890714	46	288	N. 45° E.	80° NW.	24,12,4
890720	74	564	N. 45° .E	80° NW.	22,10,4
890907	53	163	N. 3° W.	48° SW.	30,20,4
890919	52	140	N. 15° W.	40° SW.	32,20,6
891004	54	122	N. 61° E.	87° SE.	54,32,6
891005	64	216	N. 66° E.	88° SE.	50,26,5
891009	48	85	N. 61° E.	86° SE.	40,26,3
891010	63	200	N. 67° E.	87° NW.	36,26,3
891011	65	136	N. 61° E.	88° SE.	52,28,7
891211	48	180	N. 5° E.	55° NW.	20,14,4
900118	74	585	N. 66° E.	87° SE.	46,22,5
900119	78	763	N. 60° E.	87° SE.	44,26,6
BB:					
890313	43	476	N. 19° E.	54° NW.	26,20,5
890316	33	178	N. 13° W.	47° SW.	28,18,4
890912	35	505	N. 67° E.	87° NW.	38,26,4
890921	48	123	N. 40° W.	47° SW.	32,16,4
891205	39	124	N. 5° W.	67° SW.	16,16,3
891215	23	120	N. 80° W.	86° SW.	16,12,4
891219	23	129	N. 15° E.	55° SE.	24,16,4
900102	38	333	N. 60° E.	85° SE.	34,28,5
900104	66	427	N. 49° E.	85° SE.	44,28,6
900110	69	847	N. 46° E.	86° SE.	48,18,6
900112	62	106	N. 33° E.	88° SE.	52,40,8
900116	66	427	N. 59° E.	87° SE.	44,28,4
900117	76	784	N. 61° E.	87° SE.	44,26,6
900123	76	424	N. 66° E.	87° SE.	46,24,6
900124	70	288	N. 61° E.	86° SE.	46,26,6
900306	62	389	N .48° E.	85° SE.	34,24,6
900307	36	488	N. 12° W.	87° SW.	44,38,5
BU:					
890325	32	222	N. 14° E.	47° NW.	24,24,6
890715	54	246	N. 44° E.	80° NW.	26,12,5
890804	49	504	N. 39° E.	87° SE.	28,16,4
890805	58	695	N. 34° E.	87° SE.	28,20,5
891120	34	93	N. 6° W.	86° SW.	42,14,6
STOPE 99					
BL:					
891228	48.5	573	N. 54° E.	88° NW.	28,15,2
900406	29	96	N. 83° W.	87° NE.	30,20,4
900511	34	163	N. 43° E.	80° SE.	48,24,2
900830	43	165	N. 17° W.	27° SW.	20,16,3
900907	52	120	N. 49° E.	32° NW.	18,8,3
901220	27	75	N. 83° W.	6° SW.	30,14,2
910117	43	131	N. 4° E.	22° NW.	24,14,3
BB:					
891011	32	118	N. 43° E.	82° NW.	34,18,2
891018	24	68	N. 44° E.	82° NW.	34,30,4
891020	30	112	N. 48° E.	86° SE.	32,20,2

See explanatory notes at end of table.

Table 3.—Results of planarity searches—Continued

Progenitor type and sequence	Percent in-plane[1]	Number in-plane	Strike	Dip	Extent,[2] m
STOPE 99—Continued					
891119	38	110	N. 76° E.	46° NW.	32,20,3
891227	39	187	N. 62° E.	86° SE.	44,24,4
900104	47	167	N. 25° E.	80° NW.	24,18,2
900105	48	264	N. 47° E.	89° NW.	28,18,2
900109	41	112	N. 55° E.	87° SE.	24,20,2
900110	44	109	N. 39° E.	73° NW.	32,20,2
900202	50	296	N. 53° E.	88° SE.	36,18,2
900219	45	221	N. 73° E.	87° NW.	40,26,3
900504	18	83	N. 67° W.	87° SW.	36,24,2
900615	36	402	N. 55° E.	28° NW.	32,12,5
900913	44	262	N. 62° E.	20° NW.	18,10,3
901009	40	114	N. 36° E.	36° NW.	30,12,2
901011	40	173	N. 41° E.	89° NW.	26,18,2
901019	30	143	N. 79° E.	87° SE.	20,16,2
910103	40	106	N. 29° E.	25° NW.	18,12,2
910108	46	153	N. 30° W.	13° SW.	16,12,2
910111	42	98	N. 48° E.	34° NW.	16,12,2
910205	35	161	N. 72° W.	81° SW.	28,20,4
911003	31	62	N. 46° E.	15° NW.	20,10,2
911025	53	93	N. 5° E.	88° NW.	32,24,2
911030	34	72	N. 6° E.	86° NW.	34,24,4
911108	32	53	N. 46° E.	21° NW.	26,18,2
911223	42	96	N. 38° E.	35° NW.	24,10,2
BU:					
891229	59.5	353	N. 54° E.	88° SE.	28,16,4
900207	29	145	N. 87° W.	67° NE.	30,18,2
901118	34	78	N. 20° E.	15° NW.	26,16,2
911029	43	131	N. 6° E.	88° NW.	36,22,2
930318	38	133	N. 53° E.	87° NW.	66,30,5

[1]Percentage of all located aftershocks 16 h after progenitor occurrence.
[2]Half-lengths of axes of the best fitting ellipsoid encompassing only coplanar events.

STATISTICAL COMPARATIVE ANALYSES

Significant differences may be apparent when attributes of two specific aftershock sequences are compared. In this section, a general comparison of all aftershock sequences with regard to progenitor type and nearby stope is considered. However, we will exclude the stope 99 sequences that occurred following the network change in March 1991. Table 4 lists the characteristics of the ensemble attribute distributions broken out according to progenitor type and stope. Both median and mean values are given. The median value is considered more characteristic since many of the attribute values are not symmetrically distributed about the mean. As indicated in a previous section, within the uncertainty of the calculations, most individual sequence attribute values were stationary for periods between 2 and 16 h following the progenitor. Accordingly, there is very little difference between the attribute *distribution* characteristics measured at 2-, 4-, 8-, or 16-h periods. However, for a truly fair comparison, the same period of observation should be used throughout. Only the distribution values measured for the 2-h period following the progenitor are given in table 4. Although not in table 4, distributions of strikes and dips of the best fitted planes determined with 16-h data were also statistically compared.

To assess the differences between distributions of a particular attribute, we applied a two-sided Kolmogorov-Smirnov statistical test (hereafter referred to as the "K-S" test). The K-S test is a nonparametric test that compares the differences between two cumulative distributions of attribute values with the Kolmogorov distribution. The significance of the maximum deviation is assessed taking into account the number of data used to define each of the distributions being compared. In practice, the maximum deviation between the cumulative distributions is used to test the null hypothesis that there is no difference between the distributions (*15*). Acceptance or rejection of this

hypothesis is made with a certain level of confidence. The K-S test was applied to each attribute distribution listed in table 4, as well as to the planarity results presented above, comparing blast (BL), blast-bump (BB), and bump (BU) distributions for each stope, and comparing the two stopes with each other.

K-S test results are summarized in figure 18 for the most probable differences. One can reject the null hypothesis at the 95% confidence level for attributes BV, DR, CV, SR, D, EA, and ET when comparing the two stopes without regard to sequence progenitor. In other words, there is a very high probability that these attributes are different for the sequences measured in the two stopes. However, there is much less evidence to believe that there is any difference between the stopes just on the basis of comparing attributes TF, SF, AD, or N. The only evidence is that SF appears to be somewhat smaller for BU sequences, and AD is smaller for BL sequences in stope 99 than in stope 189. For both of these cases, one can reject the null hypothesis at only the 80% confidence level. Within each stope, only a few significant attribute distribution differences are noted between BL, BB, and BU sequences. At the 95% null hypothesis rejection level, only attributes AD and EA are different for stope 99 BB and BL sequences. At the same confidence level, only EA is different for stope 189 BB and BL sequences, and CV is different for stope 189 BU and BB sequences. One can also say, with less confidence (at the 90% null hypothesis rejection level), that stope 189 has different N values for BL sequences than for either BB or BU sequences. At that same 90% rejection level, stope 99 has different CV values when comparing BB with BU sequences, and different BV's between BU and BL sequences. The null hypothesis can be rejected, but with even less confidence (85% level), when comparing attributes EA and AD between BU and BB sequences in stope 99. Finally, in stope 189, the null hypothesis can be rejected with only 80% confidence for the SF and TF attribute distribution comparison between BL and either BB or BU sequences. For all other potential distribution comparisons, rejection of the null hypothesis was even less warranted.

The K-S test can also be used to confirm the general lack of attribute distribution dependence on observational window size, if used to compare the 2- and 16-h periods. Such tests confirm what can be seen in preceding figures. Only the distributions for attributes DR, N, and ET change significantly as time progresses after progenitor occurrence. Determination of these attributes will depend on the period of observation used.

The relationship between total length of production blasting holes (LT) drilled and BB sequences was significantly different in both stopes. In stope 189 there was a greater probability of producing blast-associated bumps with greater length of hole blasted, whereas in stope 99 most of the production blasts that we studied produced bumps, independent of the total length of hole blasted. Although this observation may be a byproduct of the sequences chosen (17 out of 40 in stope 189 and 26 out of 37 in stope 99 were BB sequences), examination of the mining logs over the same 2 year period confirms the general impression that stope 99 had more frequent small bumps than stope 189 during production work. This is in spite of the fact that LT values were typically lower in stope 99 than in stope 189 (table 4). Nevertheless, in both stopes, blasts not followed by bumps generally had fewer events and released less energy in their aftershock sequences than those followed by bumps.

Cross-correlation coefficients for the distributions of attributes measured 2 h into the sequences are given in tables 5 and 6 for stopes 189 and 99, respectively. The low values in most cases support the essential independence of the attributes. The cumulative energy count ET and the number of aftershocks N were correlated in each stope, which is consistent with the small range of the average energy counts (compare figure 12). A modest negative correlation was observed between the average interevent distance AD and the skewness ratio SR in stope 189. In stope 99, a modest negative correlation was observed between the coefficient of variation CV and the decay rate DR, as well as between the decay rate and the cumulative energy counts. A positive correlation was observed between the coefficient of variation and the cumulative energy count in stope 99.

Table 4.—Comparison of stope attributes

Progenitor type and attribute[1]	Stope 189		Stope 99	
	Median	Mean and std dev	Median	Mean and std dev
BL:				
SF	1.72	1.71 ± 0.27	1.72	1.72 ± 0.12
AD	30.6	27.7 ± 6.8	20.4	19.4 ± 3.3
SR	3.79	4.12 ± 2.5	4.19	5.51 ± 1.8
TF	0.83	0.82 ± 0.07	0.76	0.75 ± 0.10
DR	-0.54	-0.55 ± 0.11	-0.69	-0.62 ± 0.21
CV	1.36	1.40 ± 0.16	1.53	1.63 ± 0.15
N	207	246 ± 139	255	345 ± 138
EA	1.77e7	1.72 ± 0.54e7	4.59e6	4.38 ± 1.78e6
BV[2]	1.4	1.5 ± 0.4	0.85	0.85 ± 0.13
LT	41.2	48.8 ± 21.9	29.3	30.2 ± 9.1
BB:				
SF	1.92	1.92 ± 0.19	1.8	1.74 ± 0.28
AD	26.7	28.2 ± 9.6	29.4	31.9 ± 15.8
SR	2.76	3.44 ± 2.5	4.07	4.59 ± 2.0
TF	0.78	0.80 ± 0.10	0.83	0.81 ± 0.07
DR	-0.6	-0.53 ± 0.18	-0.74	-0.80 ± 0.2
CV	1.47	1.49 ± 0.3	1.66	1.84 ± 0.5
N	244	310 ± 189	279	346 ± 184
EA	1.44e7	1.65 ± 0.58e7	5.53e6	9.1 ± 1.11e6
BV[2]	1.2	1.3 ± 0.4	0.87	0.95 ± 0.22
LT	56.1	66.8 ± 24.4	31.7	35.4 ± 14.9
BU:				
SF	1.9	1.94 ± 0.16	1.6	1.58 ± 0.16
AD	22.7	29.1 ± 12.8	22.1	22.2 ± 3.6
SR	4.1	4.30 ± 2.4	4.9	5.9 ± 2.63
TF	0.88	0.81 ± 0.11	0.77	0.75 ± 0.13
DR	-0.52	-0.45 ± 0.10	-0.68	-0.76 ± 0.21
CV	1.23	1.24 ± 0.08	1.49	1.68 ± 0.4
N	329	331 ± 190	281	328 ± 212
EA	1.45e7	1.60 ± 0.39e7	2.99e6	3.98 ± 3.24e6
BV[2]	1.5	1.5 ± 0.4	1.3	1.2 ± 0.13

[1]Values determined 2 h after sequence initiation. See table 2 for attribute label identification. AD and LT are in meters. The normalized energy average EA is in meters squared-millivolts. All other attributes are dimensionless.

[2]Values calculated from log number versus log normalized energy data.

Table 5.—Attribute cross-correlation coefficients[1] for stope 189

Attribute	SF	SR	AD	TF	DR	CV	N	ET	BV
SF	1.00								
SR	0.14	1.00							
AD	-0.25	-0.71	1.00						
TF	0.08	-0.31	-0.06	1.00					
DR	0.36	0.22	-0.13	-0.01	1.00				
CV	0.07	0.17	-0.36	-0.35	-0.47	1.00			
N	0.30	-0.13	-0.01	0.48	0.21	-0.10	1.00		
ET	-0.33	0.03	-0.09	0.40	0.29	-0.20	0.87	1.00	
BV	-0.12	0.38	-0.32	0.00	0.12	0.08	0.02	0.00	1.00

[1]Attribute values determined 2 h after sequence initiation.

Table 6.—Attribute cross-correlation coefficients[1] for stope 99

Attribute	SF	SR	AD	TF	DR	CV	N	ET	BV
SF	1.00								
SR	-0.35	1.00							
AD	0.32	-0.24	1.00						
TF	0.41	-0.12	0.38	1.00					
DR	-0.05	0.28	-0.43	-0.31	1.00				
CV	0.04	0.23	0.49	0.10	-0.74	1.00			
N	0.31	-0.30	0.00	0.56	0.14	-0.31	1.00		
ET	0.15	-0.01	0.59	0.24	-0.61	0.76	0.91	1.00	
BV	-0.24	0.11	0.00	-0.01	0.16	-0.17	0.01	-0.40	1.00

[1]Attribute values determined 2 hours after sequence initiation.

CLASSIFICATION PROCEDURES AND ANALYSIS

Each stope can be represented by a matrix of attribute values determined for a common postprogenitor period. There are four such matrices for each stope, corresponding to the 2-, 4-, 8-, and 16-h postprogenitor periods. The rows of the matrix are the individual aftershock sequences, and the columns of the matrix are the attributes described above. The aftershock sequence attributes may involve incompatible units of measure and may span different orders of magnitude. Some (SF, SR, TF, CV, BV, N) have no units at all. This will affect attempts to cluster and classify sequences based upon selected attributes. As a remedy, each attribute was normalized in the following way. For each stope, each attribute measure was divided by the range span of all like attribute values in the sequence. This produces, for each matrix attribute component, a nondimensional number between zero and one. For the attribute of major plane strike, 90° W. to 90° E. was mapped from zero to one. Similarly, for the major plane dip, 0° to 90° was mapped from zero to one. Inevitably, some information is lost in this type of normalized compression. Also, if the attribute matrix is subsequently enlarged by the addition of other individual sequences, the normalization may have to be redone. However, this normalization avoids introducing potentially subjective weighting to each attribute value in order to bring all into a common nondimensional base and magnitude scale. It also avoids assumptions about the form of statistical distributions of the attribute values.

For various reasons, not all the attributes listed in table 2 could be measured for each sequence and for each time period. Methods exist for filling in missing attribute data in a way that does not affect the distributions, but we elected not to use such methods. If a measure of an attribute in one or more sequences was not available, we did not use that attribute at all to cluster and classify the sequences for that time period. For example, in some cases it may not have been possible to adequately fit a power law to the event rate decay after 8 h of a specific sequence, so attempts to cluster the sequences using that attribute were limited to prior-time attribute values.

As many as 44 attribute measures were compiled for each aftershock sequence (i.e., the 10 attributes listed in table 2 that were measured at 2, 4, 8 and 16 h after progenitor occurrence, and the attributes LT, M, S, and D, which were measured only once). Many classification exercises were carried out on subsets of these attributes. The same attributes, measured at different times, were never included in the same subset. Furthermore, only two of the EA, N, and ET attributes were used at any one time since they are not mathematically independent. At most, then, 13 attributes were used for any one classification exercise. Typically, nine or fewer attributes were used in any single classification exercise. Additionally, only spatial or only temporal or only size subgroups of attributes were separately studied.

The general procedures of mathematical taxonomy or classification analysis, as described in appendix A, were followed. This enabled us to form potential classes of sequences for each stope, *without regard to the nature of the sequence progenitors*. The results of each classification exercise were then examined for potential usefulness. Lastly, as a test of the hypothesis that stopes have a unique style of aftershock response, all of the sequences from both stopes 189 and 99 were combined, and subsequently an attempt was made to form two distinct groups *without regard to parent stope*. The subsequent groupings were examined to see if the aftershock sequences were classified by parent stope and what selection of sequence attributes best accomplished this.

Pictographic representations of the aftershock group associations, called dendograms, are shown in figures 19 and 20. In the dendograms, the strength of the association between any two sequences is measured inversely by the length of the path along the lines connecting them. Very

similar sequences, determined by the attributes used in the classification, are near each other in the dendogram tree structure, while less similar sequences are farther apart.

Figure 19 is an example result for the 31 pre-network-change sequences near stope 99, classified using attributes DR, CV, SR, AD, and EA and the centroid clustering method (compare figure A-5 in appendix A). The first six sequences form a single class characterized by relatively high average event energies. The next four sequences form another class characterized by relatively high skewness ratios. The last sequence had such a low event rate decay that it was assigned to a class by itself. In this example, no grouping by progenitor type is easily identifiable. Few trials, with other attributes and different clustering methods, produced classes that could be characterized simply by sequence progenitor type. This is not surprising given the few significant differences between sequences with different progenitor types (figure 18).

Figure 20, in which all the sequences for stopes 189 and 99 are combined, shows that aftershock sequences can be correctly assigned to their parent stope in almost all cases. Misclassified sequences are underlined. Only three stope 189 sequences and two stope 99 sequences were misclassified. This classification was accomplished using attributes DR, CV, SR, and EA, with dissimilarity measured by simple Euclidean distance after the attributes were normalized by total range. The complete-link clustering method was used (compare figure A-2), although there was almost no classification difference when using the between-group method (compare figure A-4). In contrast to figure 19, the good separation of sequences into classes according to stope of origin is accomplished because of the greater number of attributes with significant differences between the stopes (figure 18).

CHANGES IN ATTRIBUTES AS MINING PROGRESSES

Each stope is a dynamic entity, responding to mining activity on various time scales. Viewed over the working life of a stope, each aftershock sequence can be considered to be a snapshot of the stope's response to a rapid stress perturbation caused by the progenitor. Consequently, as mining progresses, trends or changes of aftershock sequence attributes may hold information about near-stope conditions. Figures 1 and 2 above delineate geometric changes in mined-out areas over periods of about 1 year in stope 189 and about 2 years in stope 99. Progress in stope 189 ended with the rock burst sequence identified as 900307 in table 1. Stope 99 was monitored into 1993. However, progress in it ended in June 1992 when mine-wide production was halted.

Sequence attributes are plotted as a function of progenitor occurrence time in figures 21 through 30. Observations can be made with respect to the progress of mining in stopes 189 and 99 as delineated in figures 1 and 2, respectively. However, care must be exercised concerning any conclusions about temporal trends in the data. The times between occurrences of the selected sequences are not uniform, and unmeasured, intervening sequences could disrupt perceived trends. Additionally, the uncertainty in attribute measures must be considered. Typical uncertainties are listed in table 2. Differences between any two measurements may be significant if greater than the uncertainty level. Over a period of time, however, a real trend will appear only when such significant differences persist.

Figure 21 shows that, with only a few exceptions, SF attribute values were within the range of 1.6 to 2.3 for both stopes. No strong temporal trends were discernible in either stope. Except for the four low values for BL sequences in stope 189 in October 1989, there would be no differences in median SF values for BL, BB, and BU sequences in that stope. These four sequences were initiated by smaller than average production blasts (on one side of the stope in three cases), and activity was apparently more clustered near the blasted area. However, the average distance between event locations for those four sequences was relatively high (figure 22*A*). These relatively high AD were obtained because, aside from the single major cluster near the blast area, other event locations in each sequence were more thinly spread throughout the region encompassed by the geophone network. Sequences that occurred after the stope 99 geophone network change in April 1991 displayed, on average, somewhat lower SF values than prior sequences (figure 21*B*). In this case, however, the increase in degree of clustering may be more of a network artifact than real, because smaller events were less detectable and locatable after the network change. This fact also shows up in the very high average AD values after the network change (figure 22*B*).

The average interevent distances showed some interesting trends. In stope 189, AD values for all sequence types generally increased from July through November 1989. In the third quarter of 1989, work was concentrated near the 189 raise, expanding eastward and westward (figure 1), and this may account for the more than doubling of the AD values during this period. A similar situation occurred beginning in December of that year and continued on into 1990 in that stope. In contrast, stope 99 AD values diminished from about 30 to 20 m for

all sequence types (figure 22*B*) as the remnant pillar to the east of the 99 raise was mined out.

The skewness of the interevent distance distribution seems to be inversely correlated to the average interevent distance in stope 189 (figure 23*A*). If one ignores the post-network-change sequences, a similar, but very much weaker trend occurred in stope 99 (figure 23*B*). High SR values combined with low AD values indicate event location clustering, a fact already quantified by the spatial fractal dimension, and easily verified by examination of location plots as in figure 3.

Although there were several low values for the TF attribute in both stopes, no strong trend was evident in either stope (figure 24). Even after the network alteration in stope 99, the temporal clustering of event triggers in aftershock sequences was essentially indistinguishable from that in previous sequences. This implies that the less complete set of larger events captured by the altered network was similarly distributed in time as prealteration sequence events.

Sequences of all progenitor types tended to decay at slower rates in stope 189 than the same sequence type in stope 99 (figure 25), although sequence rate decay was more variable in stope 189 (figure 25*A*). In stope 99, the DR attribute was additionally affected by the inability of the altered geophone network to detect small events (figure 25*B*). This caused an apparently more rapid event rate decay in the last six sequences studied. During the third and fourth quarters of 1989, blast-induced sequences (BL) tended to decay at faster rates as mining progressed outward on both sides of the 189 raise (figure 25*A*). When the next level upward was started in December 1989, sequence rate decays were slower again.

Neglecting the post-network-change period in stope 99, variability in the CV attribute was about the same for both stopes, although stope 189 had a significantly lower median value (figure 26). A trend of decreasing CV values in stope 189 followed damaging bumps in both August and November 1989. No similar trend is seen in stope 99.

Total sequence energy count, 16 h after progenitor occurrence, tended to decrease during the third and fourth quarters of 1989 in stope 189 (figure 27*A*) and during the entire monitoring period prior to network change in stope 99 (figure 27*B*). This trend was independent of progenitor type and embodies almost an order of magnitude decrease in both stopes. Following the November 1989 bump in stope 189, ET tended to increase. This corresponds with the noted slower event rate decays for the same period in that stope (figure 25*A*). However, the average event energy count in stope 189 sequences did not show an increase during this period (figure 28*A*). Rather, sequence EA values during this period were stable or decreasing. One must conclude that this is due to generally larger numbers of events in sequences occurring in 1990 in stope 189, and this is substantiated in table 1. Average event energy counts for stope 99 sequences showed no trend throughout the period before the network change (figure 28B).

A trend of decreasing B-values was noted during two periods of time. These occurred during the third quarter of 1989 in stope 189 (figure 29*A*) and during the fourth quarter of 1990 into the first quarter of 1991 in stope 99 (figure 29*B*). Stope 189 was being mined on both sides close to the raise, but at slightly different levels during the third quarter of 1989 (figure 1). The last remnants of the residual pillar were being mined in stope 99 near the end of 1990, and this was completed by March 1991 (figure 2*A*). A possibly increasing BV trend during March and April 1989 in stope 189 was also noted. For other periods of time, trends in BV were not discernible.

Most of the larger magnitude progenitors spawned aftershock event locations whose primary fitted plane was close to vertical (figures 30*A*-30*B*). An interesting change in the planarity occurred for stope 99 sequences following the destress blast on June 15, 1990. Unusually shallow-dipping, fitted planes dominated thereafter for the smaller progenitor sequences. These tended to strike in the same northeast direction as most of the other fitted planes (compare figure 16*B*). A cross-sectional view of the 900615 aftershock sequence locations is shown in figure 31. Nothing as remarkable as this change in plane dip was observed in any of the other attributes during this time period. A previous destress blast (sequence 900202) was not followed by significant changes in aftershock location planarity, but was followed by greater than average seismic activity (*10*).

AFTERSHOCK SEQUENCE AFTER MINING WAS SUSPENDED

Production throughout the Galena Mine was suspended in June 1992. The geophone network near stope 99 at that time was left in place and continued to monitor local seismicity. Subsequently, overall seismicity rates began an exponential decline. Eight months later, on March 18, 1993, a magnitude 3.0 rock burst occurred about 50 m to the southwest of stope 99, near another vein and stope. This occurrence provided an opportunity to study an aftershock sequence virtually uncontaminated by mining activity. The sequence was analyzed in the same manner as the others had been for periods of 16 h, 7 days, and 43 days following the progenitor.

Table 3 indicates that the strike and dip of the best-fitted plane was N. 53° E., 87° NW., containing 38% of all

locations, much the same as other bump (BU) sequences in stope 99. However, the spatial limits of this plane were much greater than previous fitted planes. The average and median values for the AD attribute at 16 h were about 40 and 75 m, respectively, which is substantially larger than for previously examined stope 99 sequences (figure 5*B*). Additionally, the SR attribute was about 2.5, which is significantly lower than for previous BU sequences near stope 99 (figure 6*B*). The other spatial attribute, SF, ranged from 1.74 at 16 h to 1.85 after 43 days. Taken together, these measures indicate that the degree of event location clustering was about the same as for previously studied BU sequences in this stope (figure 4*B*), but the volume containing the events was significantly larger, and the density of well-located events was less.

The temporal fractal dimension, TF, was 0.91 ± 0.03 after 16 h. This value is at the upper end of the range of previous sequences near stope 99 (figure 8*B*). The event rate decay exponent at 16 h was -0.57 ± 0.05, lower than sequences previously studied that occurred after the network change in 1991 (figure 25*B*). The CV attribute at 16 h was 1.67, which is about average and essentially indistinguishable from the other BU sequences previously studied in this stope (figure 10*B*). Taken together, these measures indicate that, at least for the first 16 h, aftershocks occurred more slowly, with apparently less clustering in time than other sequences previously studied.

Total normalized energy counts after 2 h and after 16 h were determined to be 1.9×10^{10} and 2.6×10^{10}, respectively. At the same times, average event energy counts were 5.1×10^{7} and 3.7×10^{7}, respectively. All of these values are higher than the corresponding values measured for prior sequences near this stope (compare figures 11*B* and 12*B*). The B-value at 16 h was 0.3, which is quite low. This indicates either an unusual abundance of larger aftershocks or a deficiency in the number of smaller events located. Most of the events in this sequence were generally farther away from the stope 99 networked geophones than the prior sequences studied. Overcompensation for geometric spreading is one possible reason for the larger energy count values. Loss of detectable and locatable small events due to more attenuation is a possible reason for the low B-value.

DISCUSSION

SPATIAL ASPECTS OF AFTERSHOCK ACTIVITY

The stopes are essentially thin, prismatic voids that efficiently concentrate stresses along their smallest dimension. Additionally, as mining proceeds upward in the stope, the overlying residual pillar diminishes, and horizontal stresses in it increase. The prevailing state of stress for the two stopes studied had the maximum principal stress horizontally oriented within 15° of N. 45° W., with the intermediate and minimum principal stresses being roughly equal to the vertical overburden (*9*). The minimum principal stress is horizontal. This situation favors relatively high shear stress concentrations on the eastern and western stope boundaries. Since blasting also tends to occur on stope boundaries, there is no surprise in finding aftershocks clustered there following blasts (figure 3). Following bumps and rock bursts not immediately preceded by blasting, aftershock locations were included in a larger rock mass volume, as well as clustered in the same stope boundary areas.

Gresseth and Reid (*16*) studied mining-induced fractures in a nearby mine with similar tectonic fabric and mining practices. They found that, as the stope evolved, there was a tendency to shift the stress state from one favoring slip on the prevailing fracture sets to slip on planes subparallel to the stope. Both northwest-trending and northeast-trending fractures were activated during a stope development cycle. In another nearby mine, Scott (*17*) determined that only 6% of microseismic events were associated with known strike slip faults. Of the events he studied, 73% occurred more than 6 m from any mine opening. Examinations of shear zones intersecting tunnels following rock bursts in a deep gold mine indicated that failure of intact rock was involved (*18-19*). McGarr and others (*19*) found that although there were abundant geological faults and joints, the faulting associated with the tremors did not show any marked tendency to follow preexisting faults. Fractures were mapped in stopes 189 and 99 prior to, but not following, the progenitors in this study. These maps show a northwest-trending fabric, subparallel with larger regional fault structure. However, without focal mechanism data for the aftershock events, we cannot associate individual events with specific fractures or faults. From focal mechanism studies at two mines, Urbancic and others (*20*) concluded that microseismicity generally occurs along the most significant mapped fractures. There is no doubt, based on the present observations and prior studies associating blasting with near wall damage (e.g., *21-23*), that new fractures were formed and repeatedly activated near the stopes. Given that the dominant planarity in the aftershock locations is subparallel to the stopes and not the preexisting fracture system, it is possible that such planes include events occurring both on older and newly formed fractures.

In contrast to most earthquake studies, this study found little evidence to suggest that aftershock locations near a

stope predominantly cluster along a common parent fault structure. Rather, planarity in the aftershock locations was more easily associated with the local vein being mined. The vast majority of sequences studied here failed to show that aftershocks were confined to only one or two planes corresponding to known major fractures or fault structures that trend in the northwest direction (figure 17). Swanson (*9*) determined that large events occurred on a northwest-trending planar array in this mine. It is not clear that aftershocks for those events did likewise. For example, a focal mechanism for one of those events (stope 99, event 900207.122021) had a N. 45° W. nodal plane (*10*), yet the associated aftershock sequence event locations indicated only a weakly determined plane (29% of all high-quality locations) striking almost east-west (table 3). In addition to the general tendency for aftershock event location clusters to form near the stress-concentrating boundaries of the stopes, the residual pillar size may have a strong effect on any planarity determinations. For example, the dramatic change in the dip of fitted planes in stope 99 for the last half of 1990 and the first quarter of 1991 coincides with the last stages of removal of the residual pillar (figure 2*A*). In general, however, if individual event locations indicate the presence of a structural discontinuity, then the aftershock location patterns studied here suggest a volumetric, rather than simply planar, distribution of damage in most cases.

The spatial fractal dimension was determined over the range of 4 to 32 m. The median spatial fractal dimension for the aftershock sequences was about 1.9 and 1.8 for stopes 189 and 99, respectively (figure 21). Even after mining activity had long ceased, a BU sequence had about the same SF value over a range of 4 to 64 m. Previously (*1*), we looked at a continuous determination of SF in stope 189 and found a median value of about 2.5 for a 60-day period that included relatively inactive periods as well as blasts and bumps. Since random locations should eventually be space-filling and have SF equal to about 3.0, we interpret the SF value of the aftershock sequences to mean that they are considerably more spatially clustered than the usual background. For comparison, we note that Eneva and Young (*24*) also used the correlation dimension to study temporal changes in seismicity in a working hard-rock mine. They found a spatial fractal dimension of about 1.7 over the range of 15 to 121 m for a 160-day period. Shorter term values were often much lower.

The persistent spatial fractality of the aftershock locations over many months indicates that the organization of parent fractures in the rock mass is also likely to be fractal over the same scale ranges (*25*). The stress perturbation associated with each sequence progenitor tests the preexisting distribution of fractures as the sequence proceeds; each aftershock is a failure of a member of this population. The persistent fractality in the same region, without long-term trend, sequence after sequence (figure 21), argues for a continual replenishment, rather than exhaustion, of the *active* fracture population. This can be accomplished by either repeated slipping of many of the same fractures or by creation of new fractures. If aftershock event locations from two different aftershock sequences occupy much the same volume, the sequence with the lower SF value sampled the volume when it was more seismically heterogeneous. It is important to realize that this greater seismic heterogeneity can be caused *either* by an increase in fracture density in a portion of the volume *or* by fewer, repeatedly active members of the preexisting fracture population. Both situations could reduce SF.

TEMPORAL ASPECTS OF AFTERSHOCK ACTIVITY

Most of the aftershock sequence attributes were relatively unchanged when viewed from the 2- or 16-h windows. For any particular sequence, if the majority of events occurred within the first 2 h, then data from that window would dominate data in longer windows, and this would explain the lack of difference between 2- and 16-h values. However, the ratio of the median number of event triggers accumulated within 2 h to those accumulated by 16-h after progenitor occurrence was about 35% and 45% for stopes 189 and 99, respectively. (This difference between the stopes is also evident in the differences in event rate decay noted in table 4). Therefore, the data based on a 16-h window of observation is not typically dominated by the data from the first 2 h. Some other explanation must be found for the stable values of those sequence attributes that apparently are well established within 2 h of progenitor occurrence.

Most SF values indicate that strong event location clustering occurred in the first 2 h. After that, additional event locations, random or not, did little to diminish the strength of the clustering (figure 3). After 2 h, the addition of events not located in the clusters tended to slightly increase the average interevent distances (figure 5) and also to slightly modify the highly skewed interevent distance distribution (figure 6). All three attributes suggest that the spatial organization of events was well established within 2 h and was maintained for up to 16 h after progenitor occurrence. Although the high shear stresses available near the stope boundaries are part of the reason for the cluster persistence, other clusters of events occurred in the rock mass away from the stopes (figure 3). The aftershock sequence following the March 1993 event (local magnitude M_L = 3.0) in the rock mass near stope 99 did not decluster even after 43 days (SF = 1.74 and 1.85 at 16 h and 43 days, respectively, whereas aftershock numbers increased from 350 to 998). These observations can be explained if newly created fracture surfaces or slipping preexisting fractures engendered *nearby* newer damage during

a sequence. The newer damage might simply have been repeated slip on the same fractures. The size or density of event location clusters away from the stope might be related to the occurrence of a larger aftershock within the first 2 h following the progenitor that, subsequently, created its own aftershock cluster nearby.

The demonstration of temporal fractality in aftershock occurrences argues for scale independence in the time domain. One interpretation of this is that, within the overall sequence, each aftershock produces its own aftershock sequence, members of which produce their own subsidiary sequences, and these continue downward in diminishing duration. Secondary and tertiary embedded aftershock sequences are often manifested by short jumps in event rate (compare figure 7), but do not significantly alter the degree of temporal clustering (figure 8). The duration of each subsidiary sequence might depend on the size of each aftershock. In this interpretation, the entire aftershock sequence ends when local strength thresholds are no longer exceeded by stress or strain changes induced by prior aftershocks. The overall sequence is a superposition of old and new sequences embedded throughout. This creates the clustering of event occurrences, the strength of which is inversely related to the temporal fractal dimension TF. Contrast that situation with random event occurrences, independent from each other, but classified as aftershocks simply because they occurred after the sequence progenitor. Even random event occurrences can be somewhat clustered, however. Sequences with TF values closer to 1 (random clustering) are those with either fewer detected subsidiary sequences or greater contamination from random background events not related to the sequence progenitor.

There was no apparent correlation of the temporal fractal dimension or the rate decay exponent with the progenitor type in either stope. This implies that the rock mass response to a stress perturbation was relatively blind to the stress change mechanism, reacting more to the stress change magnitude. In fact, for those progenitors where a local magnitude was obtainable, a weak dependence of DR on M is evident in both stopes (figure 32). This observation is at odds with some theories of aftershock occurrences that explicitly predict aftershock rate decay to be independent of the main shock magnitude (e.g., *26*). The data in figure 32 are for DR 4 h after progenitor occurrence. The dependence of DR on M is somewhat stronger for longer times after progenitor occurrence.

Several attributes were correlated with the date of progenitor occurrence (i.e., the place where production was occurring). For example, a trend of decreasing DR (greater rate deceleration) for blast-induced sequences was previously noted for stope 189 (figure 25*A*), during the third and fourth quarters of 1989. Combined with the significant differences in DR observed between the two stopes, this could be used to support theories that relate DR to structural heterogeneity or damage. Unfortunately, the use of DR in this context is ambiguous. Progenitors that have rapidly decaying aftershock sequences (more negative DR values) may have attenuated responses either because there are fewer potential seismic sources available in the rock mass or because previously accumulated local damage shields more distant fractures from the stress perturbation associated with the progenitor. Either way, a case could be made that stope 189 was less heavily damaged than stope 99 in most, but not all, near-stope regions. This would be consistent with the smaller, and presumably more highly damaged, residual pillar and its eventual partial removal in one section of stope 99, prior to April 1991. DR values for stope 99 after that date can be discounted because of the subsequent network alteration.

Another piece of information possibly related to damage evolution in the stopes is provided by the average interevent distance and total energy liberated during an aftershock sequence. A continual, general decline in both AD (figure 22*B*) and ET (figure 27*B*) for blast-induced sequences in stope 99 was observed as one section of the residual pillar was totally consumed. These observations may be taken as evidence for *either* smaller, more concentrated seismically active fractures, *or* greater attenuation and shielding effects as the stope evolved.

SIZE ASPECTS OF AFTERSHOCK ACTIVITY

In general, there were poor correlations between the spatial or temporal attributes and the energy or size attributes for the stopes studied (tables 5 and 6). One exception to this was found when examining the blast (BL) sequences alone. BL sequences are those that did not induce any recorded bump(s) soon after the production blast. Fewer events typically occur in BL than in blast-bump (BB) sequences (table 4). Figure 33 indicates that, for both stopes, there was a positive correlation between the spatial fractal dimension and the total sequence energy count for these BL sequences. That is, more seismic energy was released during the sequence when events were less spatially clustered. Higher degrees of event clustering occurred when events were mostly confined to the immediate area surrounding the holes blasted (compare figures 3*A* and 3*C*). These events were probably associated with the new local fractures created at the time of the blast. If energy released per event (EA) can be associated with the average size of the parent fractures, then these near-stope fractures are possibly smaller than active fractures farther out in the rock mass. However, this hypothesis has yet to be tested. We also cannot entirely rule out the effect of event location errors on normalized energy attributes. Location errors may be greater for the sparser locations near the geophone network boundaries.

Previously (figure 24 in reference 1), we indicated a negative correlation had been found between spatial fractal dimensions and B-values for stope 189. With a fuller data set, we cannot support that assertion now (figure 34). In fact, BV is not strongly correlated with any of the attributes evaluated in this study (tables 5 and 6). Recall that BV is determined from the slope of a log-log fit of number of events versus normalized event energy. It is related to, but is not equivalent to, the more commonly presented b-value that associates the numbers of events with their magnitudes. If progenitor energies scale in the same manner as their aftershocks, our calibrations using the surface seismograph indicate that dividing BV by approximately 1.3 will give the b-value. Trifu and others (*27*) found no correlation between b-value and spatial correlation dimension for microseismic events in a Canadian hard-rock mine. In retrospect, this is not surprising since the b-value indicates the distribution of event sizes, whereas the spatial correlation dimension indicates the distribution of interevent distances. Hypothetical relations of b-values and spatial fractal dimension usually begin with power laws relating numbers of faults to fault *lengths* (*28-29*). If the lengths are distributed according to a power law, the exponent is sometimes taken as the fractal dimension. Only if the spacing between event locations can be related to the distribution of active fault lengths will there be any connection between b-value and the correlation dimension (*29*). We do not know the distribution of active fracture lengths for the stopes studied here, so cannot test proposed associations.

Trifu and others (*27*) also found that the progenitor perturbs the volume in which aftershocks occur to such an extent that the b-value actually *decreases* for a time following the progenitor. Based on laboratory experiments (e.g., *30*), decreases in b-value are thought to coincide with increasing differential stress. Many of the sequences near stope 189 showed a higher b-value in the 2-h window than in the 16-h window, even after the estimated uncertainty is considered. Such observations are difficult to reconcile with other observations and theories that indicate that decreasing b-values before, and *increasing* b-values after, main shocks are associated with relaxation in stress state and concurrent event clustering (*29, 31*). Evidently, in the mine environment, a progenitor can lower the differential stress in the nearby, surrounding region. A recovery to higher differential stress might then occur during the aftershock period.

Finally, it should be recognized that some of the damage around a developing stope is aseismic in nature. What is called "aseismic" damage obviously depends on detection threshold capability. Boler and Swanson (*32*) showed that over several months, displacements in stope 99 were very heterogeneous, and that *coseismic* displacements may have accounted for as little as 30% of the measured time-dependent closure. Without additional data, however, it would be imprudent to speculate on differences in aseismic deformation at different times or in different stopes. Nevertheless, we have assumed throughout both parts of this report that the seismicity is a generally valid indicator of rock mass damage in unmined volumes adjacent to the stopes.

CONCLUSIONS

Conclusions concerning stope-scale microseismicity in this mine, from the various measures and analyses presented and discussed above, are given below:

1. Sequences of microseismic events following blasts or rock bursts were clustered in space and time. However, the degree of spatial clustering was somewhat greater than the degree of temporal clustering when comparison is made to random locations or random occurrences in the spatio temporal window of observation. The degree of clustering is inversely quantified by the fractal dimension.

2. Spatial and temporal clustering of stope-scale aftershock sequence events was well established within 2 h after the occurrence of the sequence progenitor (blast or bump) and changed little thereafter. Events continued to locate in much the same area and with the same clustering intensity as prior groups of events. Although event rates decreased and event numbers increased throughout the aftershock sequence, the sequences remained temporally and spatially fractal for at least 16 h following the progenitor. These observations argue for some mechanical dependency of younger events in a sequence on their predecessors.

3. There was no statistically significant difference in the degree of spatial clustering or in the degree of temporal clustering following production blasts or rock bursts and bumps. Therefore, the spatial or temporal fractal dimensions *cannot* reliably be used to infer the progenitor type. Nor can they be used to infer whether a blast induced one or more bumps shortly thereafter. Rather, the general similarity in both the spatial and temporal fractal dimensions following any progenitor type indicates the similar scale-invariant response of the affected rock volume to a rapid stress perturbation from any source.

4. Few of the other spatial or temporal attributes measured in this study can reliably be used to infer progenitor type. Instead, it appears that size attributes, such as numbers of event triggers or average energies of aftershock events, are somewhat more reliable indicators. Taken together with the previous conclusion, one can infer that the magnitude of the stress perturbation produced by

rock burst or blast, and not the subsequent interactions of forces and local structure, best distinguishes one aftershock sequence from another.

5. The unmined regions surrounding the two different stopes *cannot* be differentiated solely by the degree of spatial or temporal clustering of aftershock events occurring therein. If such clustering is relatable to heterogeneities in rock mass properties, such as preexisting fracture densities or strength, then the unmined regions were either similarly damaged or features such as joints and faults were grossly similar in strengths (as reflected in their seismic activity), independent of any geometric differences between the stopes.

6. When other attributes such as aftershock occurrence rate decay, interevent distance distributions, and aftershock energies are used, distinctions between the two stopes can be made in regard to their responses to stress perturbations. These attribute differences may have been a direct consequence of either the slightly different geometry of the stopes (because that affects the local stress concentrations) or the differences in the local rock mass damage state. There is presently no satisfactory way to distinguish the two possibilities with the available data.

7. Microseismic events following blasts can result from delayed slip on new fractures associated with that blast, as well as on fractures created by any previous mining activity. As a stope is developed and the residual pillar shrinks, increasing stresses and damage accumulation modify the rate of aftershock event occurrences as well as the local density. Nevertheless, spatial and temporal scale invariance are maintained; no long-term trends were perceived.

8. In any aftershock sequence following a rock burst or blast-induced bump, a significant fraction of the event locations were associated with northeast-trending planes that roughly aligned with the position and attitude of the local stope and vein, and *not* with most of the mapped *northwest*-trending fractures and faults. The remainder of the event locations were contained in nonplanar clusters or volumetrically dispersed. This argues for a distributed damage model, in contrast to a single fault-slip model in which aftershocks would primarily occur on the same fault as the sequence progenitor.

ACKNOWLEDGMENTS

The authors thank ASARCO, Inc., for its long-standing cooperation with the USBM in the field experiments at the Galena Mine, Wallace, ID. Data collection and field assistance by C. D. Sines, USBM engineering technician, over many years have resulted in the vast amount of raw data from that mine available for study. P. Swanson, USBM geophysicist, J. Whyatt, USBM mining engineer, and C. Bufe, geophysicist of the U.S. Geological Survey, made several useful comments on an earlier version of this report.

REFERENCES

1. Kranz, R. L., J. P. Coughlin, and S. Billington. Studies of Stope-Scale Seismicity in a Hard-Rock Mine. Part 1: Methods and Factors. USBM RI 9525, 1994, 27 pp.

2. Utsu, T. Aftershocks and Earthquake Statistics (1). J. Fac. Sci., Hokkaido Univ., Ser. 7, v. 3, 1969, pp. 129-195.

3. Gardner, J. K., and L. Knopoff. Is the Sequence of Earthquakes in Southern California, With Aftershocks Removed, Poissonian? Bull. Seismol. Soc. Am., v. 64, 1974, pp. 1363-1367.

4. Shlien, S., and M. N. Toksoz. A Statistical Method of Identifying Dependent Events and Earthquake Aftershocks. Earthquake Notes, v. 45, No. 3, 1974, pp. 3-16.

5. Frohlich, C., and S. D. Davis. Identification of Aftershocks of Deep Earthquakes by a New Ratio Method. Geophys. Res. Lett., v. 12, 1985, pp. 713-716.

6. Reasenberg, P. Second-Order Moment of Central California Seismicity, 1969-1982. J. Geophys. Res., v. 90, 1985, pp. 5479-5495.

7. Davis, S. D., and C. Frohlich. Single-Link Cluster Analysis, Synthetic Earthquake Catalogues, and Aftershock Identification. Geophys. J. Int., v. 104, 1991, pp. 289-306.

8. Molchan, G. M., and O. E. Dmitrieva. Aftershock Identification: Methods and New Approaches. Geophys. J. Int., v. 109, 1992, pp. 501-516.

9. Swanson, P. L. Mining-Induced Seismicity in Faulted Geologic Structures: An Analysis of Seismicity-Induced Slip Potential. Pure Appl. Geophys., v. 139, 1992, pp. 657-676.

10. Boler, F. M., and P. L. Swanson. Seismicity and Stress Changes Subsequent to Destress Blasting at the Galena Mine and Implications for Stress Control Strategies. USBM RI 9448, 1993, 21 pp.

11. Fehler, M., L. House, and H. Kaieda. Determining Planes Along Which Microearthquakes Occur: Application to Earthquakes Accompanying Hydraulic Fracturing. J. Geophys. Res., v. 92, 1987, pp. 9407-9414.

12. Fehler, M., and P. Johnson. Determination of Fault Planes at Coalinga, California By Analysis of Patterns in Aftershock Locations. J. Geophys. Res., v. 94, 1989, pp. 7496-7506.

13. Hirata, T. Omori's Power Law Aftershock Sequences of Microfracturing in Rock Fracture Experiment. J. Geophys. Res., v. 92, 1987, pp. 6215-6221.

14. Davis, S. D., and C. Frohlich. Single-Link Cluster Analysis of Earthquake Aftershocks: Decay Laws and Regional Variations. J. Geophys. Res., v. 96, 1991, pp. 6335-6350.

15. Beyer, W. H. (ed.). Handbook of Tables for Probability and Statistics. Chem. Rubber Co., 2nd ed., 1968, pp. 427-429.

16. Gresseth, E. W., and R. R. Reid. A Petrofabric Study of Tectonic and Mining-Induced Deformations in a Deep Mine. USBM RI 7173, 1968, 64 pp.

17. Scott, D. F. Relationship of Geologic Features to Seismic Events, Lucky Friday Mine, Mullan, Idaho. Paper in Rockbursts and Seismicity in Mines (Proc. 3rd Int. Symp. on Rockbursts and Seismicity, Kingston,

Ontario, Canada, Aug. 1993), ed. by R. P. Young. Balkema, 1993, pp. 401-405.

18. Legge, N. B., and S. M. Spottiswoode. Fracturing and Microseismicity Ahead of a Deep Gold Mine Stope in the Pre-Remnant and Remnant Stages of Mining. Paper in Proceedings of 6th International Congress on Rock Mechanics, Montreal, Canada, ed. by G. Herget and S. Vongpaisal. Balkema, 1987, pp. 1071-1077.

19. McGarr, A., S. M. Spottiswoode, N. C. Gay, and W. D. Ortlepp. Observations Relevant to Seismic Driving Stress, Stress Drop and Efficiency. J. Geophys. Res., v. 84, 1979, pp. 2251-2261.

20. Urbancic, T. I., C-I. Trifu, and R. P. Young. Microseismicity Derived Fault-Planes and Their Relationship to Focal Mechanism, Stress Inversion, and Geologic Data. Geophys. Res. Lett., v. 20, 1993, pp. 2475-2478.

21. Spathis, A. T., D. P. Blair, and J. R. Grant. Seismic Pulse Assessment of the Changing Rock Mass Conditions Induced by Mining. Int. J. Rock Mech. Min. Sci., v. 22, 1985, pp. 303-312.

22. Young, R. P., and J. J. Hill. Seismic Characterization of Rock Masses Before and After Blasting. Paper in Proceedings of 26th U.S. Symposium on Rock Mechanics, Rapid City, SD, ed. by E. Ashworth. Balkema, 1985, pp. 1151-1158.

23. Talebi, S., and R. P. Young. Microseismic Monitoring in Highly Stressed Granite: Relation Between Shaft-Wall Cracking and In-Situ Stress. Int. J. Rock Mech. Min. Sci., v. 29, 1992, pp. 25-34.

24. Eneva, M., and R. P. Young. Evaluation of Spatial Patterns in the Distribution of Seismic Activity in Mines: A Case Study of Creighton Mine, Northern Ontario (Canada). Paper in Rockbursts and Seismicity in Mines (Proc. 3rd Int. Symp. on Rockbursts and Seismicity, Kingston, Ontario, Canada, Aug. 1993), ed. by R. P. Young. Balkema, 1993, pp. 175-180.

25. Kranz, R. L. Fractal Point Patterns and Fractal Fracture Traces. Paper in Rock Mechanics: Models and Measurements Challenges From Industry (Proc. 1st N. Amer. Rock Mech. Symp., Austin, TX, June 1-3, 1994), ed. by P. Nelson and S. Laubach. Balkema, 1994, pp. 793-800.

26. Shaw, B. E. Generalized Omori Law for Aftershocks and Foreshocks From a Simple Dynamics. Geophys. Res. Lett., v. 20, 1993, pp. 907-910.

27. Trifu, C-I., T. I. Urbancic, and R. P. Young. Non-Similar Frequency Magnitude Distribution for M < 1 Seismicity. Geophys. Res. Lett., v. 20, 1993, pp. 427-430.

28. King, G. The Accommodation of Large Strains in the Upper Lithosphere of the Earth and Other Solids by Self-Similar Fault Systems: The Geometrical Origin of b Value. Pure Appl. Geophys., v. 121, 1983, pp. 761-815.

29. Main, I. G. Damage Mechanics With Long-Range Interactions: Correlation Between the Seismic b-Value and the Fractal Two-Point Correlation Dimension. Geophys. J. Int., v. 111, 1992, pp. 531-541.

30. Scholz, C. H. The Frequency Magnitude Relation of Microfracturing in Rock and Its Relation to Earthquakes. Bull. Seismol. Soc. Am., v. 58, 1968, pp. 1117-1130.

31. Hirata, T. A. Correlation Between the b-Value and the Fractal Dimension of Earthquakes. J. Geophys. Res., v. 94, 1989, pp. 7507-7514.

32. Boler, F. M., and P. L. Swanson. Observations of Heterogeneous Stope Convergence Behavior and Implications for Induced Seismicity. Pure Appl. Geophys., v. 139, 1992, pp. 639-656.

33. Willemann, R. J. Cluster Analysis of Seismic Moment Tensor Orientations. Geophys. J. Int., v. 115, 1993, pp. 617-634.

34. McWilliams, P. C., M. W. McDonald, and F. M. Jenkins. Statistical Analysis of a Microseismic Field Data Set. Paper in Rockbursts and Seismicity in Mines. Proceedings of the 2nd International Symposium on Rockbursts and Seismicity in Mines (Univ. MN, Minneapolis, MN, June 8-10, 1988), ed. by C. Fairhurst. Balkema, 1990, pp. 235-245.

35. Frohlich, C., and S. D. Davis. Single-Link Cluster Analysis as a Method to Evaluate Spatial and Temporal Properties of Earthquake Catalogues. Geophys. J. Int., v. 100, 1990, pp. 19-32.

36. Jardine, N., and R. Sibson. Mathematical Taxonomy. Wiley, New York, 1971, 286 pp.

37. Anderberg, M. R. Cluster Analysis for Applications. Academic, New York, 1973, 359 pp.

38. Kaufman, L., and P. J. Rousseeuw. Finding Groups in Data. Wiley, New York, 1990, 342 pp.

APPENDIX A.—MATHEMATICAL TAXONOMY

Any individual or group of individuals can be described by a set of characteristics or attributes. One can never know the set completely. However, it may be possible to describe and quantify enough attributes, or a subset of particularly characteristic attributes, to enable us to separate a heterogeneous collection of individuals into homogeneous classes. Such classification may give us new insights about the individuals or groups of individuals. It may also give us information about the relative importance or dominance of various attributes. This approach has been used extensively for many years in the biological and social sciences, but only recently has it been applied seismologically (*7, 14, 31, 33-35*). As in the papers just referenced, we are interested here in hierarchical cluster analysis procedures. General references on this topic (*36-38*) show that the generic procedures for population classification require several sequential steps.

The first step is to collect measures of attributes. Typically, this collection is organized in a matrix, with each row representing an individual's set of attributes and each column the measures of a single attribute. The whole collection may be thought of as a set of vectors in multidimensional attribute space. Although attributes can be nonnumerical, we are interested here only in attributes that have measured numerical values. Attribute values can vary widely in absolute magnitude according to the scale units chosen. Furthermore, units of measure cannot always be converted to a common system. Accordingly, weighting and normalization techniques are often used to minimize bias resulting from disparate units and scales. Such techniques must be used cautiously since they may artificially affect the ultimate groupings and classifications, as well as destroy important information on attribute relative strengths. If the attribute matrix is incomplete, missing attribute measures can be calculated from the expected values of the attributes. Expectation values are typically based on assumptions of randomness or specific attribute frequency distributions (known or hypothesized). Any artificial values introduced in this manner must not alter the cluster relationships.

The second step is to define and quantify the similarity or dissimilarity among the individuals in a consistent fashion. The mathematical expression chosen to quantify similarity also has an effect on the final classification outcome. Many different expressions have been used to construct a similarity or dissimilarity matrix. For example, the dissimilarity D_{ij} between individuals is commonly calculated using the general Minkowski distance:

$$D_{ij} = \left[\sum_{K=1}^{N} (A_{ik} - A_{jk})^P \right]^{\frac{1}{P}}, \qquad \text{(A-1)}$$

where A_{ik} are the k attributes of the ith individual. The constant P may be assigned any positive value. If P = 2, this is the familiar "Euclidean distance" measure. Larger P values tend to emphasize the larger or more conspicuous differences among attributes. Another way to quantify dissimilarity is to use the direction cosines between the row vectors. Normalization techniques have the least effect on this measure since they affect the vector lengths only. Still another way to quantify similarity is to calculate the correlation coefficients among the attributes in all rows.

Once the matrix of dissimilarity or similarity values is constructed, the third step is to choose a linkage or grouping method. In hierarchical methods, a choice must be made as to the order in which grouping decisions are to be effected: divisive (starting with all individuals) or agglomerative (taking one individual at a time in sequence). Like the decision of how to define similarity, the choice of method to link individuals or separate groups strongly affects the final outcome. Some common methods are:

1. Maximize the smallest distance between a member of class A and a member of class B (figure A-1). This is called the nearest neighbor or single-link method.
2. Maximize the largest distance between a member of class A and a member of class B (figure A-2). This is called the furthest neighbor or complete-link method.
3. Minimize the within-group dissimilarity average or maximize the within-group similarity (figure A-3). This is sometimes called the within-group method.
4. Maximize the dissimilarity between the attributes of all members of class A and the *corresponding* attributes of all members of class B (figure A-4). This is called the between-group method.
5. Maximize the separation between the mean attribute values of class A and the corresponding mean attribute values of class B (figure A-5). This is called the centroid method.

Results can be displayed in portions or slices of attribute space, as in the schematic figures A-1 through A-5, or in hierarchical connections called "dendograms." Examples of dendograms for aftershock classes are given in the main body of the text as figures 19 and 20. If an individual or group of individuals has a large number of attributes, it is not trivial to find the crossplots of the two or three attributes that visually show the greatest separation in attribute space. On the other hand, hierarchical dendograms give information on both the class membership and degree or scale of class separation.

For an objective measure of the effectiveness of the clustering process, one can quantify the separability of the classes with the Wilks' parameter L = W/(B + W). W is the within-group scatter, equal to the deviation between attribute elements and the corresponding mean value of

each attribute for the members of the group. B is the between-group scatter, equal to the total difference between the global mean attribute values of each group. Smaller L values indicate better clustering results. In choosing from a variety of possible dissimilarity measures and clustering methods, one strategy could be to minimize W and maximize B in an iterative fashion until L is at minimum. However, small differences in L values resulting from different combinations of attributes, dissimilarity measures, or clustering methods need to be evaluated on a case-by-case basis. A low value of Wilks' L may simply be an artifact of having one or more classes containing a single outlier member (such as in the dendogram example of figure 19).

APPENDIX B.—EXAMPLE OF CLASSIFICATION OF SEQUENTIAL EVENTS

As a detailed example of the methodology and to demonstrate its capabilities, we examined a single sequence composed of 563 individual microseismic events near one stope occurring before and after a large event (event 237 in the sequence). The epicenters of the set of events classified were shown previously in figure 23*A* in the report on the first part of this study (*1*). That figure is repeated here as figure B-1. One objective for such a study could be to indicate any differences, indicated by assignment to different classes, between events prior to and after the large event. Since waveform data were not available, only four attributes of the 563 individual events were used, namely, calculated x,y,z location coordinates and the number of geophones in the network that exceeded a preset amplitude threshold. This last attribute is only a rough measure of event size, for it depends in a complicated way on the location of the event with respect to the locations of geophones within the network. Using only these four attributes, however, it is relatively easy to confirm any class differences visually on a map of event locations. A similar analysis on seismicity data from another hard-rock mine, using only location attributes, the Euclidean distance metric, and a centroid method of group separation, was performed by McWilliams and others (*34*). They related the results of the class membership's average position to mine and geologic structure. Frohlich and Davis used the Euclidean distance metric and the single- link grouping method as a tool to study spatial associations of earthquakes and to identify aftershocks (*7, 14, 35*).

Five different measures of dissimilarity (three different values of P in equation A-1, direction cosines, and correlation coefficients) were used with the five different methods of group separation described in appendix A. Therefore, 25 combinations of methodological parameters were evaluated. A FORTRAN program was written, making use of subroutines in the IMSL[1] statistical analysis library, to accomplish this. Evaluation of each cluster analysis was made using both the value of Wilks' parameter and close examination of the derived class memberships. Results indicated that the choice of dissimilarity measure was not as important as the choice of grouping method in this case example. The best combination of methods used the maximum distance metric (letting P in equation A-1 approach infinity) to quantify dissimilarity and the maximized between-group separation clustering method (figure A-4). The classification results presented below were derived from this combination of methods. Because of the size of the population analyzed, the dendogram representation of the results would be quite long, and it is not presented here.

[1]Integrated mathematical software library.

The 563 events were separated into two, three, and four classes during independent trial analyses. Class membership population counts (NCLUS) and individual class assignments (ICLUS) are shown in figures B-2 through B-4 for two, three, and four classes, respectively. The ICLUS listings are sequential in time, starting with the leftmost member in a row and proceeding to the right, then down to the leftmost member in the next row, proceeding to the right, etc. The time between events is not uniform, however. The main event is event 237, which is indicated with a box in all three figures. In figures B-2 and B-3, it is a member of class 2, whereas in figure B-4 it is a member of class 4.

Let us first examine the two-class analyses in figure B-2. There are 75 members in class 1, and 488 members in class 2. Forty-one class 2 members occur first, then many class 1 members, then a string of class 2 members, then a string of class 1 members and finally another string of class 2 members. Just before the main event, a class 1 member occurred. Following the main event, almost all events are members of class 2. Examination of the attributes of the two classes shows that almost all class 1 members have an East coordinate less than 12950, while almost all class 2 members have an east coordinate greater than 12950. Looking at the epicenter map in figure B-1, it is not hard to see why the events were separated primarily by this coordinate, as there seems to be an epicenter cluster division on this axis. This classification probably could have been done by eye. The strong serial correlation between class occurrence times is just a reflection of the fact that a group of events occurred closely together in space and time, then activity switched to a different area, then back to the first area, etc. Following the main event, activity was confined primarily to the region near its location. These event locations were previously analyzed for planar structure in the first report (*1*). All of the events occurring on the plane depicted in figure 23*B* of reference 1 are class 2 events.

Now let us look at the three-class results in figure B-3. Here, class 3 contains the same 75 members as class 1 in the previous example above. However, the previous class 2 has been separated into two new classes of 98 and 390 members, respectively. This separation into class 1 and class 2 was done primarily by number of overthreshold geophones, with class 1 having a small number and class 2 having a moderate to large number of overthreshold geophone hits. Almost all the members of both class 1 and class 2 lie east of coordinate 12950. The same serial correlation previously observed in the two-class results is seen here. However, now we have the additional information that after the main event, more of the events were

relatively moderate to large in size, whereas smaller events to the east of coordinate 12950 occurred sporadically as time passes. The apparently random occurrence of class 3 members after the main event might allow us to discard them and identify only class 1 and 2 members as true "aftershocks." Most of the 113 plane-forming events shown in figure 23*B* of reference 1 were of class 1; the others were of class 2.

Now, the four-class results in figure B-4 are discussed. The main event is a member of class 4, which holds only 22 members. Class 3 is a singleton class. The serial correlation seen previously in the two-class and three-class results is still evident in figure B-4. Examination of the membership indicates that class 4 holds only the events with the largest number of overthreshold geophone hits, to the east of coordinate 12950. The single member of class 3 is both west of 12950 and far to the south of most other events. Class 2 and class 1 members tend to be located west and east of coordinate 12950, respectively. One can see that, although some large events (class 4) occurred before the main event, most occurred after and close in time to it, with only a few occurring at later times. One might further restrict the classification of "aftershock" to be only those members of class 4 that occurred after the main event. However, of the 22 members of class 4, only 5 were part of the plane-forming group shown in figure 23*B* of reference 1. All other plane-forming events were class 1 members.

In none of the analyses just presented was there any clear indication that some subset of seismic activity, prior to the main event, was different enough to allow classification as "foreshocks," or to be useful for predicting the main event. We would be quite surprised if there had been identifiable foreshocks, since the main event was not a result of naturally changing stresses, but rather a result of a production blast less than a minute before! However, a retrodictive search for "foreshocks" to a progenitor not associated with blasting might be pursued in this fashion. One may also use the analyses to help restrict or define the term "aftershock."

The results just presented show a certain utility for extracting information about a set of individuals that might not be easily obtained otherwise. Usually, the list of available attributes is larger than in the preceding simple example. Such is the case for the aftershock sequences that are the subject of this report, where each entire sequence is treated as an individual with many attributes (table 2).

Figure 1

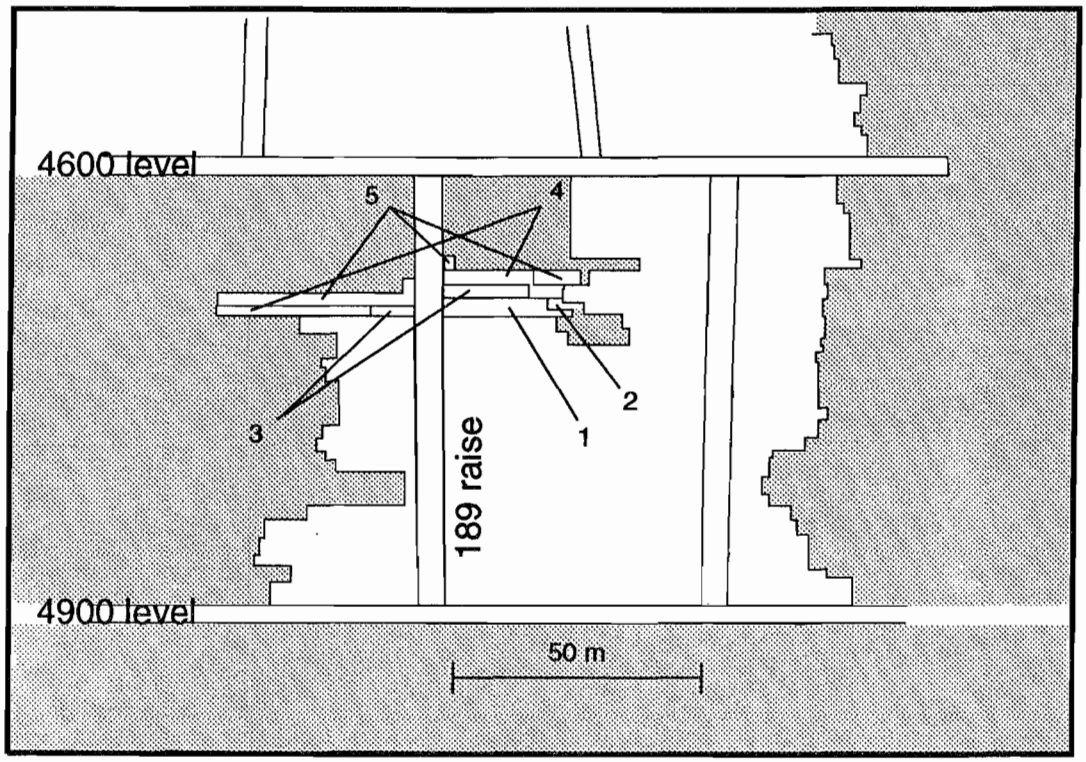

Cross section of stope 189 looking north, perpendicular to the silver vein in this area. Sections mined are shown on a quarterly basis.

Figure 2

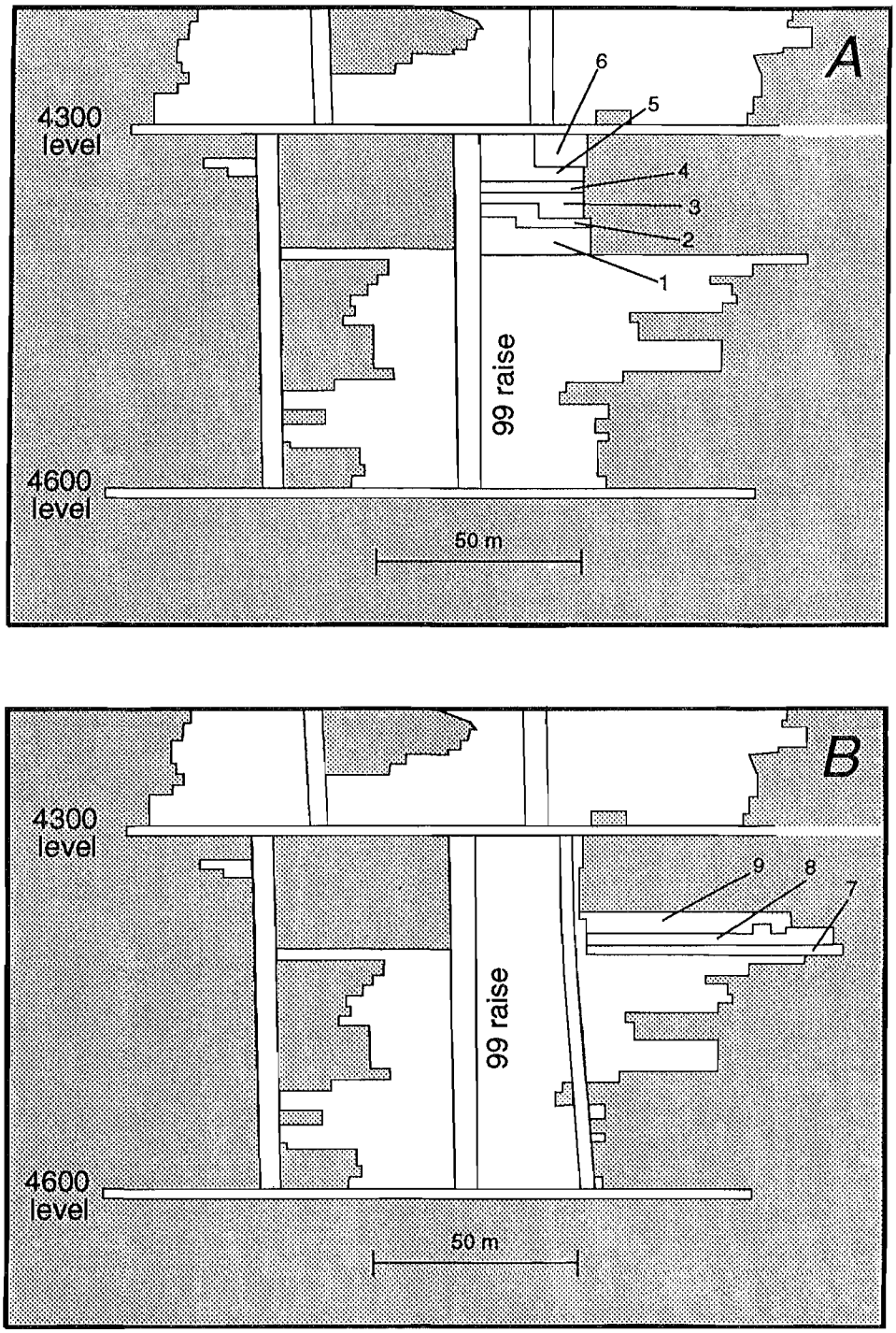

KEY

1	Oct-Dec 1989
2	Jan-Mar 1990
3	Apr-Jun 1990
4	Jul-Sep 1990
5	Oct-Dec 1990
6	Jan-Mar 1991
7	Apr-Jun 1991
8	Jul-Sep 1991
9	Oct-Dec 1991

Cross section of stope 99 looking N. 48° W., perpendicular to the mined vein in this area. Sections mined are shown on a quarterly basis for (A) periods prior to April 1991 and (B) subsequent periods.

Figure 3

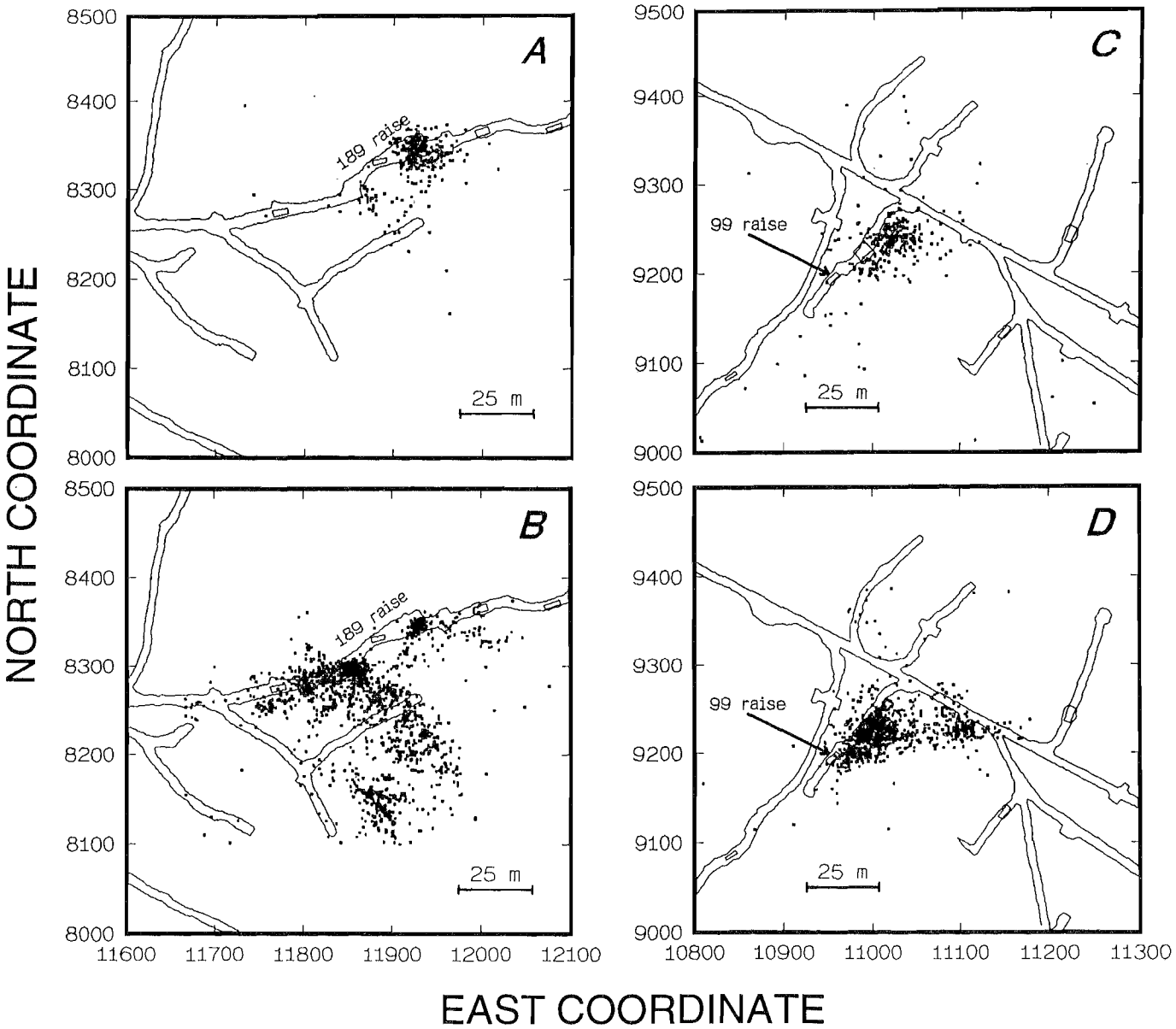

Aftershock event locations for selected sequences occurring near stopes 189 and 99. Map views, looking down. A, Sequence 891211.141941, following a production blast on east side of stope 189; B, sequence 900307.141821, in which a large rock burst and smaller bumps followed a production blast on west side of stope 189; C, sequence 900406.141949, following a production blast in stope 99; D, sequence 900615.145016, in which a moderate bump followed a destressing blast in stope 99. Mine coordinates, in feet, are shown.

Figure 4

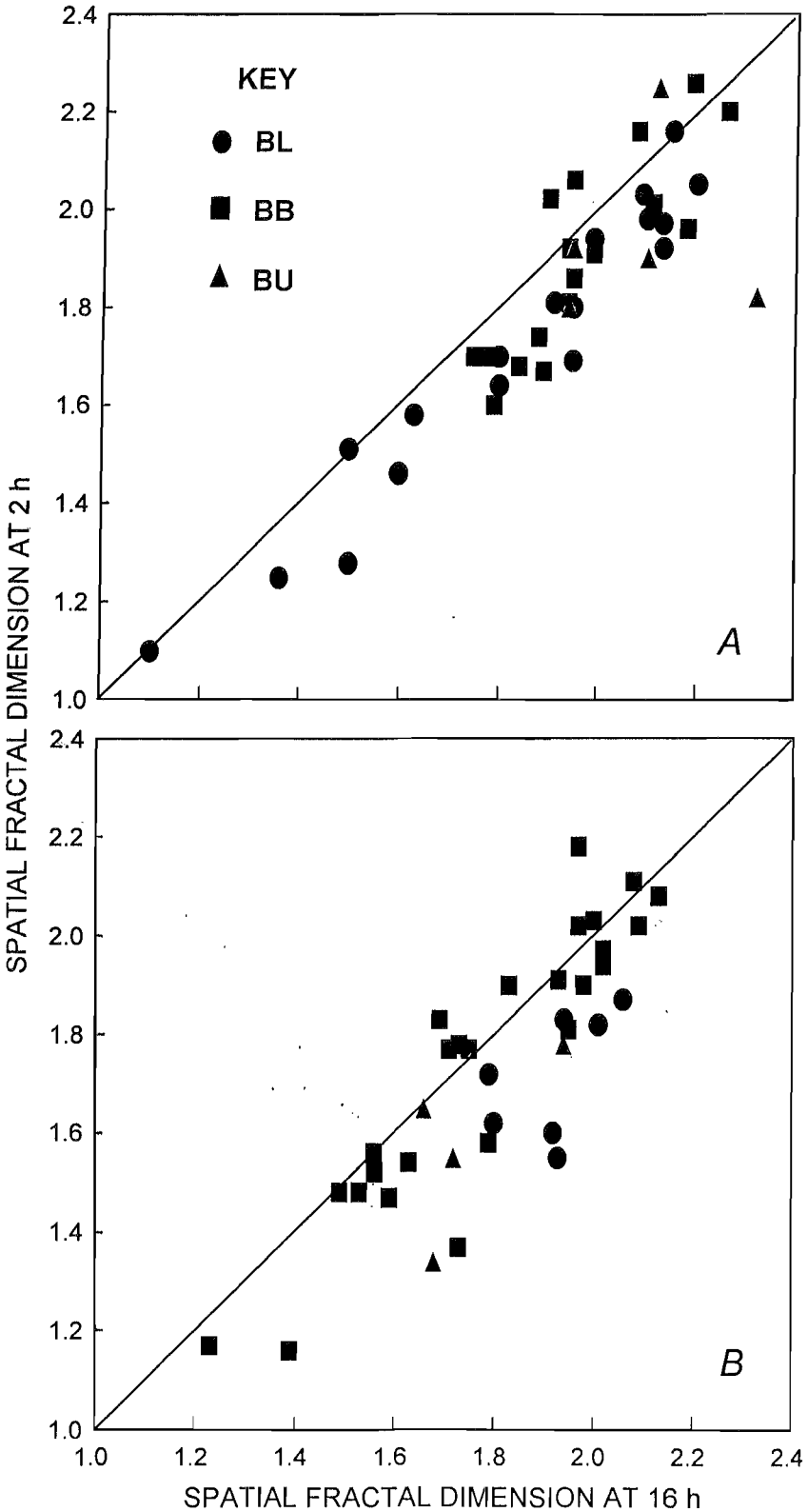

Spatial fractal dimension (SF) determined 2 and 16 h after progenitor occurrence near (A) stope 189 and (B) stope 99.

Figure 5

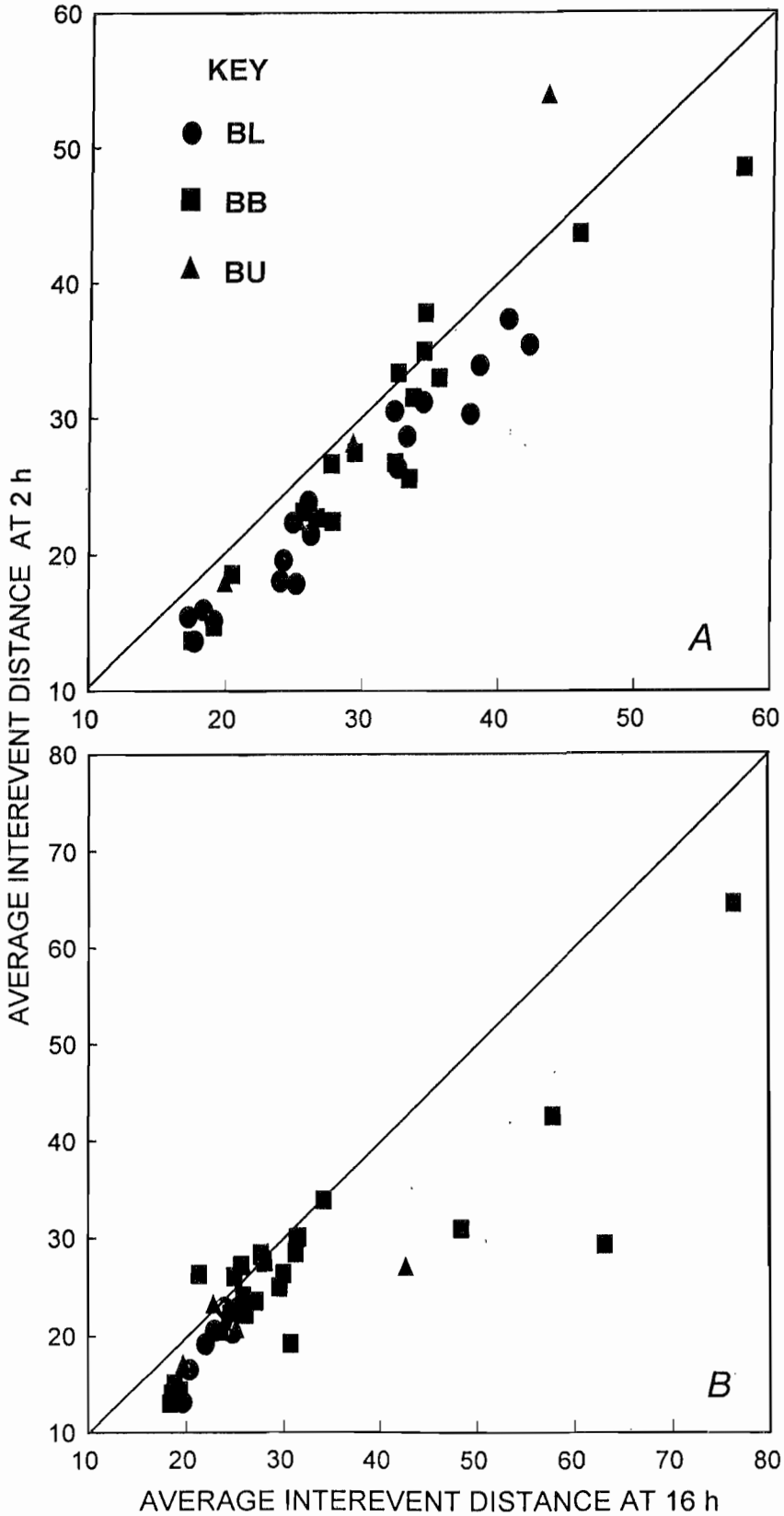

Average interevent distance (AD) determined 2 and 16 h after progenitor occurrence near (A) stope 189 and (B) stope 99. Distance is in meters.

Figure 6

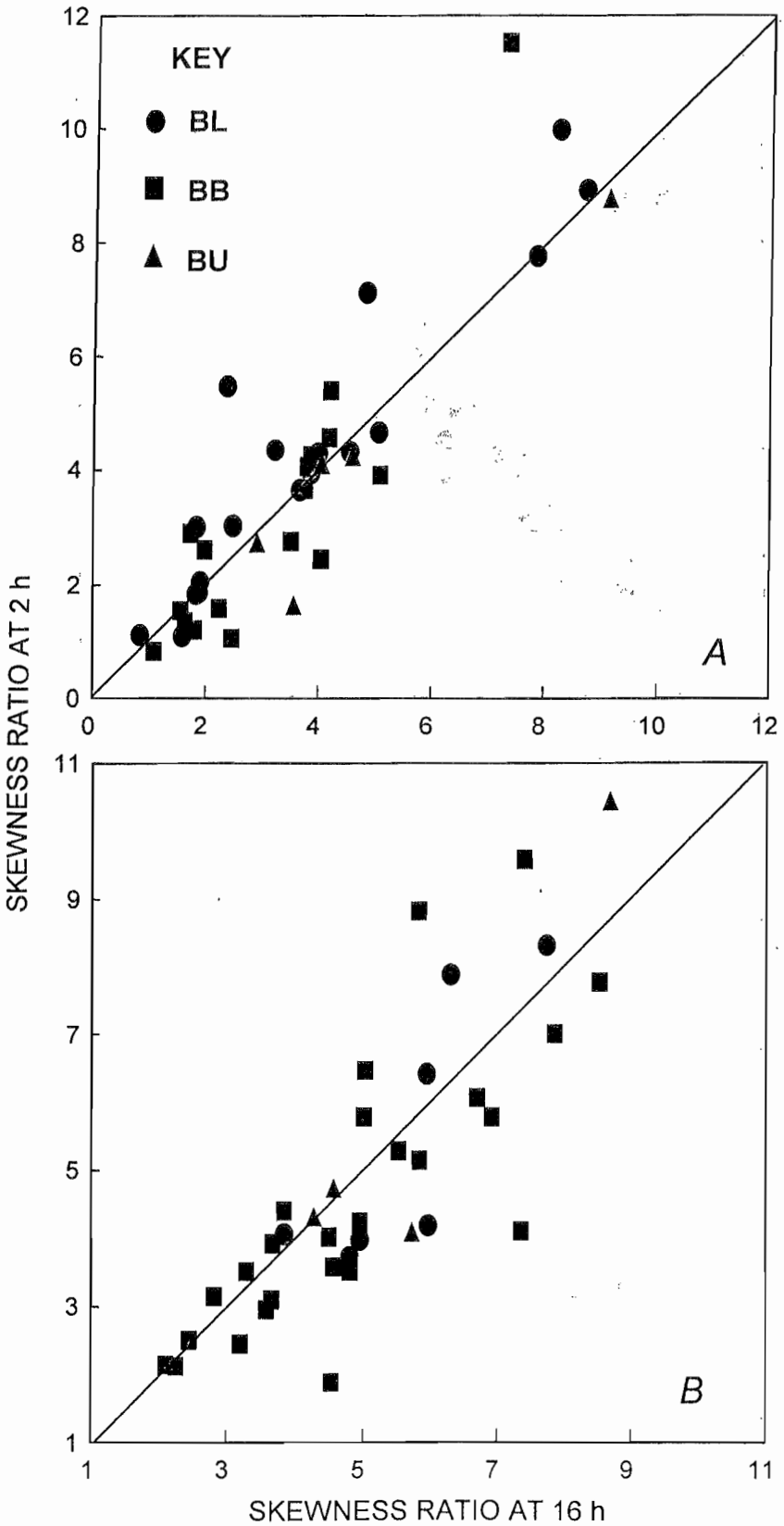

Skewness ratio (SR) determined 2 and 16 h after progenitor occurrence near (A) stope 189 and (B) stope 99.

Figure 7

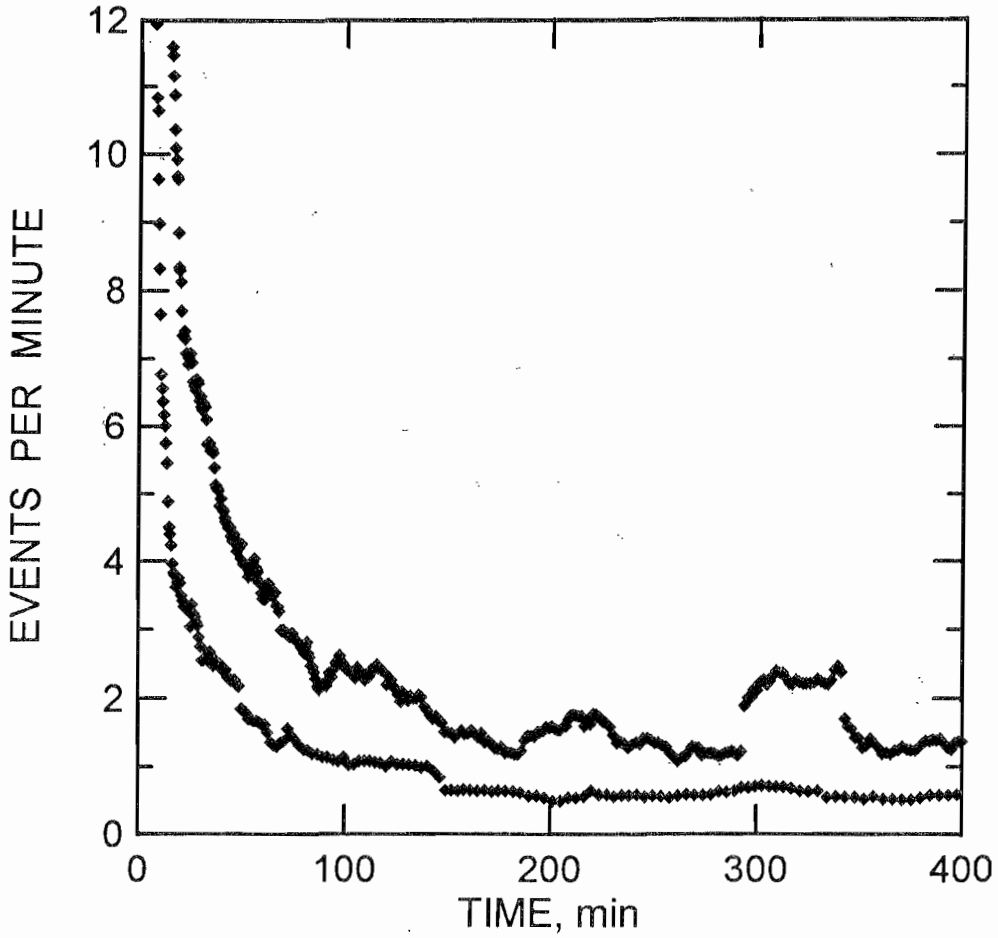

Event rate as a function of time for two sequences.

Figure 8

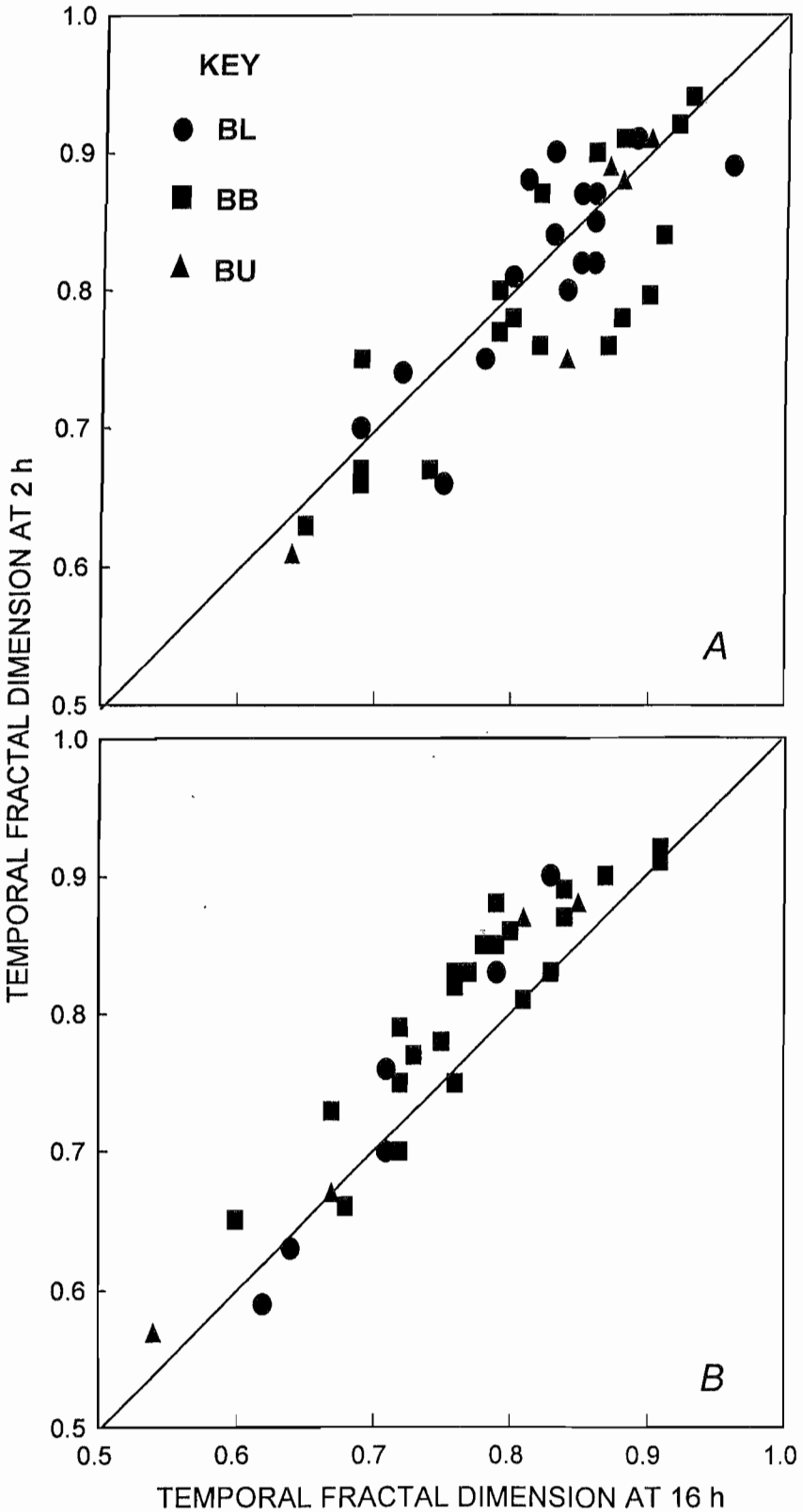

Temporal fractal dimension (TF) determined 2 and 16 h after progenitor occurrence near (A) stope 189 and (B) stope 99.

Figure 9

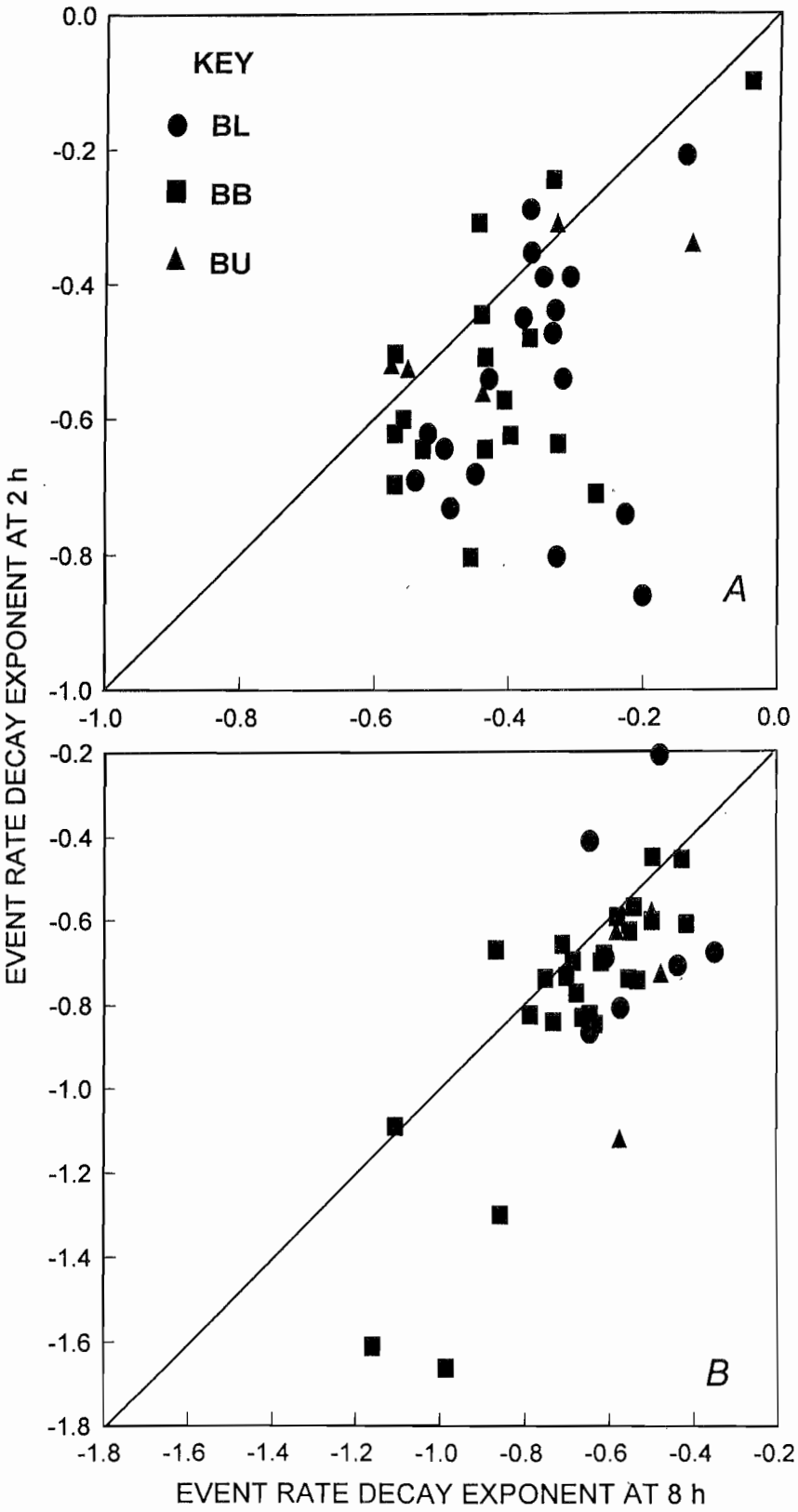

Exponent of decaying power law fit to event rate (DR) determined 2 and 8 h after progenitor occurrence near (A) stope 189 and (B) stope 99.

Figure 10

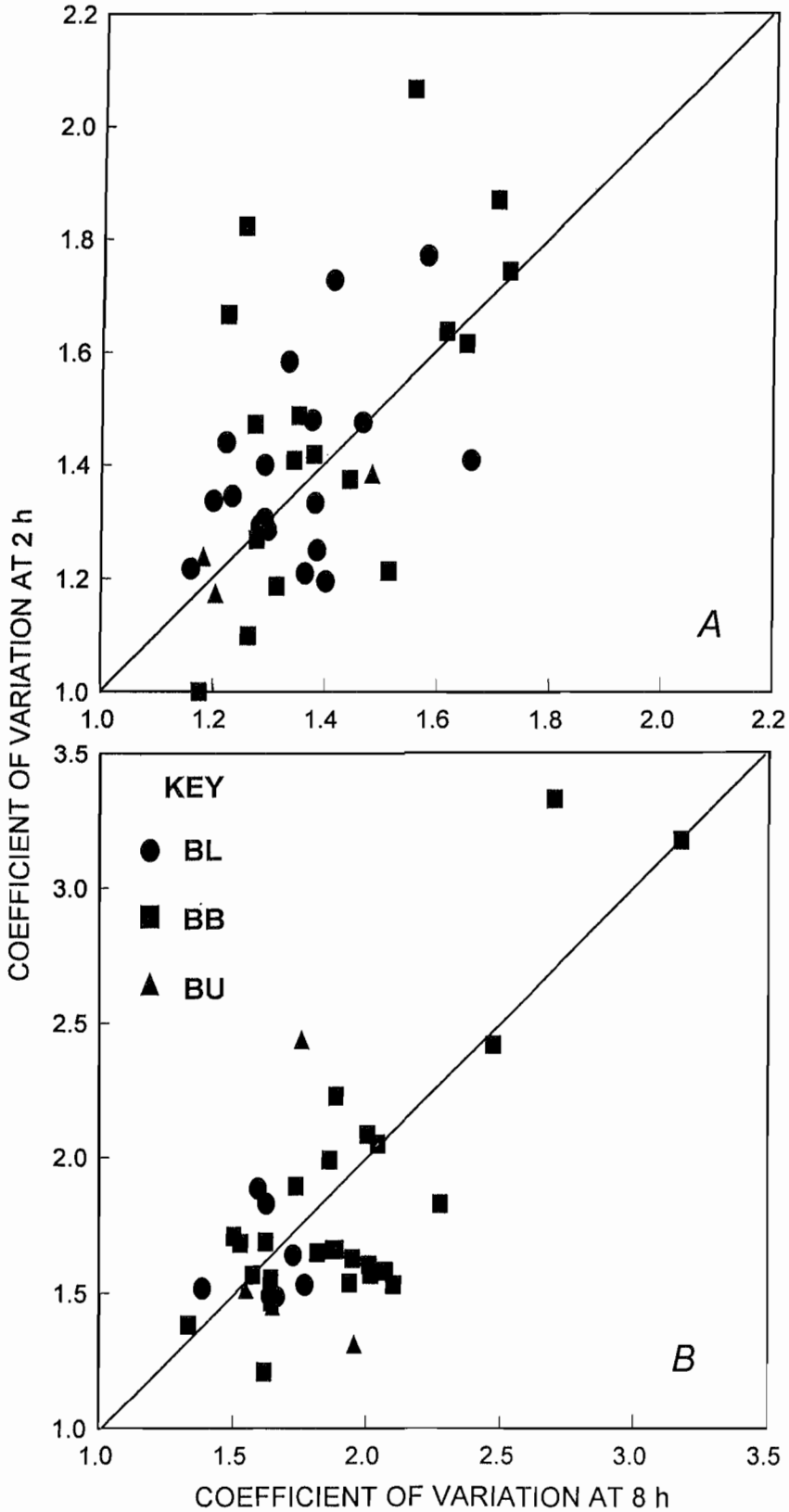

Coefficient of variation (CV) determined 2 and 8 h after progenitor occurrence near (A) stope 189 and (B) stope 99.

Figure 11

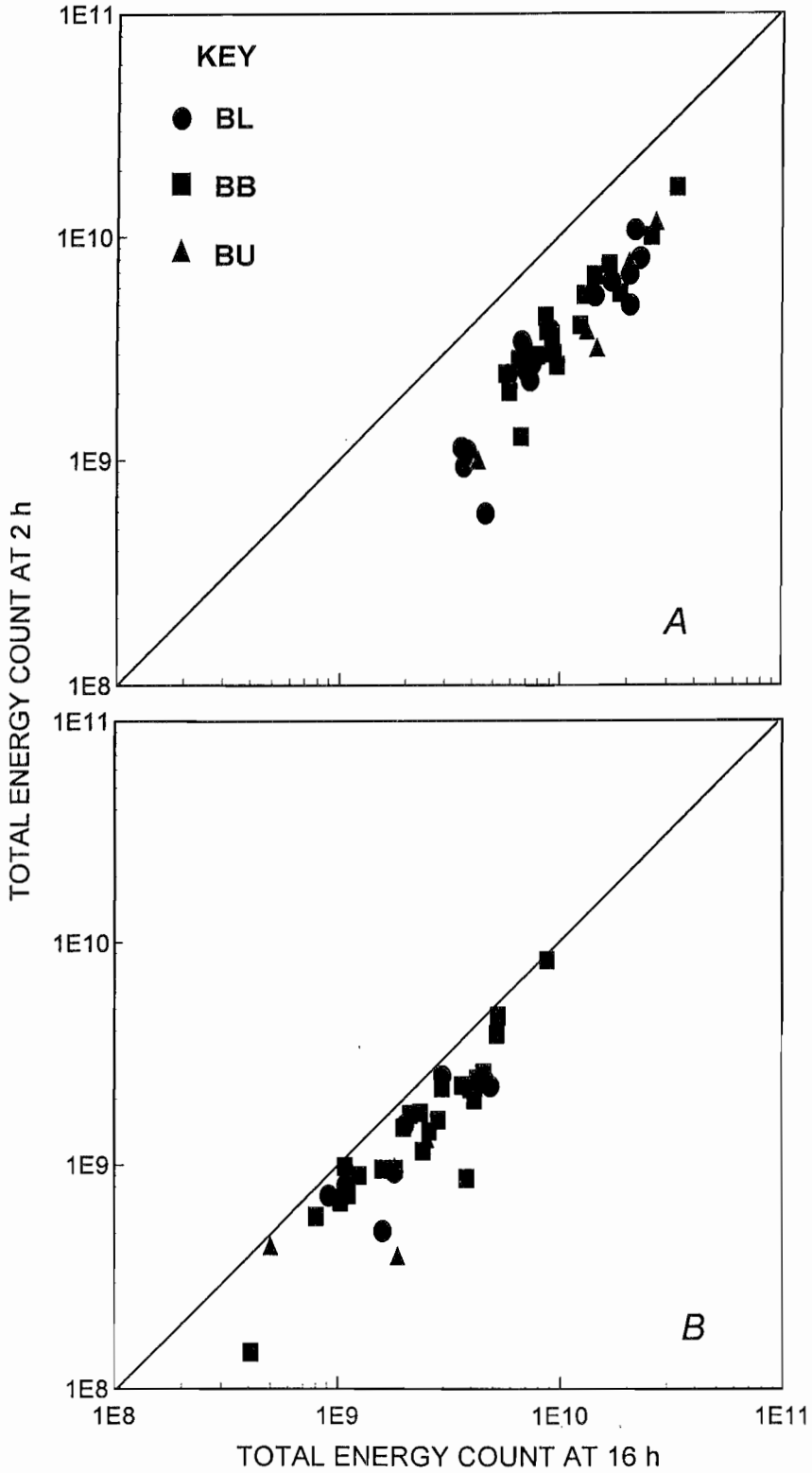

Cumulative normalized energy (ET) for aftershock sequence events, determined 2 and 16 h after progenitor occurrence near (A) stope 189 and (B) stope 99.

Figure 12

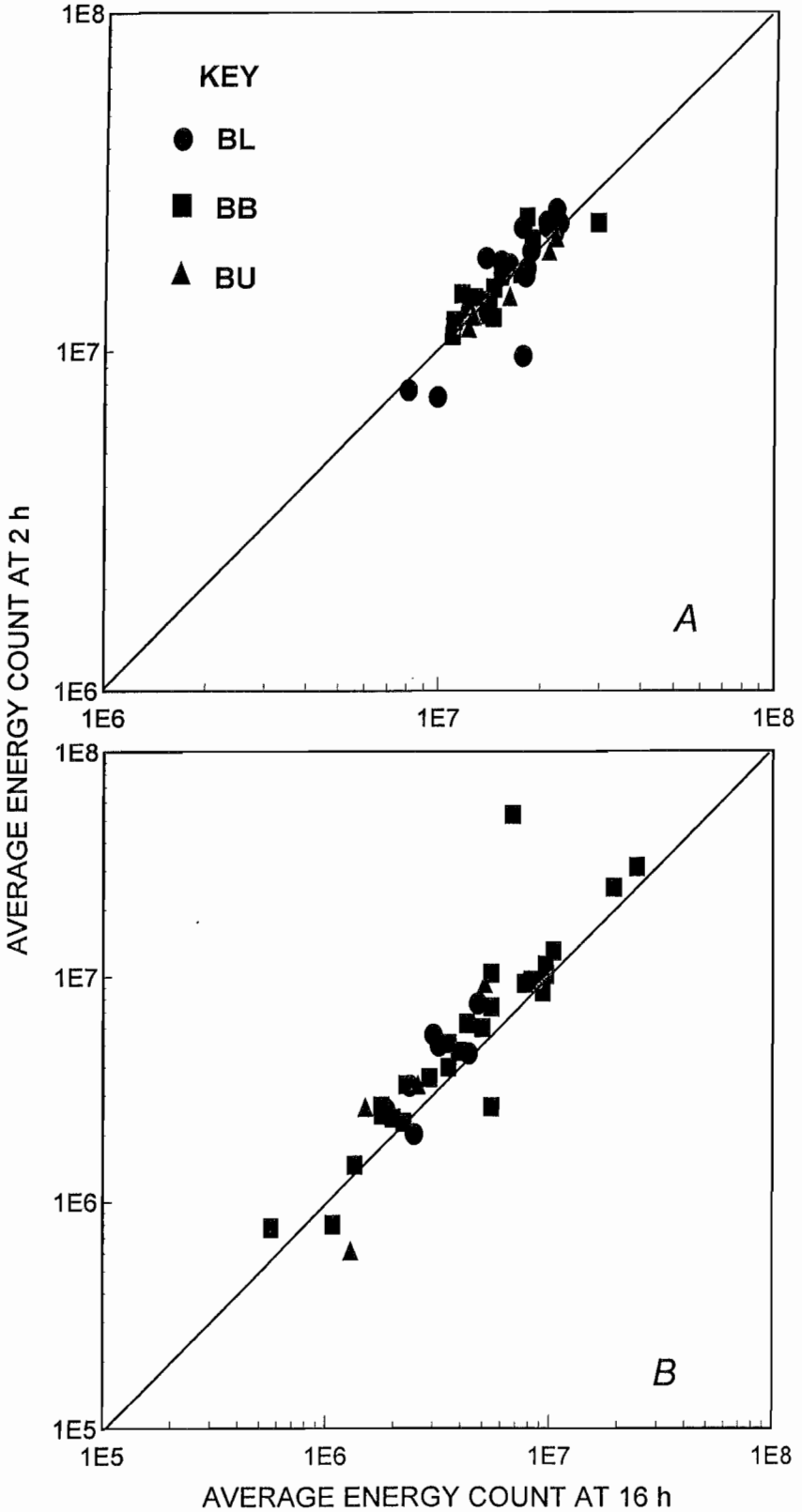

Average aftershock event energy (EA) determined 2 and 16 h after progenitor occurrence near (A) stope 189 and (B) stope 99.

Figure 13

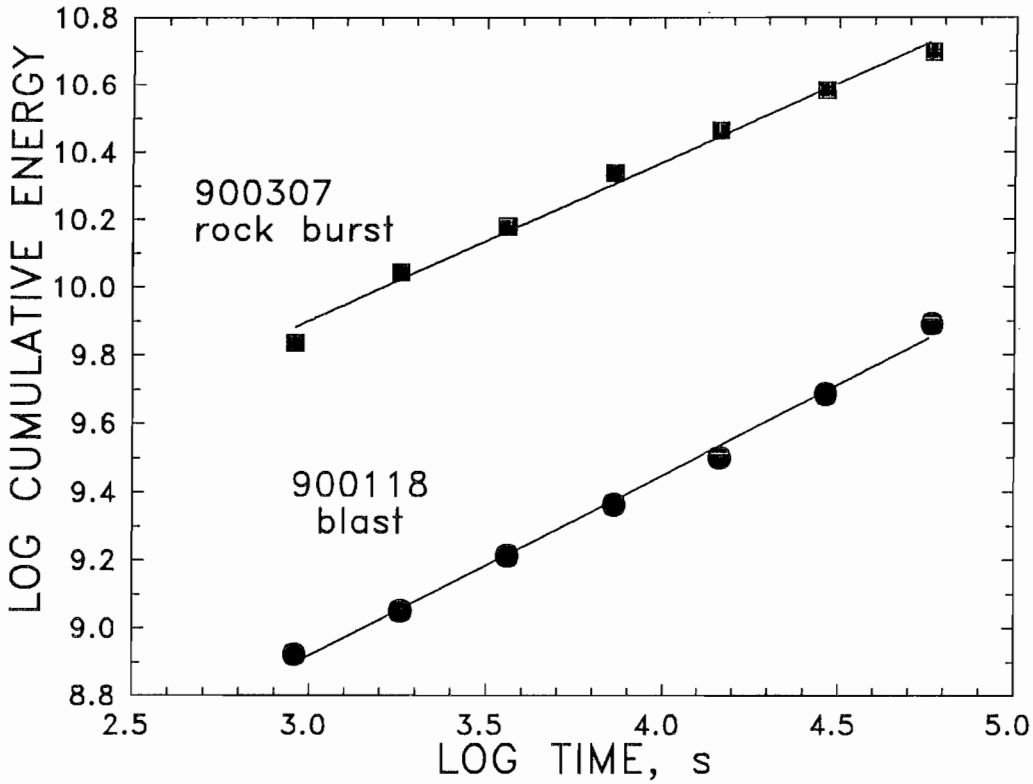

Cumulative event energy (ET) as a function of time for two sequences near stope 189.

Figure 14

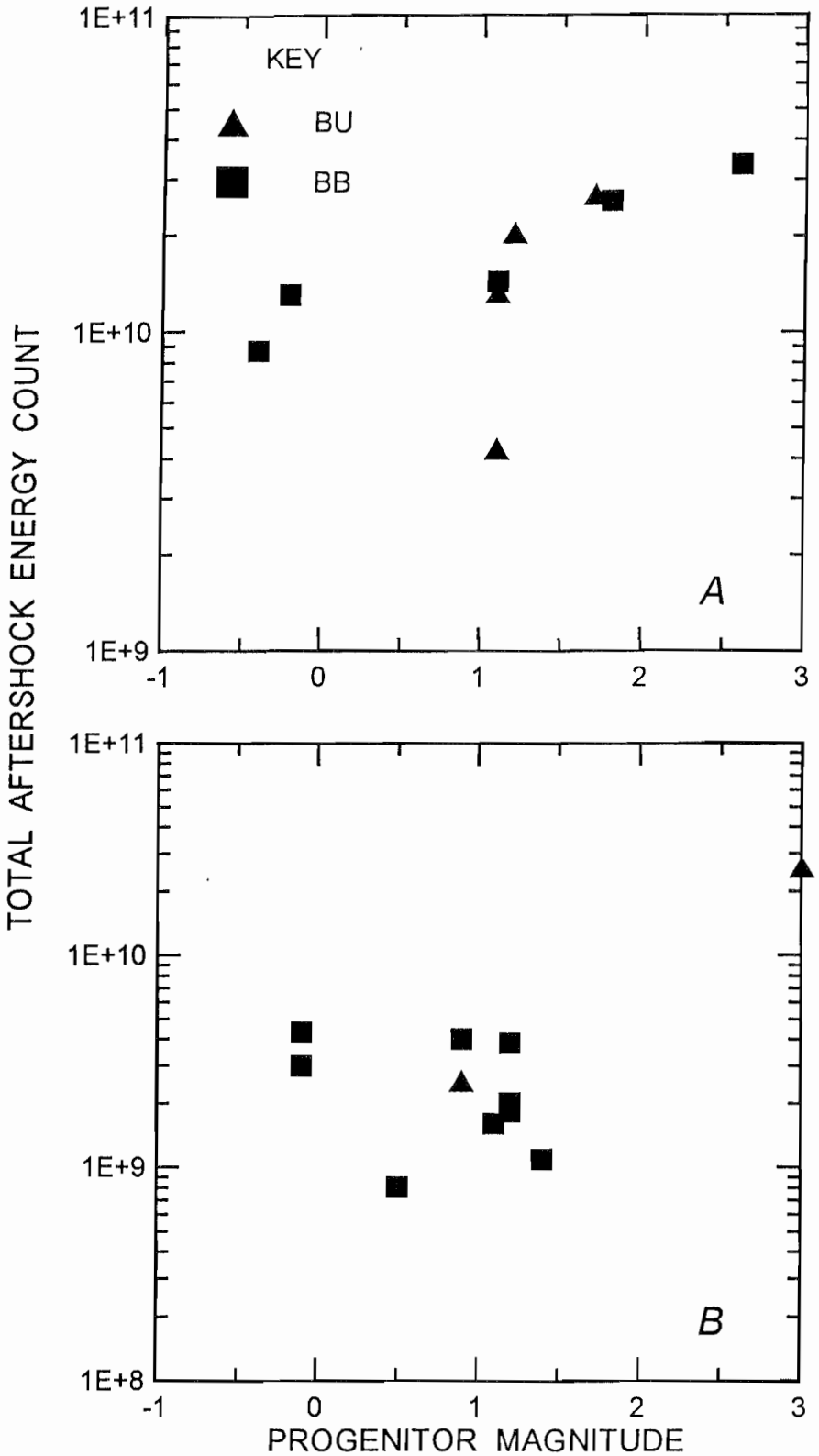

Cumulative aftershock event energy (ET) 16 h after progenitor occurrence as a function of the sequence progenitor magnitude for selected sequences near (A) stope 189 and (B) stope 99.

Figure 15

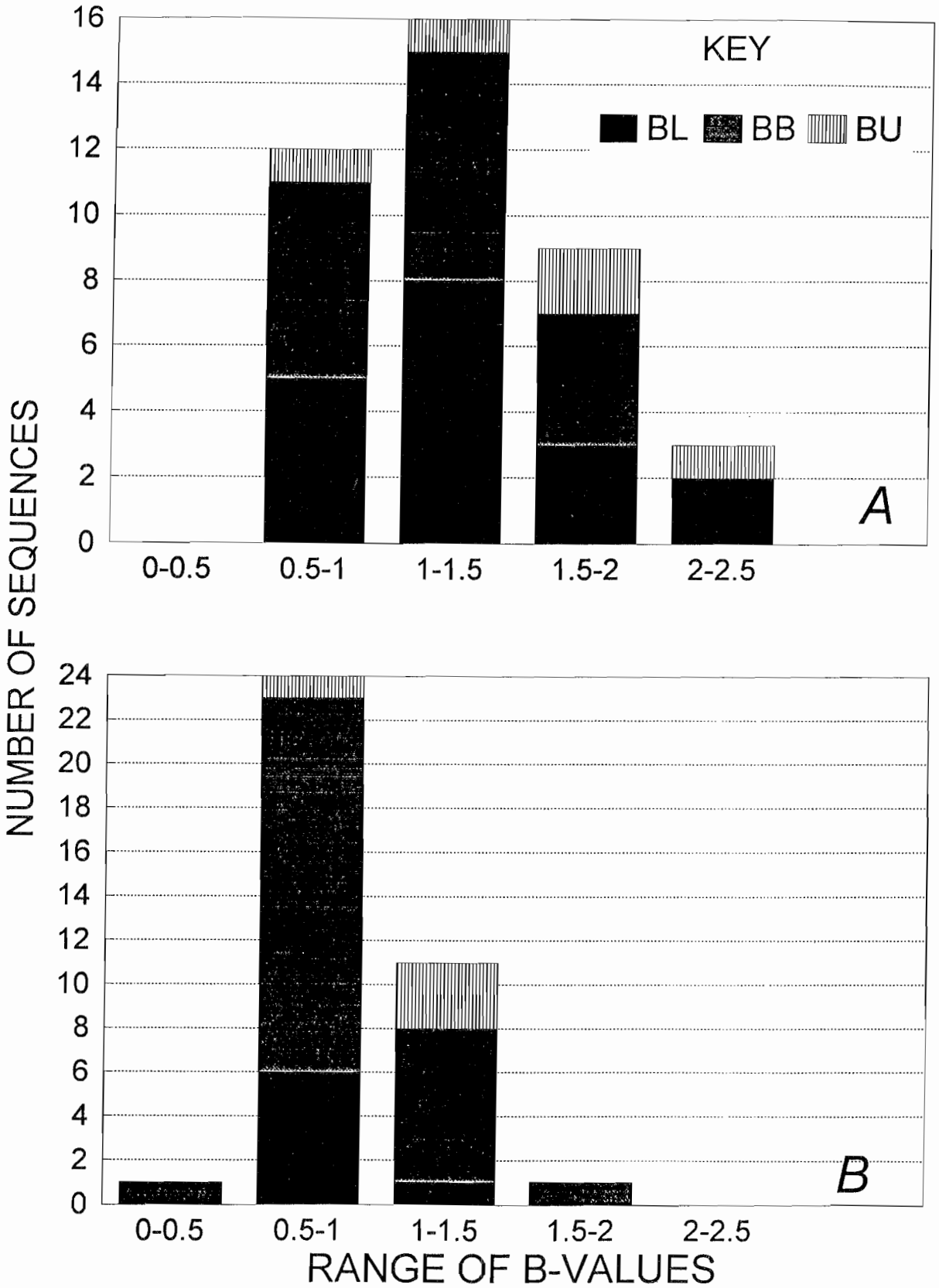

B-value (BV) distribution for (A) stope 189 and (B) stope 99.

Figure 16

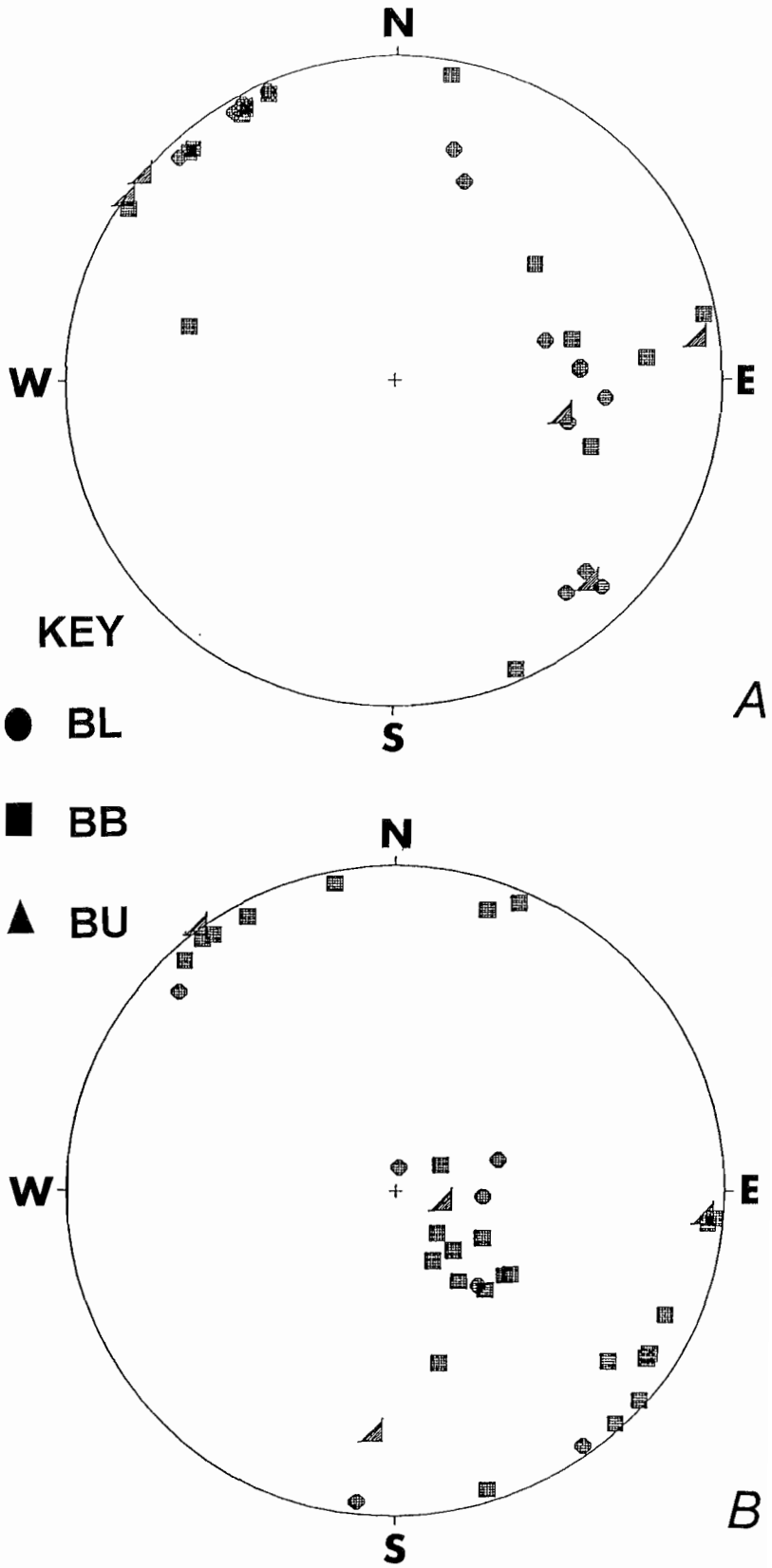

Poles to primary planes fitted to well-located events in 16-h sequences near (A) stope 189 and (B) stope 99.

Figure 17

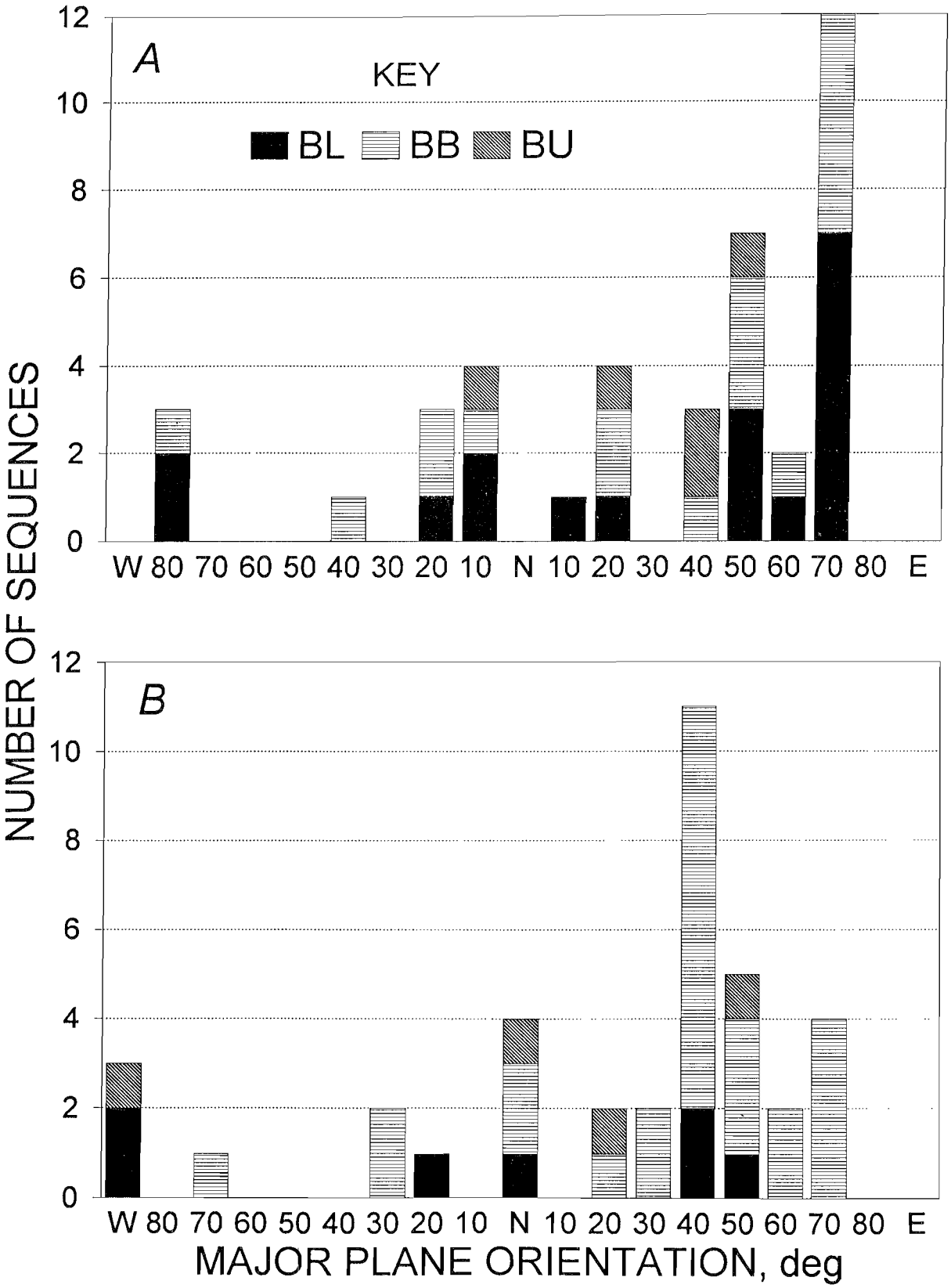

Orientation of primary planes fitted to well-located events in 16-h sequences near (A) stope 189 and (B) stope 99. Note that the mined vein generally strikes N. 70° E. and N. 45° E. in stopes 189 and 99, respectively.

Figure 18

A

	Stope 189
Stope 99	**BV, DR, CV, SR, D, EA, ET,** *S*

B

		BL
	BB	**EA** *N*
BU	**CV**	*CV N*

C

		BL
	BB	**AD, EA**
BU	*CV*	*BV*

Results of Kolmogorov-Smirnov two-sided tests, comparing (A) both stopes, (B) sequence types in stope 189, and (C) sequence types in stope 99. Only those attributes that allow rejection of the null hypothesis at the 95% confidence level (boldface) or 90% confidence level (italics) are listed. That is, differences between the column and row heading subsets are highly significant for only those attributes listed. See table 2 for attribute label identifications.

Figure 19

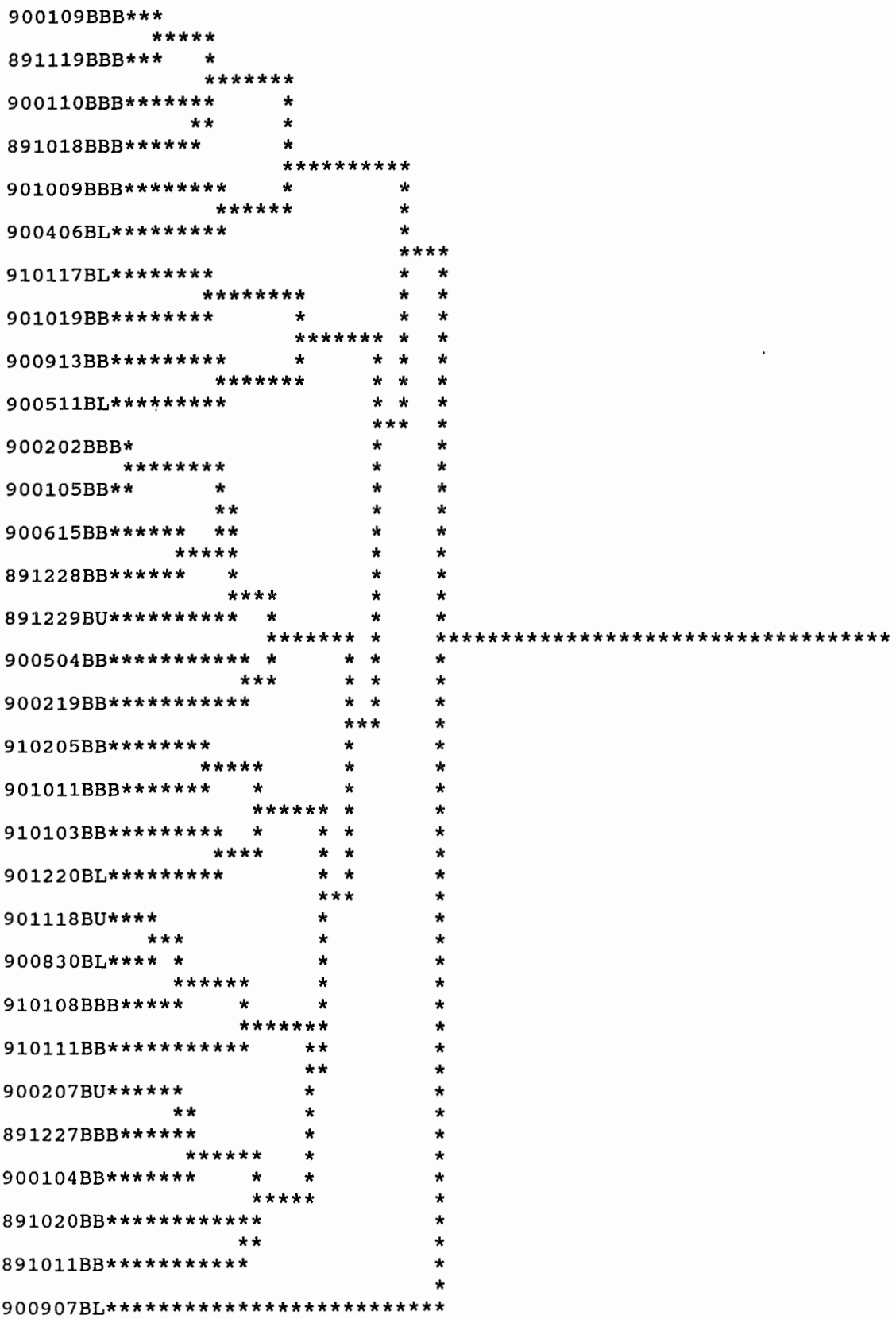

Dendogram depicting group associations among 31 selected aftershock sequences from stope 99. Progenitor type follows sequence date.

Figure 20

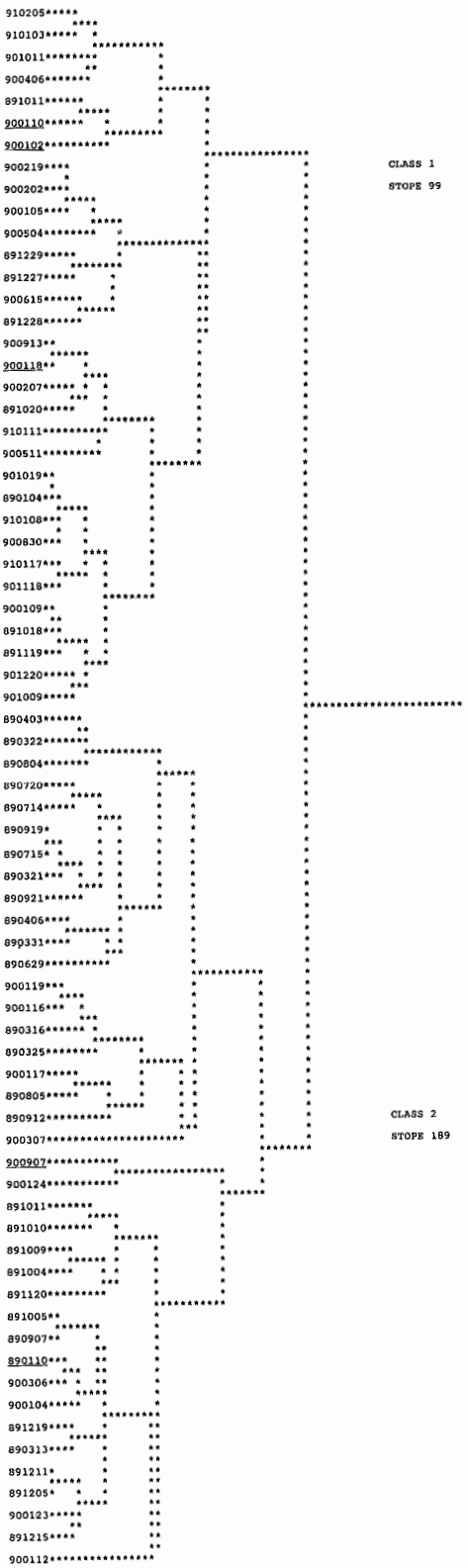

Dendogram depicting group associations among all 71 selected aftershock sequences from stopes 189 and 99. Sequence identification numbers underlined were misclassified as belonging to the other stope.

Figure 21

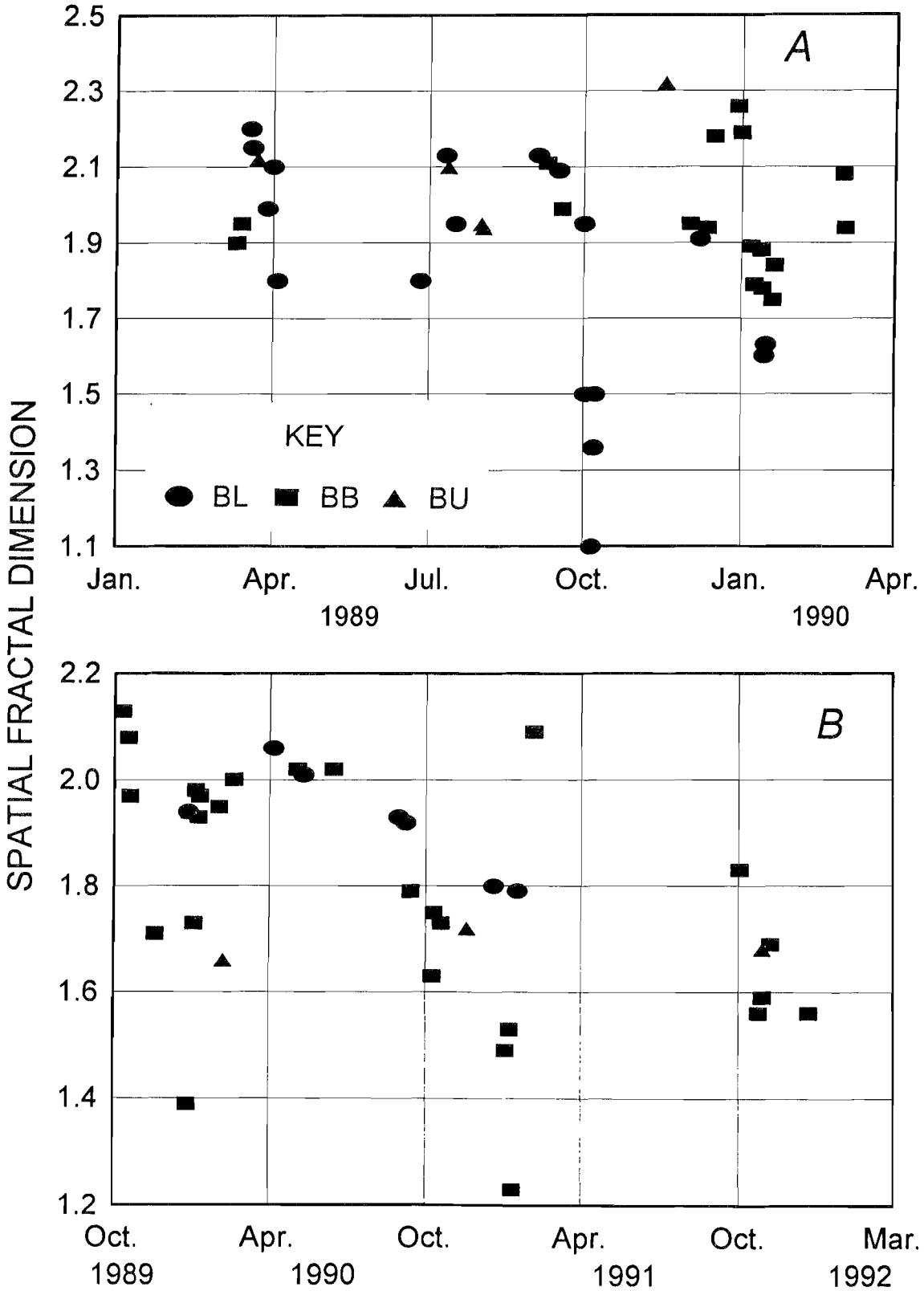

Aftershock sequence spatial fractal dimension (SF) as a function of sequence progenitor occurrence time near (A) stope 189 and (B) stope 99.

Figure 22

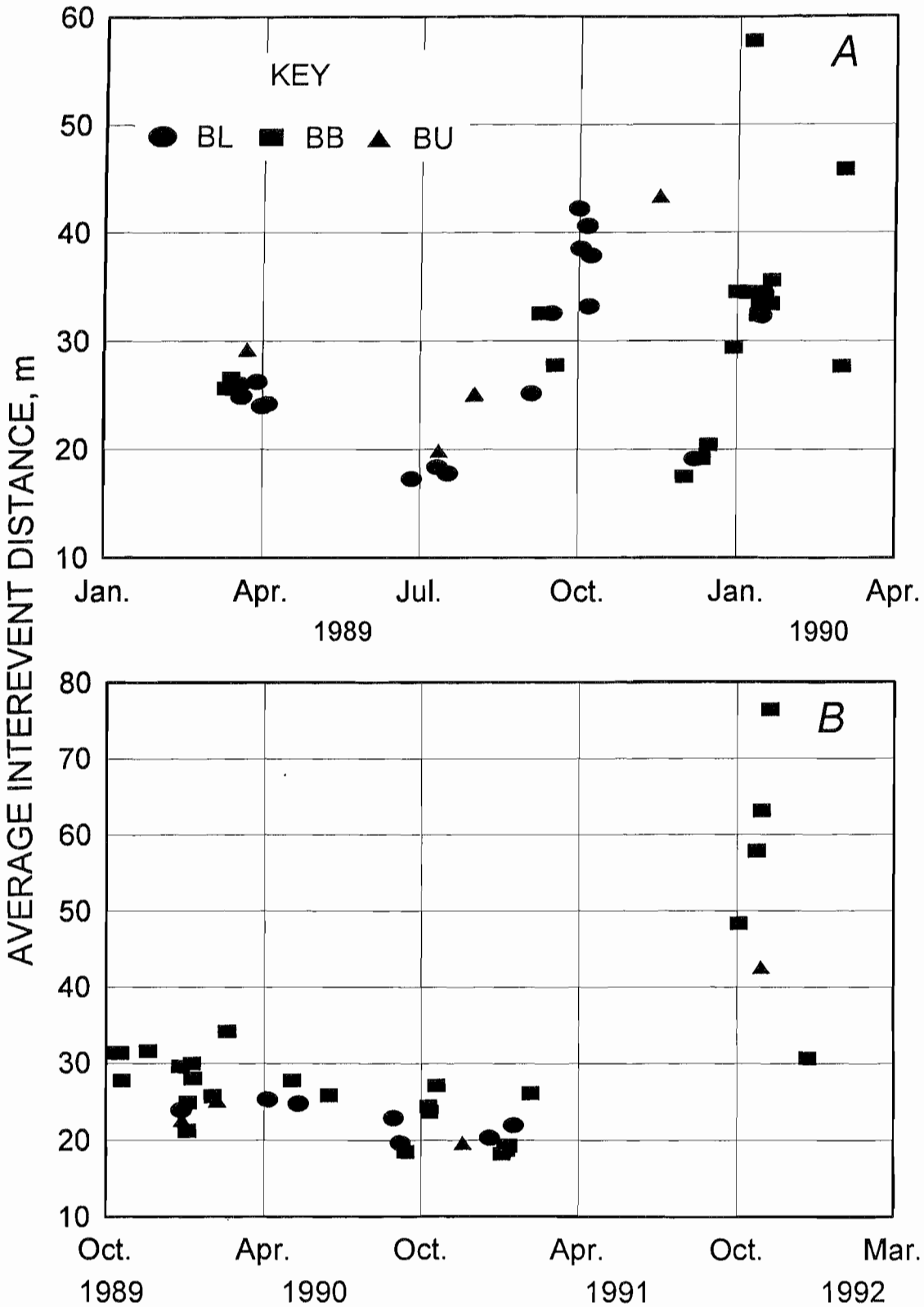

Aftershock sequence interevent distance average (AD) as a function of sequence progenitor occurrence time near (A) stope 189 and (B) stope 99.

Figure 23

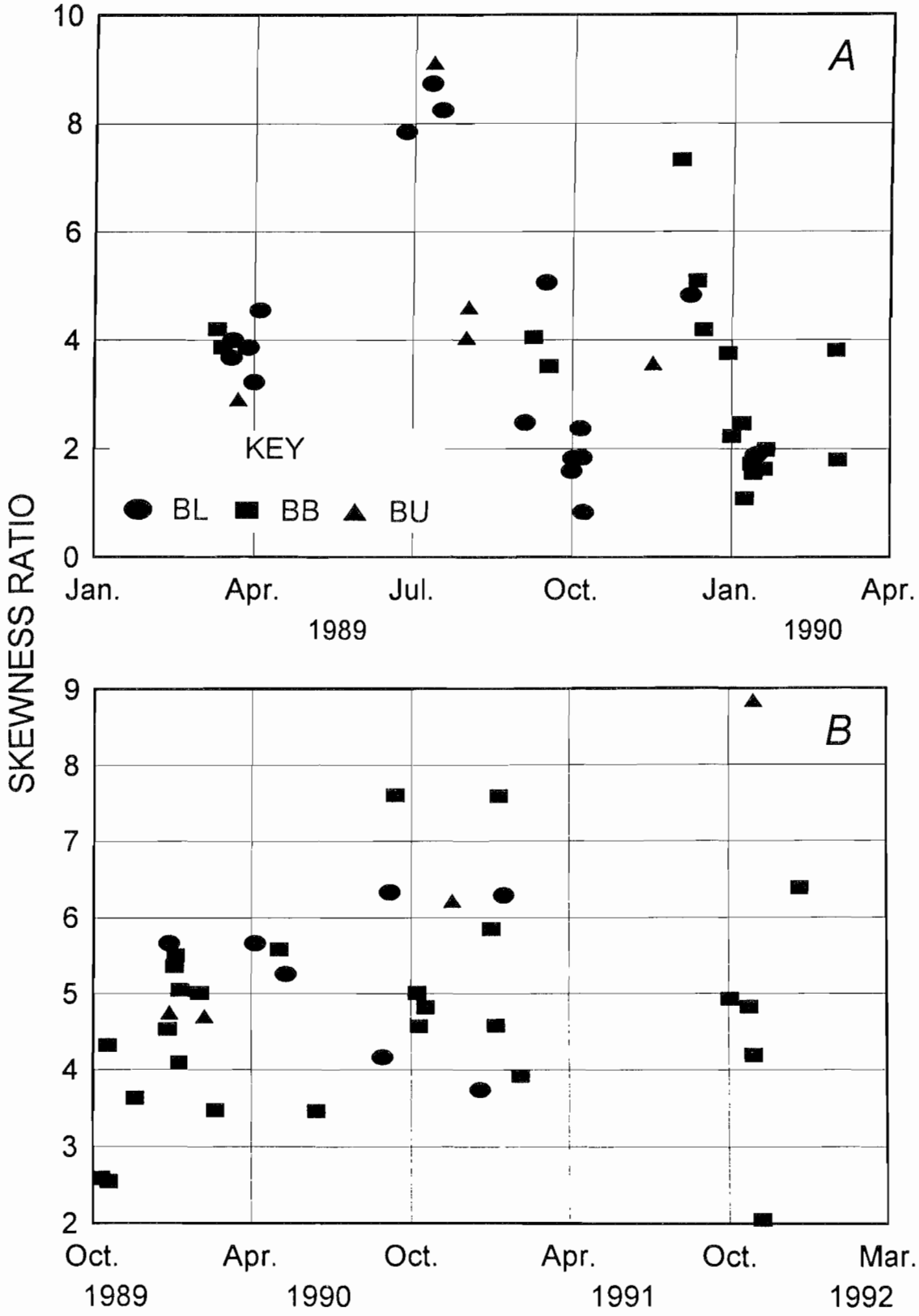

Aftershock sequence spatial skewness ratio (SR) as a function of sequence progenitor occurrence time near (A) stope 189 and (B) stope 99.

Figure 24

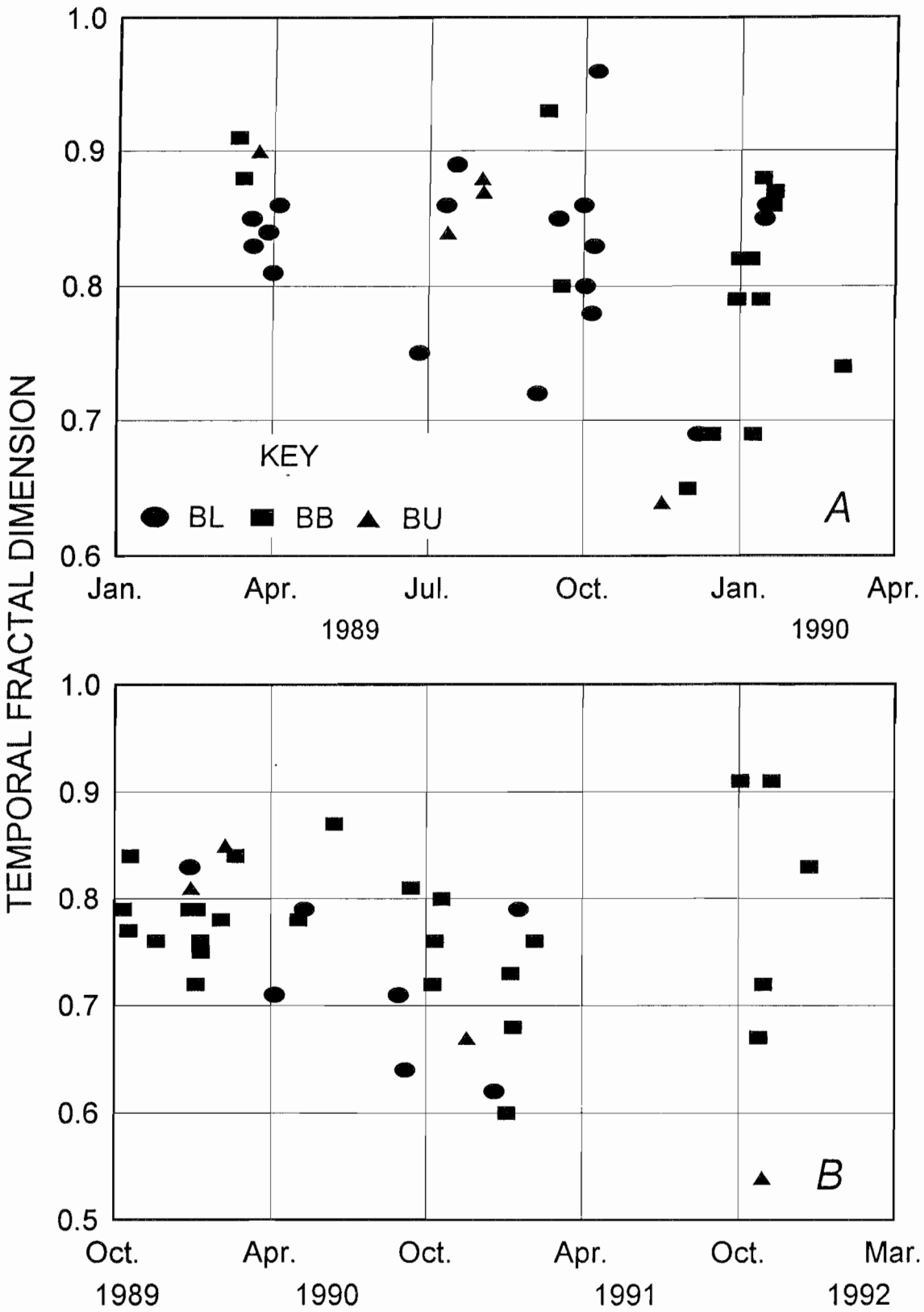

Aftershock sequence temporal fractal dimension (TF) as a function of sequence progenitor occurrence time near (A) stope 189 and (B) stope 99.

Figure 25

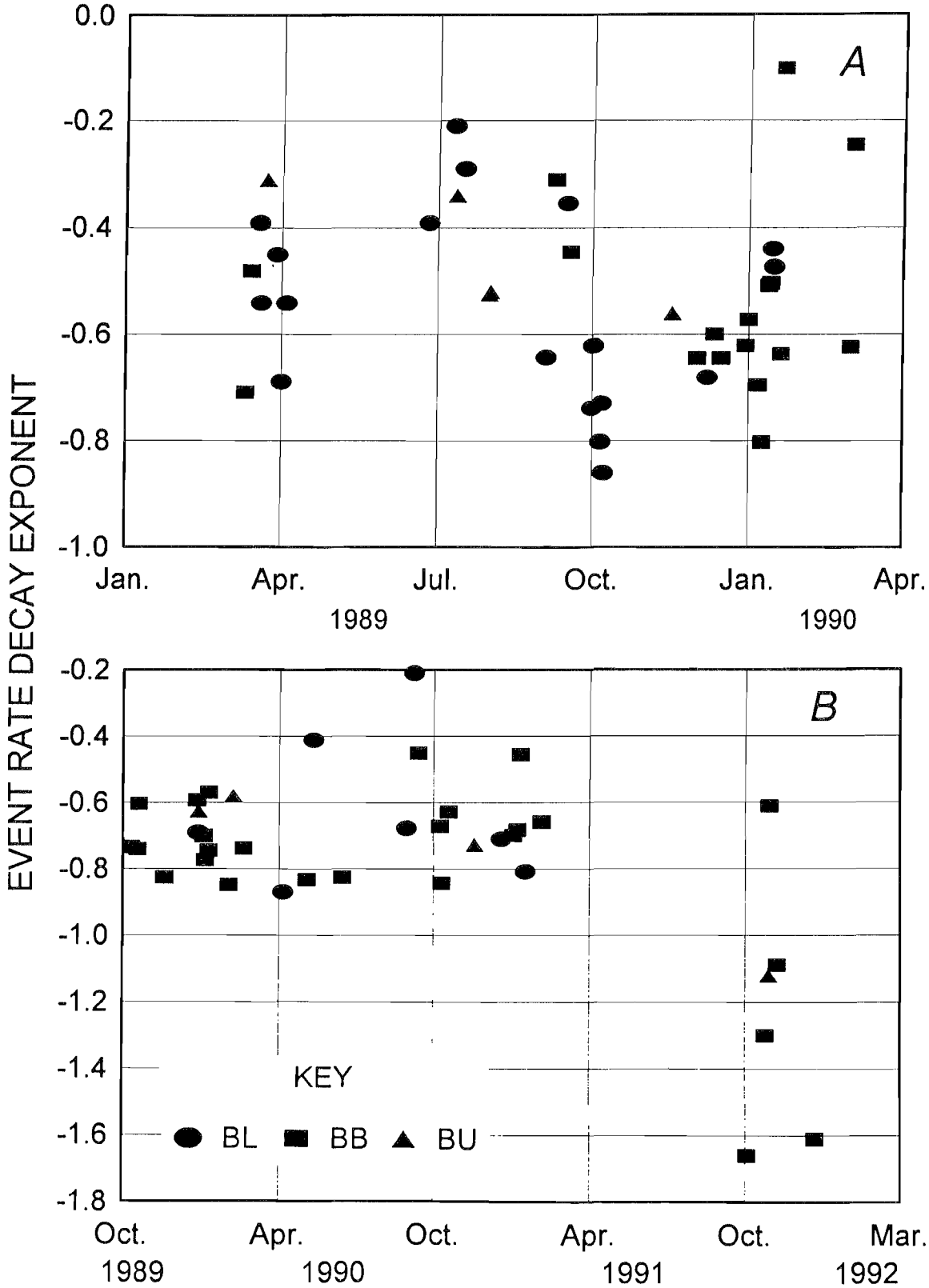

Aftershock sequence event rate decay exponent (DR) as a function of sequence progenitor occurrence time near (A) stope 189 and (B) stope 99.

Figure 26

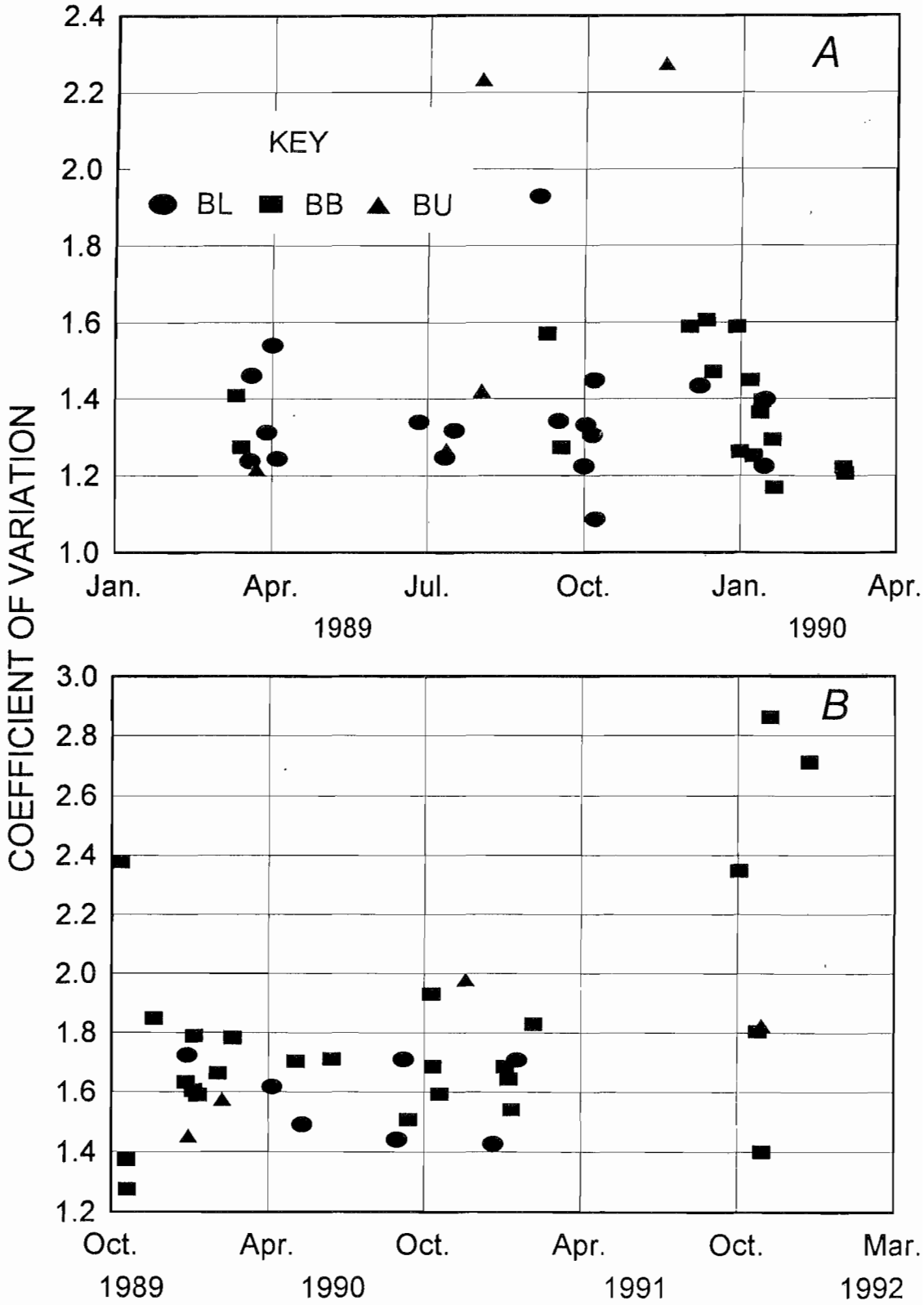

Aftershock sequence temporal coefficient of variation (CV) as a function of sequence progenitor occurrence time near (A) stope 189 and (B) stope 99.

Figure 27

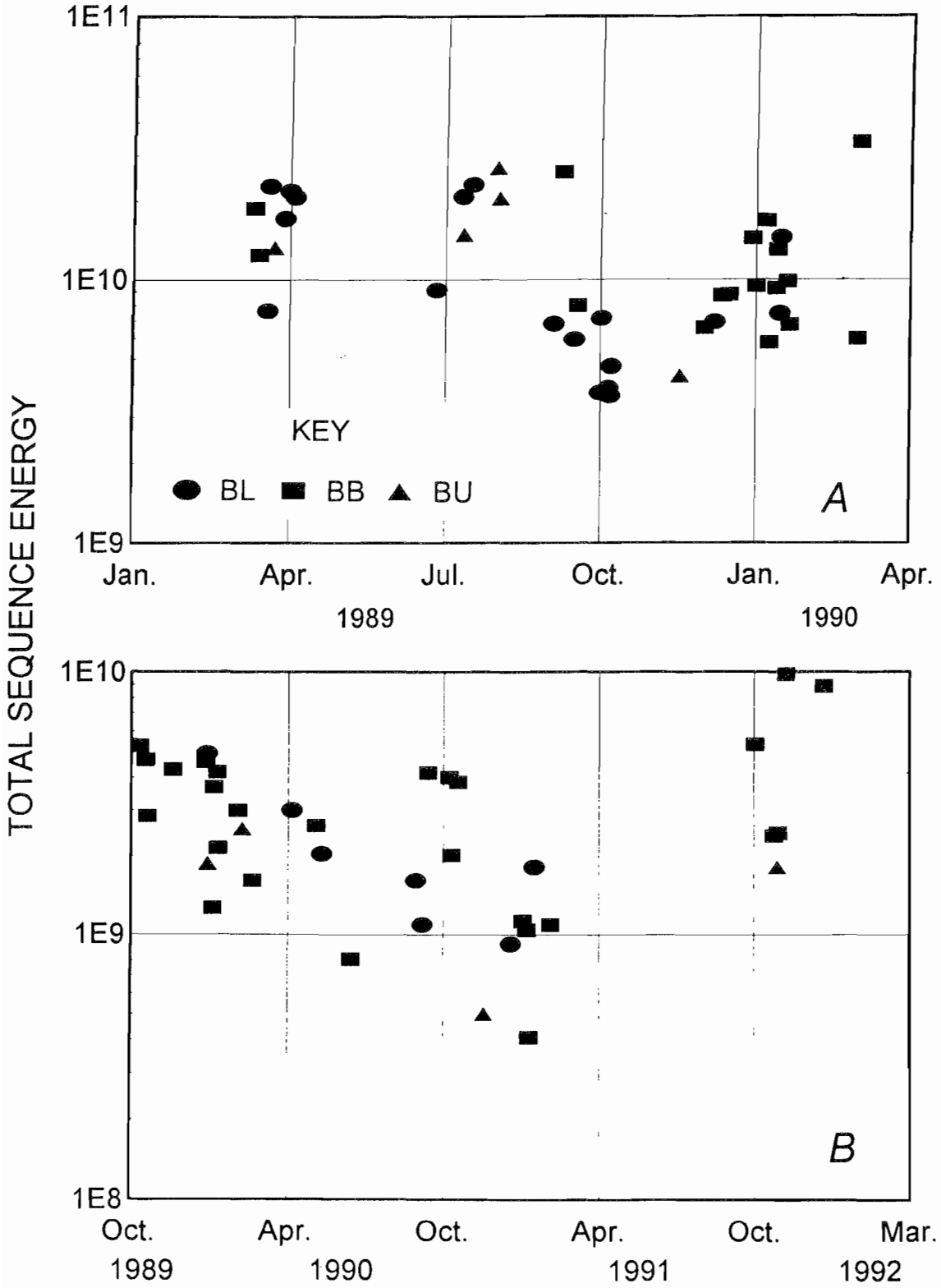

Total aftershock sequence energy (ET) as a function of sequence progenitor occurrence time near (A) stope 189 and (B) stope 99.

Figure 28

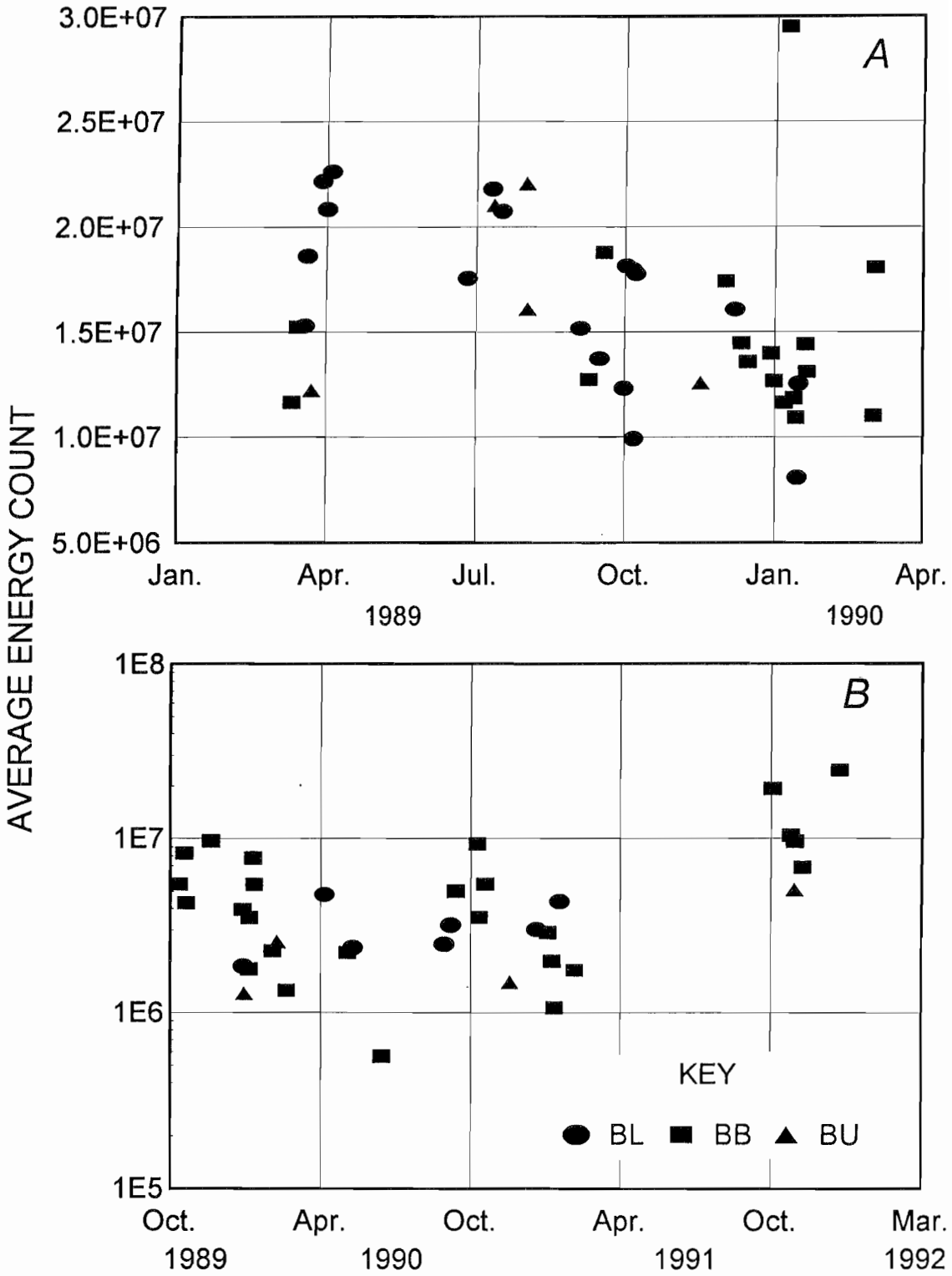

Aftershock sequence average event energy (EA) as a function of sequence progenitor occurrence time near (A) stope 189 and (B) stope 99.

Figure 29

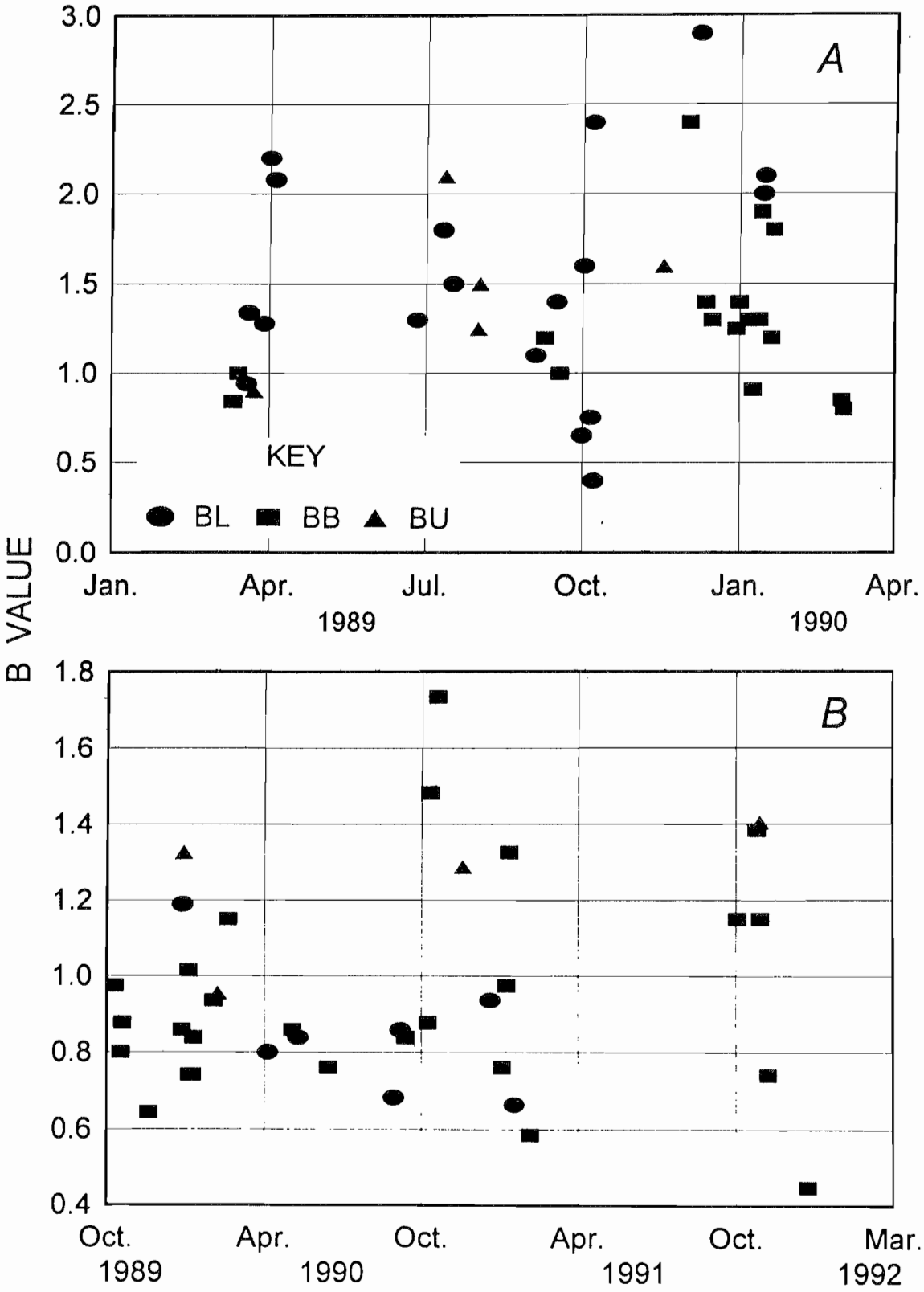

B-value (BV) as a function of aftershock sequence occurrence time for (A) stope 189 and (B) stope 99.

Figure 30

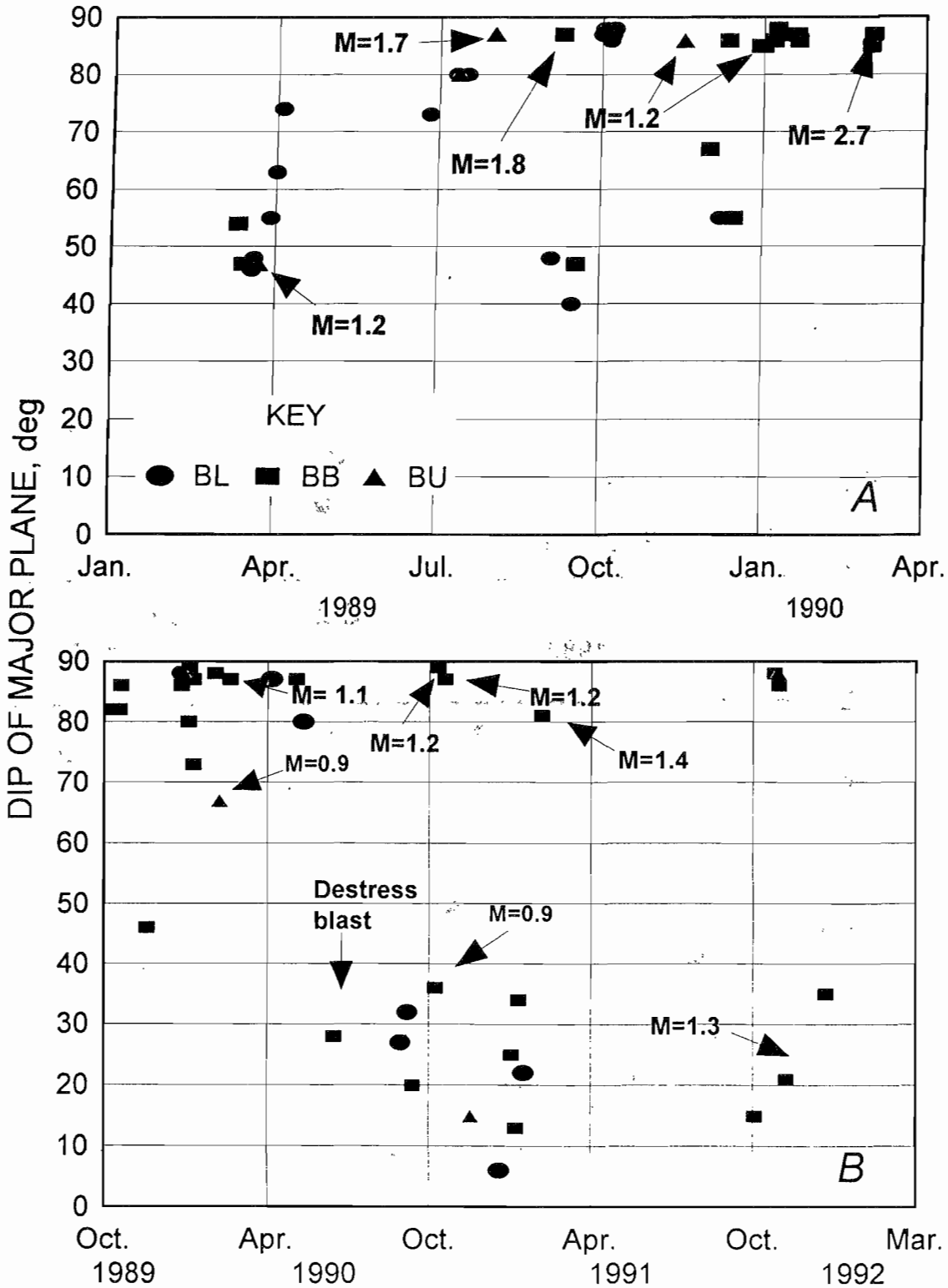

Dip of major plane fitted to sets of aftershock sequence event locations as a function of sequence progenitor occurrence time near (A) stope 189 and (B) stope 99. Magnitudes (M) of larger sequence progenitors are given.

Figure 31

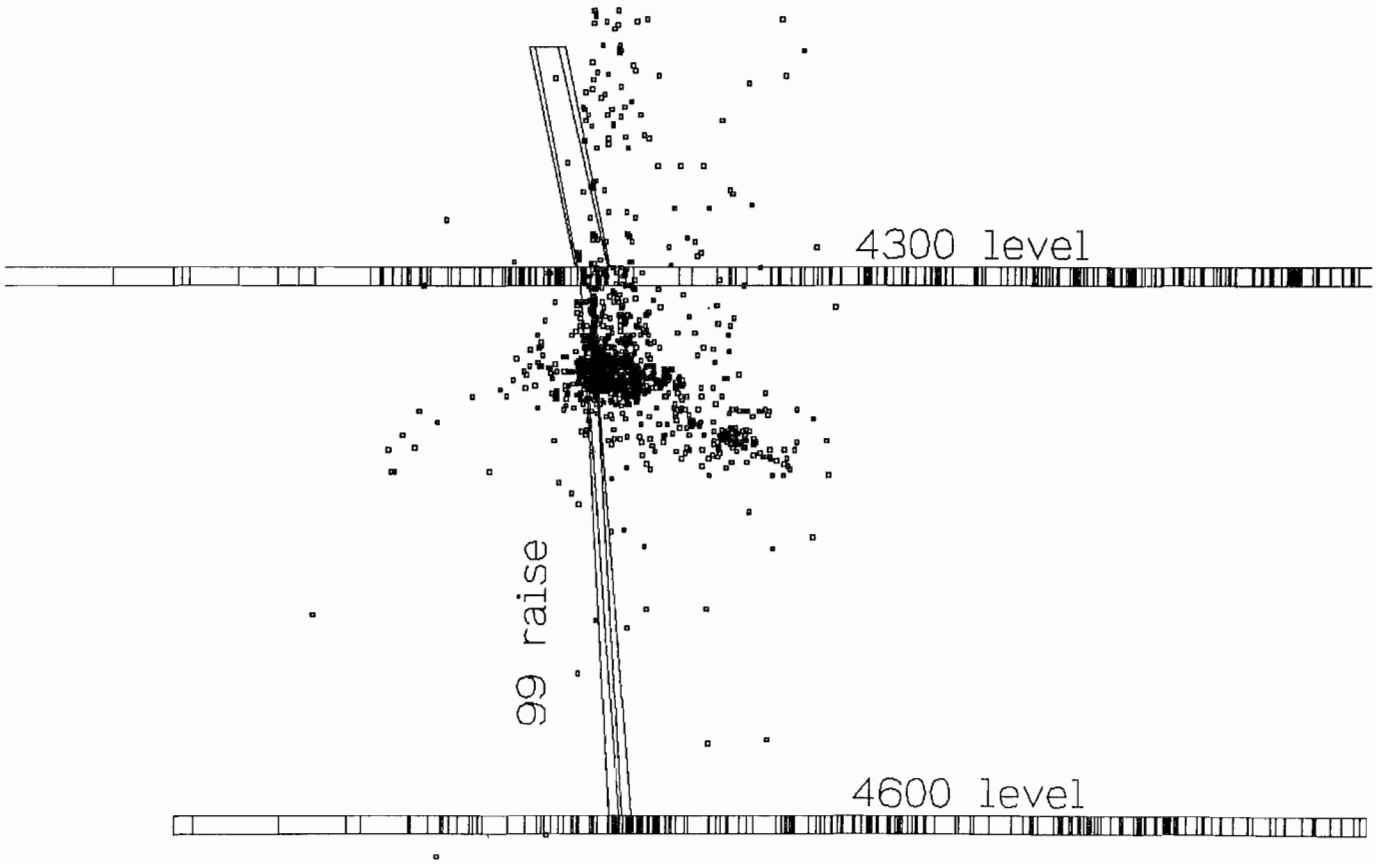

Event locations following destress blast 900615 in stope 99. 4300 level workings and raises near stope 99 are shown. View looking northwest.

Figure 32

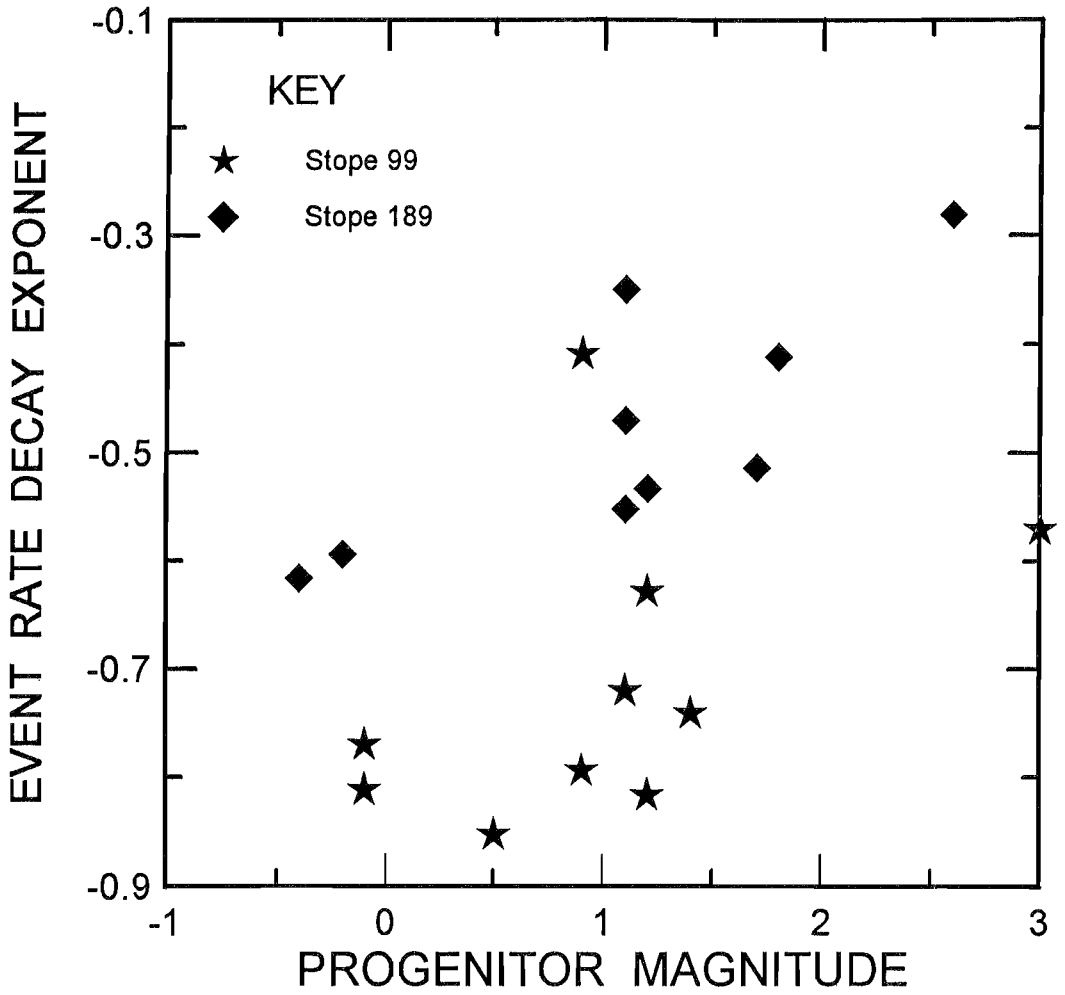

Positive, but weak, correlation between event rate decay exponent (DR) and magnitude (M) attributes for stope 99 and stope 189.

Figure 33

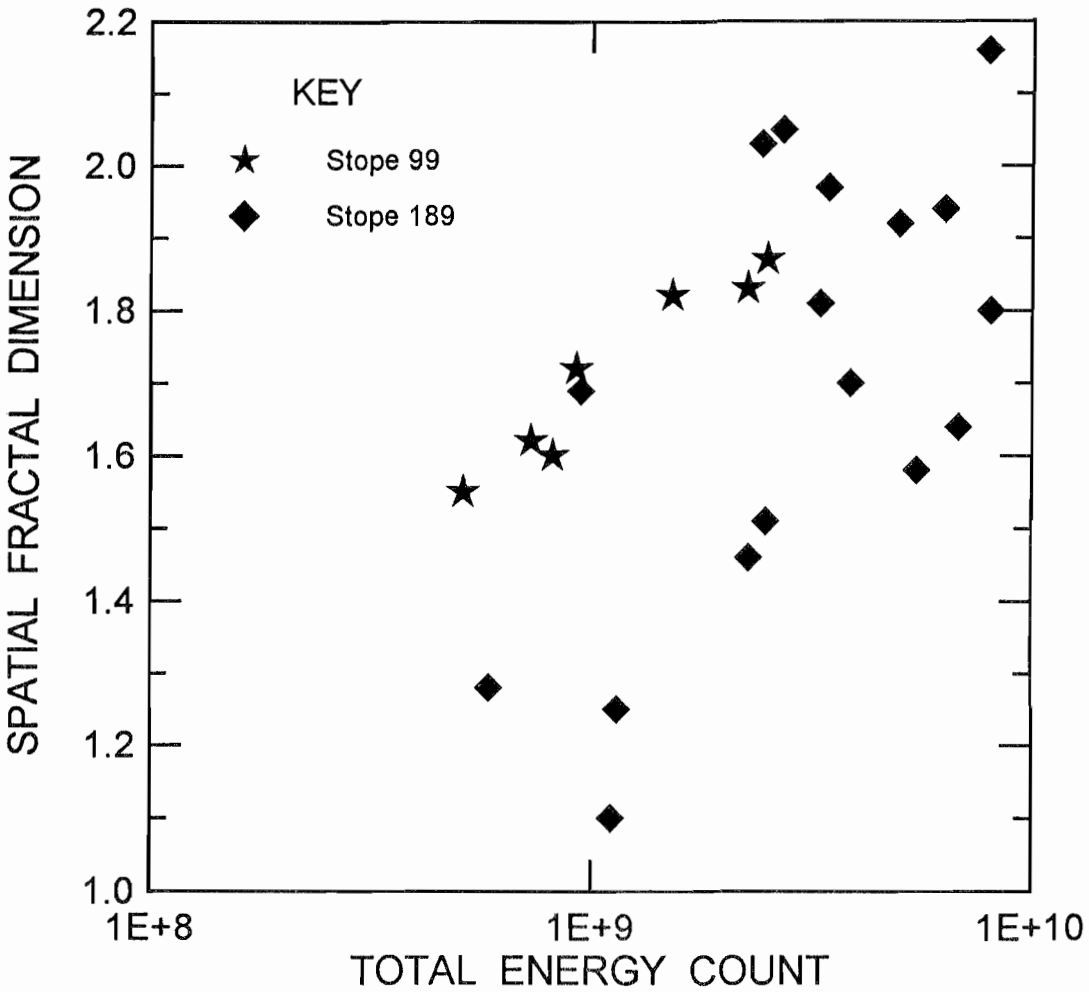

Positive correlation between spatial fractal dimension (SF) and total energy count (ET) attributes for blast (BL) sequences only.

Figure 34

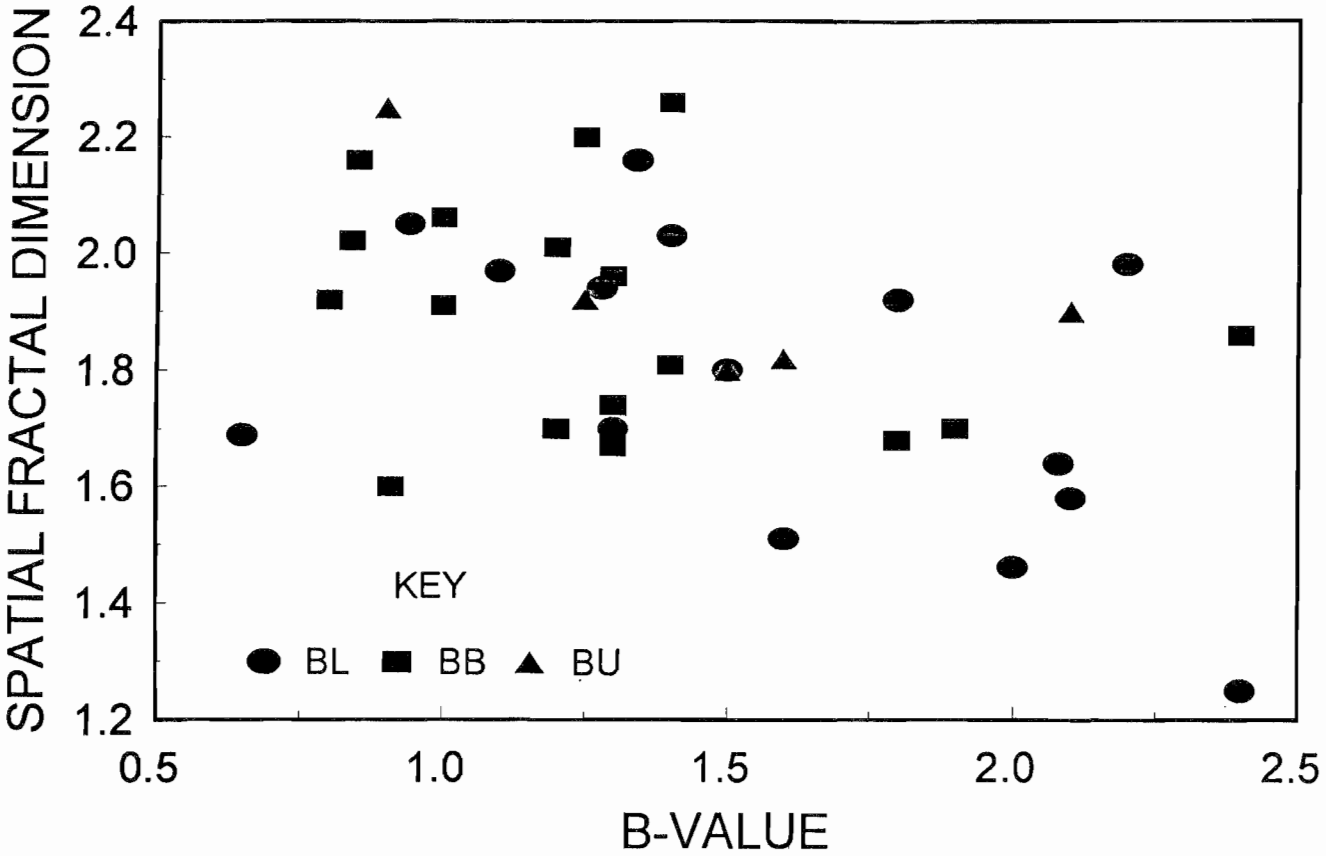

Spatial fractal dimension (SF) versus B-value (BV) for stope 189.

Figure A-1

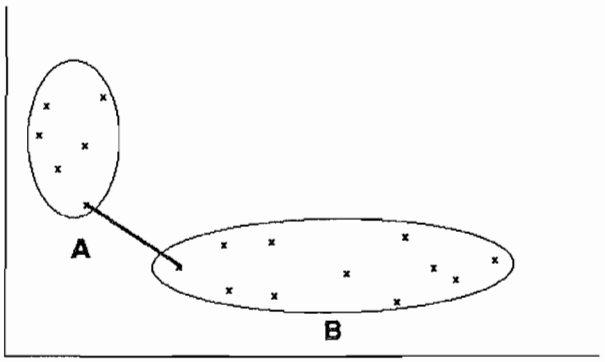

Schematic of single-link clustering method to separate class A from B.

Figure A-2

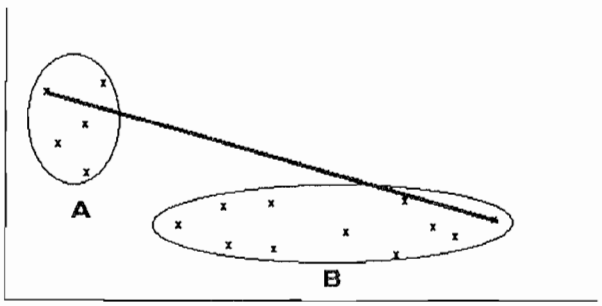

Schematic of complete-link clustering method to separate class A from B.

Figure A-3

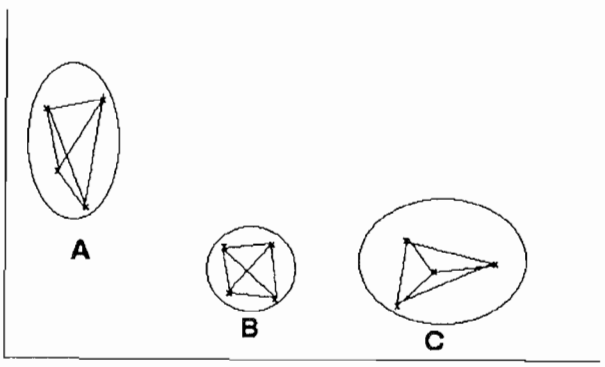

Schematic of minimizing within-group dissimilarity method to separate groups.

Figure A-4

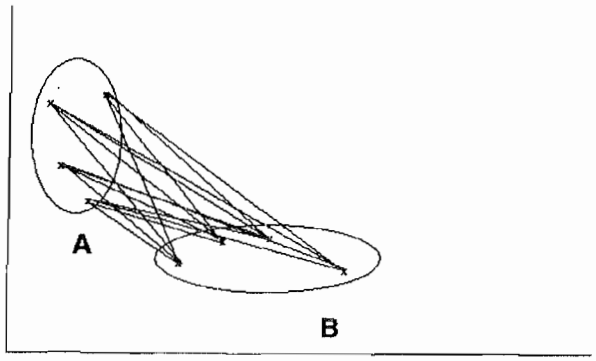

Schematic of maximizing dissimilarity between corresponding attributes method.

Figure A-5

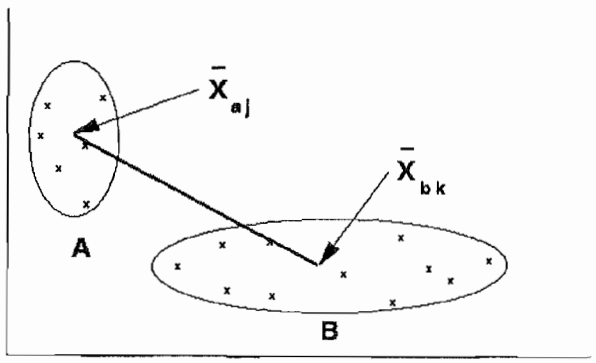

Schematic of centroid clustering method to separate class A from B.

Figure B-1

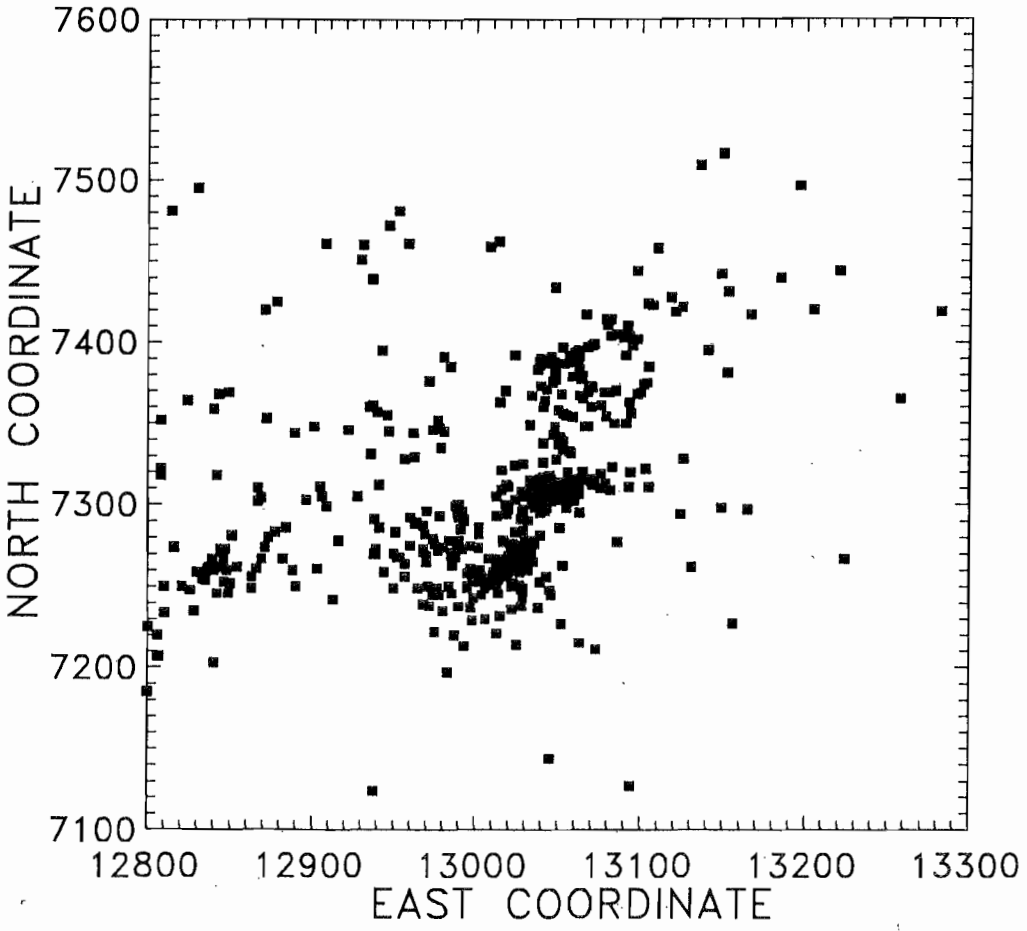

Epicenters of 563 events occurring over a 3-day period.

Figure B-2

```
ICLUS:
  2   2   2   2   2   2   2   2   2   2
  2   2   2   2   2   2   2   2   2   2
  2   2   2   2   2   2   2   2   2   2
  2   2   2   2   2   2   2   2   2   2
  2   1   1   1   1   1   1   1   1   1
  1   1   1   1   1   1   1   1   1   1
  1   1   2   1   1   1   1   1   1   1
  1   1   1   1   1   1   1   1   1   1
  1   1   1   1   1   1   1   1   1   1
  1   1   1   1   1   2   2   2   2   2
  2   2   2   2   2   2   2   2   2   2
  2   2   2   2   2   2   2   2   2   2
  2   2   2   2   2   2   2   2   2   2
  2   2   2   2   2   2   2   2   2   2
  2   2   2   2   2   1   2   2   1   2
  2   1   1   1   1   1   1   1   2   2
  1   1   2   2   2   2   2   2   2   2
  2   2   2   2   2   2   2   2   2   2
  2   2   2   2   2   2   2   2   2   2
  2   2   2   2   2   2   2   2   2   2
  2   2   2   2   2   2   2   2   2   2
  2   2   2   2   2   2   2   2   2   2
  2   2   2   2   2   2   2   2   2   2
  2   2   2   2   2   1   2   2   2   2
  2   2   2   2   2   2   2   2   2   2
  2   2   2   2   2   2   2   2   2   2
  2   2   2   2   2   2   2   2   2   2
  2   2   2   2   2   2   2   2   2   2
  2   2   2   2   2   2   2   2   2   2
  2   2   2   2   2   2   2   2   2   2
  2   2   2   2   2   2   2   2   2   2
  2   2   2   2   2   2   2   2   2   2
  2   2   2   2   2   2   2   2   2   2
  2   2   2   2   2   2   2   2   2   2
  2   2   2   2   2   2   2   2   2   2
  2   2   2   1   2   2   2   2   2   2
  2   2   2   2   2   2   2   2   2   2
  2   2   2   2   2   2   2   2   2   1
  2   1   2   2   2   2   2   2   2   2
  2   2   2   2   2   2   2   2   2   2
  2   2   2   2   2   2   2   2   2   2
  2   2   1   2   2   2   2   2   2   2
  2   2   2   2   2   2   2   2   2   2
  2   2   2   2   2   2   2   2   2   1
  2   2   1   2   2   2   2   2   2   2
  2   2   2   2   2   2   2   2   2   2
  2   1   2   2   2   2   2   2   2   2
  2   2   2   2   2   2   2   2   2   2
  2   2   2   2   2   2   2   1   2   2
  2   2   2   2   2   2   2   2   2   2
  2   2   2   2   2   2   2   2   2   2
  2   2   2   2   2   2   2   2   2   2
  2   2   2   2   2   2   2   2   2   2
  2   2   2   2   2   2   2   2   2   2
  2   2   2   2   2   2   2   2   2   1
  2   2   2   2   1   2   2   2   2   2
  2   2   2
 NCLUS:  75  488
```

Class assignments of individual microseismic events as a function of order of occurrence (left to right, top to bottom) assuming two classes. Boxed event was a blast.

Figure B-3

```
ICLUS:
  2   2   2   2   2   2   2   2   2   2
  2   2   2   2   2   2   2   2   2   2
  2   2   2   2   2   2   2   2   2   2
  2   2   2   2   2   2   2   2   2   2
  2   3   3   3   3   3   3   3   3   3
  3   3   3   3   3   3   3   3   3   3
  3   3   2   3   3   3   3   3   3   3
  3   3   3   3   3   3   3   3   3   3
  3   3   3   3   3   3   3   3   3   3
  3   3   3   3   3   1   2   2   2   2
  2   2   2   2   2   2   2   2   2   2
  2   2   2   2   2   2   2   2   2   2
  2   2   2   2   2   2   2   2   2   2
  2   2   2   2   2   2   2   2   2   2
  2   2   2   2   2   3   2   2   3   1
  2   3   3   3   3   3   3   3   2   1
  3   3   2   2   2   2   2   2   2   2
  2   2   2   2   2   2   2   2   2   2
  2   2   2   2   2   2   2   2   2   2
  2   2   1   2   2   2   2   2   2   2
  2   2   2   2   2   2   2   2   2   2
  2   2   2   2   2   2   2   2   2   1
  2   2   2   2   2   2   2   2   2   2
  2   2   2   1   2   3   2   2   2   2
  2   2   2   2   2   2   2   2   2   2
  2   1   2   2   2   2   2   2   1   2
  1   2   2   2   2   1   2   1   2   2
  2   1   2   1   2   2   2   1   2   1
  2   2   1   2   1   2   2   2   2   2
  1   1   1   2   2   2   2   2   2   1
  2   2   2   2   2   1   2   2   2   2
  1   2   2   1   2   2   2   1   2   2
  1   2   2   2   2   2   2   1   1   2
  1   2   2   1   2   2   2   2   2   2
  2   2   2   2   1   1   1   2   1   2
  1   2   2   3   1   1   2   2   2   2
  2   2   2   2   2   2   2   2   2   2
  2   1   2   2   2   2   2   2   2   3
  1   3   2   1   2   2   2   1   2   1
  2   2   2   1   2   2   2   1   2   1
  2   2   1   2   2   2   2   2   2   2
  2   1   3   2   2   2   2   2   2   1
  2   2   2   1   2   2   1   1   1   1
  2   1   1   2   2   2   2   2   1   3
  1   2   3   2   2   2   2   2   2   1
  1   1   2   1   1   1   2   1   2   1
  1   3   1   2   2   1   2   1   2   2
  2   2   2   2   2   1   2   1   2   2
  1   1   1   2   1   2   1   3   2   2
  2   2   1   1   2   1   2   2   2   2
  1   2   2   2   2   2   2   2   1   2
  1   2   2   2   2   2   2   1   2   1
  1   2   2   2   2   2   2   2   1   2
  2   2   2   2   2   2   1   1   1   2
  2   1   2   1   1   1   2   1   1   3
  2   2   2   2   3   1   2   1   2   2
  2   2   1
 NCLUS:  98  390  75
```

Class assignments of individual microseismic events as a function of order of occurrence, assuming three classes. Boxed event was a blast.

Figure B-4

ICLUS:

4	1	1	1	1	1	4	1	1	1
1	1	1	1	1	1	1	1	1	1
1	1	1	1	1	1	1	1	1	4
1	1	1	1	1	4	1	1	1	1
1	2	2	2	2	2	1	2	1	2
2	2	2	2	2	2	2	2	2	2
1	2	1	2	2	2	2	1	2	2
2	2	2	2	2	2	2	2	2	2
2	2	2	2	2	2	2	1	2	2
2	2	2	2	2	2	1	1	1	1
1	4	1	1	1	1	1	1	1	1
1	1	1	1	1	1	1	1	1	1
1	1	1	1	1	1	1	1	1	1
1	1	1	1	1	1	1	1	1	1
1	1	1	1	1	2	1	1	2	1
1	2	2	2	2	1	2	2	1	2
1	2	1	1	1	1	1	1	1	1
1	1	1	1	1	2	1	1	2	1
1	1	1	1	1	1	1	4	1	1
1	1	1	1	1	1	1	1	1	1
1	1	1	1	1	1	1	1	1	1
1	1	1	1	1	1	1	1	1	1
1	1	1	1	1	2	[4]	1	4	4
4	1	4	1	4	1	4	4	4	4
1	1	1	1	1	1	1	1	1	1
1	1	1	1	1	1	1	1	1	1
1	1	1	1	1	1	1	1	1	4
1	1	1	1	1	1	4	1	1	1
1	1	1	1	1	1	1	1	1	1
1	1	1	1	1	1	1	1	1	1
1	1	1	1	1	1	1	1	1	1
1	1	1	1	1	1	1	2	1	1
1	1	1	1	4	1	1	1	1	1
1	1	1	1	4	1	1	1	1	1
1	1	1	1	1	1	1	1	1	1
1	1	1	1	1	1	2	1	1	1
1	1	1	1	1	1	1	1	1	1
1	2	1	1	1	1	1	1	1	1
1	1	1	1	1	1	1	1	1	1
1	1	4	1	1	1	1	1	1	1
1	1	2	1	1	1	1	1	1	1
1	1	1	1	1	1	2	1	1	1
1	1	2	1	1	1	1	1	1	2
2	1	2	1	1	1	4	1	1	1
1	1	1	1	1	1	1	1	1	2
1	2	2	3	1	1	1	1	1	1
1	1	1	1	1	1	1	2	1	1
1	1	1	1	1	1	1	1	1	1
1	1	1	1	1	1	1	1	1	1
2	1	1	1	1	1	1	1	1	1
1	1	1	1	1	1	1	1	1	1
1	1	1	1	1	1	1	1	2	1
1	1	1	1	1	1	1	1	1	1
1	2	1	1	1	1	1	1	1	2
1	1	1	1	1	2	1	2	1	1
1	1	2							

NCLUS: 458 82 1 22

Class assignment of individual microseismic events as a function of order of occurrence, assuming four classes. Boxed event was a blast.

INT.BU.OF MINES,PGH.,PA 30174

☆ USGPO 709-009/20,059